

SPECTROSCOPIC, STRUCTURAL, AND ELECTRICAL CHARACTERIZATION  
OF THIN FILMS VAPOR-DEPOSITED FROM THE  
SPIN-CROSSOVER COMPLEX  $\text{Fe}(\text{phen})_2(\text{NCS})_2$

by

EDWARD CHRISLER ELLINGSWORTH

GREG J. SZULCZEWSKI, COMMITTEE CHAIR

SHANE C. STREET

SHANLIN L. PAN

ARUNAVA GUPTA

GARY J. MANKEY

A DISSERTATION

Submitted in partial fulfillment of the requirements  
for the degree of Doctor of Philosophy  
in the Department of Chemistry  
in the Graduate School of  
The University of Alabama

TUSCALOOSA, ALABAMA

2015

UMI Number: 3711545

All rights reserved

INFORMATION TO ALL USERS

The quality of this reproduction is dependent upon the quality of the copy submitted.

In the unlikely event that the author did not send a complete manuscript and there are missing pages, these will be noted. Also, if material had to be removed, a note will indicate the deletion.



UMI 3711545

Published by ProQuest LLC (2015). Copyright in the Dissertation held by the Author.

Microform Edition © ProQuest LLC.

All rights reserved. This work is protected against unauthorized copying under Title 17, United States Code



ProQuest LLC.  
789 East Eisenhower Parkway  
P.O. Box 1346  
Ann Arbor, MI 48106 - 1346

Copyright Edward Chrisler Ellingsworth 2015  
ALL RIGHTS RESERVED

## ABSTRACT

Thin films (~100 nm) have been prepared of the prototypical spin-crossover complex  $\text{Fe}(\text{phen})_2(\text{NCS})_2$  (phen = 1,10-phenanthroline). Initial attempts to prepare these films by direct vapor deposition yielded films of a different material. Through extensive FT-IR, Raman, UV-Vis, and x-ray photoelectron spectroscopy it is shown that these as-deposited films are the ferriin-based *tris* complex  $[\text{Fe}(\text{phen})_3](\text{SCN})_2$ . Structural characterization by AFM and powder XRD reveals them to be smooth and amorphous. When heated, the  $[\text{Fe}(\text{phen})_3](\text{SCN})_2$  films are converted first to  $\text{Fe}(\text{phen})_2(\text{SCN})_2$  and then to a third species postulated to be  $\text{Fe}(\text{phen})(\text{NCS})_2$  which is likely a one-dimensional coordination polymer. On the other hand, deposition from  $\text{Fe}(\text{phen})_2(\text{NCS})_2$  onto heated substrates produces a mixture of these three materials. The identity of the  $\text{Fe}(\text{phen})_2(\text{NCS})_2$  films is proved by additional spectroscopic, structural, and magnetic characterization.

Magnetometry reveals them to remain spin-crossover active albeit with a more gradual and incomplete spin-transition than the bulk material. The films are found to be granular in nature and deep crevices were observed at the grain boundaries. Within the optical microscope, the coloring of the grains is seen to be dependent upon sample orientation. Powder XRD indicates texturing of crystalline domains where the crystallographic *c*-axis is parallel to the surface normal. This represents a new process for production of  $\text{Fe}(\text{phen})_2(\text{NCS})_2$  films.

With the aim of realizing the potential for spin-crossover materials to modulate electrical conduction and vice versa, electrical characterization has been performed as a function of

temperature on vertical junction devices incorporating the prepared  $\text{Fe}(\text{phen})_2(\text{NCS})_2$  films. In order to prevent penetration of the top electrode through the cracks and crevices in the organometallic layer, a multiple sequential deposition and annealing process was developed to produce films with a continuous surface topography. A small change in the weak electrical conductivity of these devices appears at the spin transition temperature, demonstrating for the first time in *ca.* 100 nm thin films of this important material a coupling of the electrical conductivity and magnetic spin state. Here, the HS state has a higher electrical conductivity. Incorporation of LiF interfacial layers between the  $\text{Fe}(\text{phen})_2(\text{NCS})_2$  and the metal electrodes improves conduction slightly but tunneling still appears to be the current-limiting mechanism. Electrical measurements were also performed on devices made with the related complex  $[\text{Fe}(\text{phen})_3](\text{SCN})_2$ . Such films were much more conductive - as good as other typical organic semiconductor materials. All together, this work establishes the potential for this family of complexes to be incorporated into thin-film based electrical devices whose operation is based on the spin-crossover effect or otherwise.

## DEDICATION

This dissertation is dedicated to curiosity, exploration, resourcefulness, obsessive pursuits, sleepless nights, bloodshot eyes, failed approaches, and the small, hard-earned successes that make science worthwhile.

## LIST OF ABBREVIATIONS AND SYMBOLS

2-me-phen	2-methyl-phenanthroline
$\gamma_{HS}$	the fraction of molecules in the high spin state
$\gamma_{LS}$	the fraction of molecules in the low spin state
$\epsilon$	the dielectric constant of a material
$\epsilon_0$	the vacuum permittivity
$\lambda_{MAX}$	the wavelength at which maximum absorption occurs
$\mu$	charge carrier mobility
$\mu_B$	the Bohr magneton
$\mu_e$	electron mobility
$\mu_{eff}$	the effective magnetic moment
$\mu_h$	hole mobility
$\mu_s$	spin-only magnetic moment
$v$	carrier drift velocity
$\sigma$	electrical conductivity
$\chi$	magnetic susceptibility
$\chi_M$	molar magnetic susceptibility
$\chi T$	magnetic susceptibility product
$\chi_M T$	molar magnetic susceptibility product

$\Delta_o$	octahedral ligand field splitting energy
$\Delta_{o,HS}$	$\Delta_o$ in the high spin state
$\Delta_{o,LS}$	$\Delta_o$ in the low spin state
$\Delta E_{HS-LS}$	the difference in the potential energies of the high spin and low spin states
$\Delta G_{HS-LS}$	the difference in free energy between the high spin and low spin states
$\Delta G_{HS}$	the free energy of the high spin state
$\Delta G_{LS}$	the free energy of the low spin state
$\Delta H_{HS-LS}$	the difference in the enthalpies between the high spin and low spin states
$\Delta H_{HS}$	the enthalpy of the high spin state
$\Delta H_{LS}$	the enthalpy of the low spin state
$\Delta S_{HS-LS}$	the difference in the entropies between the high spin and low spin states
$\Delta S_{HS}$	the entropy of the high spin state
$\Delta S_{LS}$	the entropy of the low spin state
$\Pi$	spin pairing energy
A	film area
AFM	atomic force microscopy
Alq <sub>3</sub>	tris(8-hydroxyquinolato)aluminium
BE	binding energy
bipy	2,2'-bipyridine
btP	3-(2-pyridyl)[1,2,3]triazolo[1,5- <i>a</i> ]-pyridine
CCD	charge-coupled device
d	film thickness

dmit	4,5-dithiolato-1,3-dithiole-2-thione
E	potential energy
EPR	electron paramagnetic resonance
EXAFS	extended x-ray absorption fine structure
F	electric field
FeP1	Fe(phen)(NCS) <sub>2</sub>
FeP2	Fe(phen) <sub>2</sub> (NCS) <sub>2</sub>
FeP3	[Fe(phen) <sub>3</sub> ](SCN) <sub>2</sub>
FT-IR	Fourier transform infrared spectroscopy
FWHM	full width at half maximum
g	electron g-factor
HOPG	highly ordered pyrolytic graphite
H	applied magnetic field
HOMO	highest occupied molecular orbital
HS	high spin
Htrz	1,2,4-4H-triazole
I	current
IPES	inverse photoemission spectroscopy
ITO	indium tin oxide
J	current density
k <sub>B</sub>	Boltzmann's constant
LB	Langmuir-Blodgett

LCW	lithographically controlled wetting
LIESST	light induced excited spin state trapping
LS	low spin
LUMO	lowest occupied molecular orbital
M	magnetization
MIMIC	micro-inject molding in capillaries
MLCT	metal-to-ligand charge transfer
MSA	multiple sequential assembly
$n$	the number of intrinsic free charge carriers in a material
$n_{\text{moles}}$	the number of moles of a material
NMR	nuclear magnetic resonance
phen	1,10-phenanthroline
PID	proportional integral derivative
PMMA	poly(methyl methacrylate)
$q$	the elemental charge
QCM	quartz crystal microbalance
qsal	the deprotonated form of <i>N</i> -(8-quinolyl)salicylaldimine
$r_{\text{Fe-N}}$	Fe-N bond length
RMS	root mean squared
S	total spin of a system
SCLC	space charge limited current
SCO	spin-crossover

STM	scanning tunneling microscopy
SQUID	superconducting quantum interference device
T	temperature
$T_{1/2}$	the temperature at which half of all SCO-active molecules have switched
$T_c$	the critical temperature at which $\gamma_{HS} = \gamma_{LS}$
trz	triazole
UPS	ultraviolet photoelectron spectroscopy
UV-Vis	ultraviolet-visible spectroscopy
V	voltage
XANES	x-ray absorption near edge structure
XAS	x-ray absorption spectroscopy
XPS	x-ray photoelectron spectroscopy
XRD	x-ray diffraction

## ACKNOWLEDGMENTS

I am especially grateful to my advisor, Dr. Greg Szulczewski who first conceived of this project. I am appreciative of the infinite patience shown to me by my other committee members as well, Dr. Shanlin Pan, Dr. Shane Street, Dr. Arunava Gupta, and Dr. Gary Mankey. Others who have contributed to this work include Brittany Turner who worked on the synthesis, Dr. Leonard Spinu and Dr. Jose Vargas who provided the SQUID measurement of the FeP2 film, Dr. Dipanjan Mazumdar and Dr. Karthik Ramasamy who provided SQUID measurements here at The University of Alabama, Dr. Robert Bennet who helped with running the Raman microscope and Dr. Shane Street for allowing me to use the microscope and FT-IR, Dr. Shanlin Pan who provided use of his vacuum oven, tube furnace, and microscope, Dr. Timothy Vaid and Huaiyuan Hu who helped with the powder XRD, and Steven Kelley who helped collect TGA and powder XRD data. Thank you to The University of Alabama Department of Chemistry for providing me with the resources necessary to perform this research, to the MINT center for providing instrumentation and funding, and to the Central Analytical Facility at The University of Alabama for the same. During the course of this project I received support from the National Alumni Association's Collegiate License Tag Endowed Graduate Education Fund.

Finally, thank you to all my friends, family, and loved ones for your support.

## CONTENTS

ABSTRACT.....	ii
DEDICATION.....	iv
LIST OF ABBREVIATIONS AND SYMBOLS.....	v
ACKNOWLEDGMENTS.....	x
LIST OF TABLES.....	xiv
LIST OF FIGURES.....	xv
1. INTRODUCTION.....	1
1.1 Spin-Crossover Phenomena.....	1
1.2 Spin-Crossover at the Micro- and Nanoscales.....	9
1.3 Spin-Crossover and Electrical Conduction.....	13
1.4 Aims of this Work.....	18
2. METHODS, MATERIALS, AND SYNTHESSES.....	20
2.1 Details of the Physical Vapor Deposition System.....	20
2.2 Details of the Electrical Characterization System.....	24
2.3 Details of Other Instrumentation.....	26
2.4 [Fe(phen) <sub>3</sub> ](SCN) <sub>2</sub> .....	28
2.5 Fe(phen) <sub>2</sub> (NCS) <sub>2</sub> .....	31

2.6 Synthesis of $\text{Fe}(\text{phen})_2(\text{NCS})_2$ .....	35
2.7 Summary.....	41
3. PREPARATION AND CHARACTERIZATION OF $[\text{Fe}(\text{phen})_3](\text{SCN})_2$ FILMS.....	42
3.1 Physical Vapor Deposition of Films from $\text{Fe}(\text{phen})_2(\text{NCS})_2$ .....	42
3.2 Topography and Air Sensitivity.....	43
3.3 Ultraviolet-Visible Spectroscopy.....	49
3.4 Vibrational Spectroscopy.....	53
3.5 X-ray Photoelectron Spectroscopy.....	61
3.6 Summary.....	64
4. PREPARATION AND CHARACTERIZATION OF $\text{Fe}(\text{phen})_2(\text{NCS})_2$ FILMS.....	66
4.1 Physical Vapor Deposition from $\text{Fe}(\text{phen})_2(\text{NCS})_2$ into Glass Beakers.....	66
4.2 Effect of Post-Annealing $[\text{Fe}(\text{phen})_3](\text{SCN})_2$ Films.....	69
4.3 Further Spectroscopic Characterization of $\text{Fe}(\text{phen})_2(\text{SCN})_2$ Films.....	81
4.4 Structural Characterization of $\text{Fe}(\text{phen})_2(\text{SCN})_2$ Films.....	88
4.5 Magnetometry and Spin-Crossover of $\text{Fe}(\text{phen})_2(\text{SCN})_2$ Films.....	98
4.6 Films Deposited onto Hot Substrates.....	107
4.7 Summary.....	111
5. ELECTRICAL MEASUREMENTS OF $[\text{Fe}(\text{phen})_3](\text{SCN})_2$ AND $\text{Fe}(\text{phen})_2(\text{NCS})_2$ FILMS.	115
5.1 Device Fabrication.....	115
5.2 $[\text{Fe}(\text{phen})_3](\text{SCN})_2$ Devices.....	125
5.3 $\text{Fe}(\text{phen})_2(\text{NCS})_2$ Devices.....	130
5.4 Summary.....	146

6. CONCLUSIONS.....	148
REFERENCES.....	151

## LIST OF TABLES

3.1	Peak positions and peak assignments from the vibrational spectroscopy of FeP3 powder compared to red films deposited from FeP2.....	55
4.1	Peak positions and peak assignments from the vibrational spectroscopy of FeP2 powder compared to purple films made by annealing as-deposited films identified as FeP2.....	80
4.2	Peak positions and peak separations (eV) for the Fe(2p) and N(1s) regions of the x-ray photoelectron spectra of FeP2 and FeP3 powders and films compared with reported values.....	87

## LIST OF FIGURES

1.1	SCO configurational coordinate diagram.....	3
1.2	The change in the difference in the free energies between the HS and LS states.....	5
1.3	The continuum of SCO behaviors observed depending on the extent of cooperative effects in the lattice.....	7
2.1	Details of the physical vapor deposition system.....	21
2.2	The Al sample holder used during deposition of films.....	22
2.3	The cryostat used for making temperature-dependent electrical measurements.....	25
2.4	Molecular structures for FeP3 and the title complex FeP2.....	29
2.5	A ferriin solution and the same solution after oxidation with KMnO4 at low pH to form a ferriin solution.....	30
2.6	The result of a TGA experiment in air starting with FeP3.....	37
3.1	AFM topography scan of a ~20 nm red film deposited from FeP2.....	44
3.2	Optical micrographs (10x) of red films deposited from FeP2.....	45
3.3	Examples of morphological changes in films deposited from FeP2.....	46
3.4	X-ray diffraction (Cu K $\alpha$ ) spectrum of a red film deposited from FeP2.....	48
3.5	UV-Vis spectra of [Fe(phen) <sub>3</sub> ] <sup>2+</sup> ions in ethanol and of a red film.....	50
3.6	Absorbance vs. film thickness for films deposited on glass from FeP2 extracted from Ref. 26.....	52
3.7	FT-IR spectra of FeP3 powder compared with a red film deposited from FeP2.....	54

3.8	Raman spectrum of FeP3 powder compared to a red film deposited from FeP2 onto a Si substrate in the region from 500 to 2100 cm <sup>-1</sup> .....	58
3.9	Raman spectrum of FeP3 powder compared to a red film deposited from FeP2 onto a Si substrate in the region from 150 to 500 cm <sup>-1</sup> .....	59
3.10	X-ray photoelectron spectra (Al K <sub>α</sub> ) of FeP3 powder and of a film deposited onto ITO-glass from FeP2 powder.....	62
4.1	Example of white spots and red film deposited onto the inside of a beaker covering the deposition boat during heating of FeP2.....	67
4.2	Transmission FT-IR of films deposited from FeP2 onto Si substrates and then annealed in situ.....	70
4.3	FT-IR spectra in the region from 680 to 2300 cm <sup>-1</sup> of FeP2 powder compared to that of a purple film on a KBr substrate produced by annealing an FeP3 film.....	72
4.4	Proposed structure for FeP1 1D coordination polymer.....	74
4.5	Raman spectra of films deposited from FeP2 onto Si substrates and then annealed in situ.....	76
4.6	Raman spectrum in the region from 150 to 500 cm <sup>-1</sup> of FeP2 powder compared with that of a purple film.....	77
4.7	Raman spectrum in the region from 500 to 2100 cm <sup>-1</sup> of FeP2 powder compared with that of a purple film.....	78
4.8	UV-Vis spectrum of a purple film on glass made by annealing an FeP3 film deposited from FeP2.....	83
4.9	X-ray photoelectron spectra (Al K <sub>α</sub> ) of FeP2 powder and of a purple film.....	85
4.10	AFM topography scans of FeP2 films on different substrates.....	89
4.11	FeP2 films made by annealing FeP3 films 8 hr at 115 °C as seen through the Raman microscope.....	92
4.12	An FeP2 film on Si/Al/LiF made by annealing an FeP3 film in vacuum 8 hr at 115 °C viewed through the Raman microscope at three different magnifications.....	93

4.13	X-ray diffraction (Cu K $\alpha$ ) spectrum of an FeP2 film on glass made by annealing an FeP3 film for 8 hr at 115 °C compared to that of FeP2 powder.....	97
4.14	Diagram of crystalline domains in a textured film.....	99
4.15	The view down the b-axis of the crystal structure of FeP2.....	100
4.16	The magnetic susceptibility product ( $\chi T$ ) measured by SQUID magnetometry of an FeP2 film.....	102
4.17	Transmission FT-IR in the region of the N-CS stretching modes of films deposited from FeP2 onto Si substrates held at different temperatures.....	108
4.18	Raman spectra of films deposited from FeP2 onto Si substrates held at different temperatures.....	110
5.1	Structure of two device geometries, vertical/sandwich and horizontal/bridge, used for electrical characterization.....	116
5.2	A photograph of the edges of a (used) Si wafer showing chips in the substrate.....	119
5.3	Energy level diagram for Alq <sub>3</sub> devices and the J-F characteristic measured from one such device.....	121
5.4	Valence band spectra measured by XPS for FeP2 and FeP3 films.....	124
5.5	J-F characteristics for four Si/Al/LiF/FeP3/LiF/Al junctions.....	126
5.6	Temperature dependence of the J-F characteristic of one junction of a Si/Al/LiF/FeP3/LiF/Al device.....	128
5.7	Optical micrograph of a granular FeP2 film (100 nm nominal thickness) on Si and covered by a 100 nm Pb film.....	132
5.8	A 20 x 20 $\mu\text{m}^2$ AFM image of a 61 nm FeP2 film grown by sequential deposition and annealing of four layers.....	134
5.9	Optical micrographs taken through the Raman microscope of FeP2 films grown in four layers by sequential deposition/annealing steps.....	135
5.10	Temperature dependence of the J-F characteristic of Junction 1 of a Si/Al/FeP2/Al device with a 61 nm FeP2 layer grown in multiple successive depositions.....	137

5.11	Temperature dependence of the J-F characteristic of Junction 2 of a Si/Al/FeP2/Al device with a 61 nm FeP2 layer grown in multiple successive depositions.....	138
5.12	Temperature dependence of the J-F characteristic of Junction 3 of a Si/Al/FeP2/Al device with a 61 nm FeP2 layer grown in multiple successive depositions.....	139
5.13	Temperature dependence of the J-F characteristic of one junction of a Si/Al/LiF/FeP2/LiF/Al device with an 83 nm FeP2 layer grown in multiple successive depositions.....	142

# CHAPTER 1

## INTRODUCTION

### 1.1 Spin-Crossover Phenomena

The term spin-crossover (SCO) refers to a change in the electronic spin state of a molecule that occurs in response to an external stimulus. The term canvases an array of phenomena with varying mechanisms. In general usage however, and in this work, SCO is used to refer specifically to the change in d-orbital electron configuration that can occur for  $d^2 \rightarrow d^8$  transition metal complexes. By far, the most common SCO complexes are  $d^6$  Fe(II) complexes with octahedral arrangements of N-donor ligands and the usual applied stimulus is a change in temperature.<sup>1</sup> The following discussion will be limited to such complexes.

In the absence of any ligand field, the five d-orbitals of Fe(II) are degenerate. As ligands are brought near the metal center from six sides in an octahedral arrangement, the pseudo-spherical field imposed splits the d-orbitals into three ( $d_{xy}$ ,  $d_{xz}$ ,  $d_{yz}$ ) lower energy  $t_{2g}$  and two ( $d_z$ ,  $d_{x^2-y^2}$ ) higher energy  $e_g$  orbitals. Two possible spin states result depending on the magnitude of the ligand field splitting of the  $t_{2g}$  and  $e_g$  orbitals,  $\Delta_o$ . For Fe(II), when the two sets of d-orbitals are close in energy, four electrons occupy the lower set, two occupy the higher set, maximum spin multiplicity is achieved in accordance with Hund's rule, and the total spin of the  $^5T_2$  configuration is 2. When  $\Delta_o$  is greater than the spin pairing energy,  $\Pi$ , all six electrons fill the  $t_{2g}$  orbitals and the total spin of the  $^1A_1$  configuration is 0.

The question arises as to the electron configuration of complexes with ligands of intermediate field strength, i.e. what happens when  $\Delta_O = \Pi$ ? Occasionally it is mistakenly stated that it is under this condition that SCO occurs. In fact, the condition does not occur for the ground state equilibrium configurations.<sup>2</sup> That this must be so becomes obvious when one considers that  $\Delta_O$  varies as  $(r_{\text{Fe-N}})^{5-6}$ , where  $r_{\text{Fe-N}}$  is the metal-ligand equilibrium bond length for Fe(II) metal complexes with N-donor ligands in the octahedral field (assumed symmetric). Because the  $e_g$  antibonding orbitals are populated in the high spin (HS)  $^5T_2$  configuration,  $r_{\text{Fe-N}}$  is larger than for the same complex in the low spin (LS) state. Typically, the Fe-N bonds are longer by about 0.2 Å.<sup>3</sup> Consequently,  $\Delta_O$  is larger for the HS state and neither  $\Delta_{O,HS}$  nor  $\Delta_{O,LS}$  are equal to  $\Pi$ . Instead, SCO is likely to occur when  $\Delta_{O,HS}$  and  $\Delta_{O,LS}$  are as close as possible to  $\Pi$  and the condition  $\Delta_{O,HS} < \Pi < \Delta_{O,LS}$  is met.

The configuration coordinate diagram in Figure 1.1 illustrates these principles. The two potential energy curves for the different d-orbital electron configurations,  $^1A_1$  and  $^5T_2$ , are displaced on both the vertical axis, representing potential energy,  $E$ , and the horizontal axis which represents  $r_{\text{Fe-N}}$ . Only when the Fe-N bonds stretch from equilibrium do the potential energy curves intersect. Note that the LS state is shown to have a lower potential energy at equilibrium. The LS state must be the quantum mechanic ground state of a complex in order for that complex to undergo SCO, at least by thermal activation. This is because SCO is an entropically driven process. To understand how the SCO is affected by an increase in temperature it is necessary to consider the difference in the free energies between the HS and LS states

$$\Delta G_{\text{HS-LS}} = \Delta H_{\text{HS-LS}} - T\Delta S_{\text{HS-LS}} \quad (1.1)$$

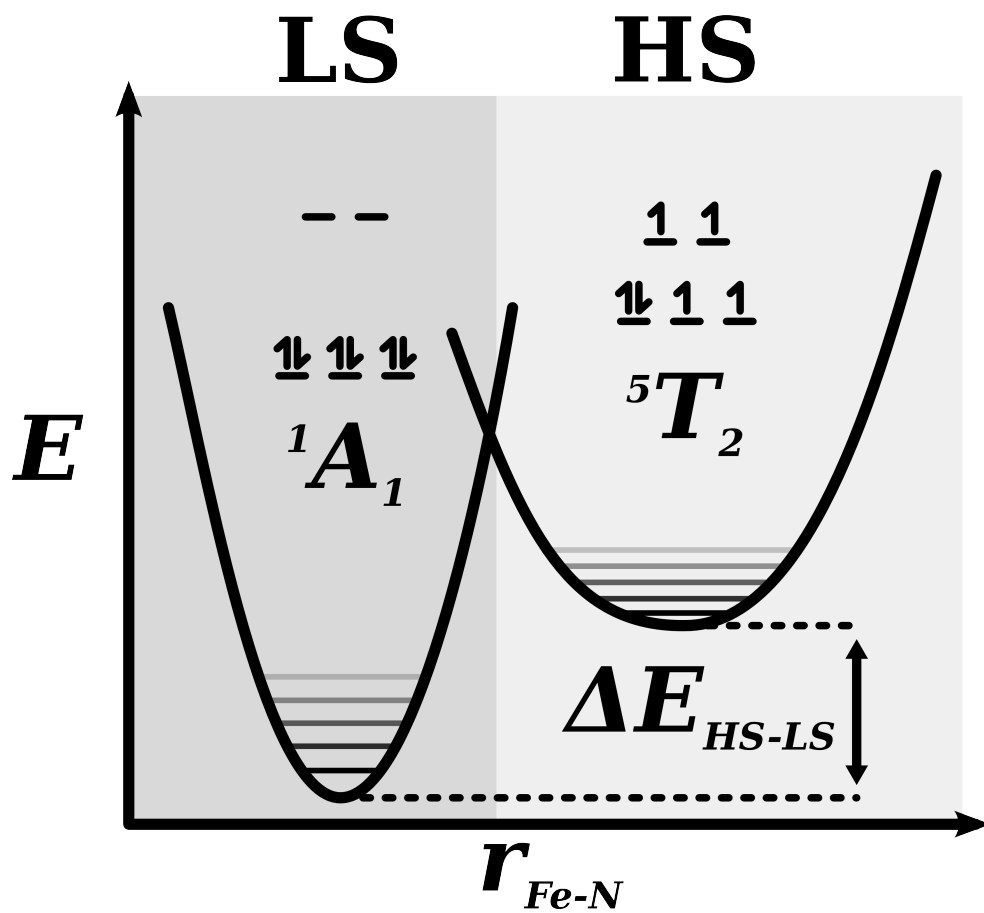


**Figure 1.1.** SCO configurational coordinate diagram showing the potential energy,  $E$ , for the LS ( ${}^1A_1$ , shaded dark) and HS ( ${}^5T_2$ , shaded light) states. The difference in energy between the two states is  $\Delta E_{HS-LS}$ . The position of the minimum of each potential energy curve on the horizontal axis represents the length of the Fe-N bonds at equilibrium,  $r_{Fe-N}$ , for the given d-orbital electron configuration shown inset on each curve.

where  $\Delta H_{\text{HS-LS}}$  is the difference in enthalpies and  $\Delta S_{\text{HS-LS}}$  the difference in entropies between the two states. The enthalpic contribution,  $-T\Delta S_{\text{HS-LS}}$ , causes  $\Delta G_{\text{HS-LS}}$  to transition from a positive value to a negative value as temperature increases. This happens because the entropy of the HS state,  $\Delta S_{\text{HS}}$ , is greater than its LS counterpart. The free energy of the HS state,  $\Delta G_{\text{HS}}$ , decreases more quickly than that for the LS state,  $\Delta G_{\text{LS}}$ , eventually becoming the lesser of the two. At this point,  $\Delta G_{\text{HS-LS}}$  is negative and the HS  $^5T_2$  configuration becomes the thermodynamic ground state. The larger entropy of the HS state originates from the electronic entropy (e.g. higher spin multiplicity) and from the vibrational entropy (e.g. greater density of vibrational states and longer bonds).

The evolution of  $\Delta G_{\text{HS-LS}}$  is calculated and plotted for a real SCO complex,  $\text{Fe}(\text{phen})_2(\text{NCS})_2$  (FeP2) in Figure 1.2. The values of  $\Delta H_{\text{HS-LS}} = 8607 \text{ J/mol}$  and  $\Delta S_{\text{HS-LS}} = 48.8 \text{ J/mol}\cdot\text{K}$  come from heat capacity measurements made by Sorai and Seki.<sup>4</sup> At a critical temperature,  $T_c \approx 176 \text{ K}$ ,  $\Delta G_{\text{HS-LS}}$  is equal to zero and the two spin states are degenerate. The ratio of the fraction of HS molecules,  $\gamma_{\text{HS}}$ , to the fraction of LS molecules,  $\gamma_{\text{LS}}$ , is given by the van't Hoff equation

$$\gamma_{\text{HS}} / \gamma_{\text{LS}} = \exp(-\Delta G_{\text{HS-LS}} / k_B T) \quad (1.2)$$

where  $k_B$  is Boltzmann's constant. At the critical temperature, where  $\Delta G_{\text{HS-LS}}$  is zero, the right hand side of Equation 1.2 evaluates to unity. Necessarily,  $\gamma_{\text{HS}} = \gamma_{\text{LS}}$  at this temperature, i.e. 50% of molecules are in the HS state and 50% are in the LS state. For this reason, the critical temperature is also called  $T_{1/2}$ . However, the formal definition of  $T_{1/2} = T_c$  is not always experimentally useful because the relative fractions of HS and LS molecules may be unknown exactly or a portion of molecules in an otherwise SCO-active material may not undergo SCO at any temperature.<sup>5</sup> The

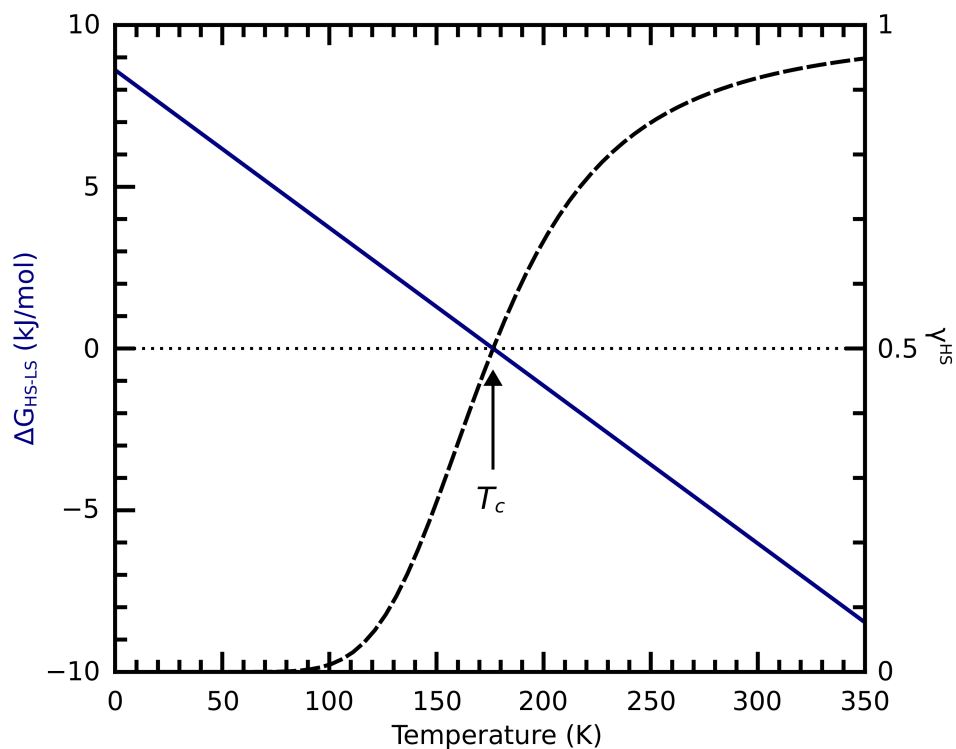


**Figure 1.2.** The change in the difference in the free energies between the HS and LS states ( $\Delta G_{\text{HS-LS}}$ ) vs. temperature (solid line, left axis) calculated using  $\Delta H_{\text{HS-LS}} = 8607 \text{ J/mol}$  and  $\Delta S_{\text{HS-LS}} = 48.8 \text{ J/mol}\cdot\text{K}$  for FeP2 from Ref. 4. As the temperature increases the fraction fo molecules in the HS state,  $\gamma_{\text{HS}}$  (dashed line, right axis), increases from 0 to 1. At a critical temperature,  $T_c$ ,  $\Delta G_{\text{HS-LS}} = 0$  and  $\gamma_{\text{HS}} = 0.5$ .

latter case leads to larger than expected residual HS/LS fractions even at very low and very high temperatures. Instead,  $T_{1/2}$  is often taken as the point of inflection in the SCO plot (however it is determined), i.e. the point at which 50% of the SCO-active molecules have switched. Additionally, two values of  $T_{1/2}$ , one upon cooling and one upon warming, will be observed at temperatures higher and lower than  $T_c$  for molecules which exhibit a hysteresis in their SCO curves.

The behavior predicted by the van't Hoff equation holds only for materials whose intermolecular interactions are weak or fleeting. For example, most solutions of SCO molecules display this type of behavior, as do solid solutions in which the concentration of the SCO-active species has been reduced.<sup>6,7</sup> In undiluted solids, molecular packing cannot be ignored. As stated above,  $r_{\text{Fe-N}}$  is significantly higher for the HS form of a complex than for the LS form. Upon switching, a molecule contracts or expands and the structural change is communicated to neighboring molecules via the elastic interactions between them. Those molecules feel a change in effective lattice pressure and may be induced to switch in concert. The efficient communication of structural changes is termed cooperativity and strongly affects the observed SCO curve (Figure 1.3). For solids which exhibit a high degree of cooperativity, the SCO event occurs abruptly rather than gradually, often over the course of only a few K. As the temperature of the system is increased or decreased the current spin state of the material is stabilized by the cooperative interactions between molecules. At the transition temperature, the entire material switches almost in unison and a discontinuity is observed in the SCO curve. If cooperativity is particularly strong and domain size is large, the material might resist switching even past the transition temperature and supercooling and superheating are observed. This results in a hysteretic SCO curve where  $T_{1/2}$  is different for either direction of temperature change. It should be noted though, that with any thermodynamically

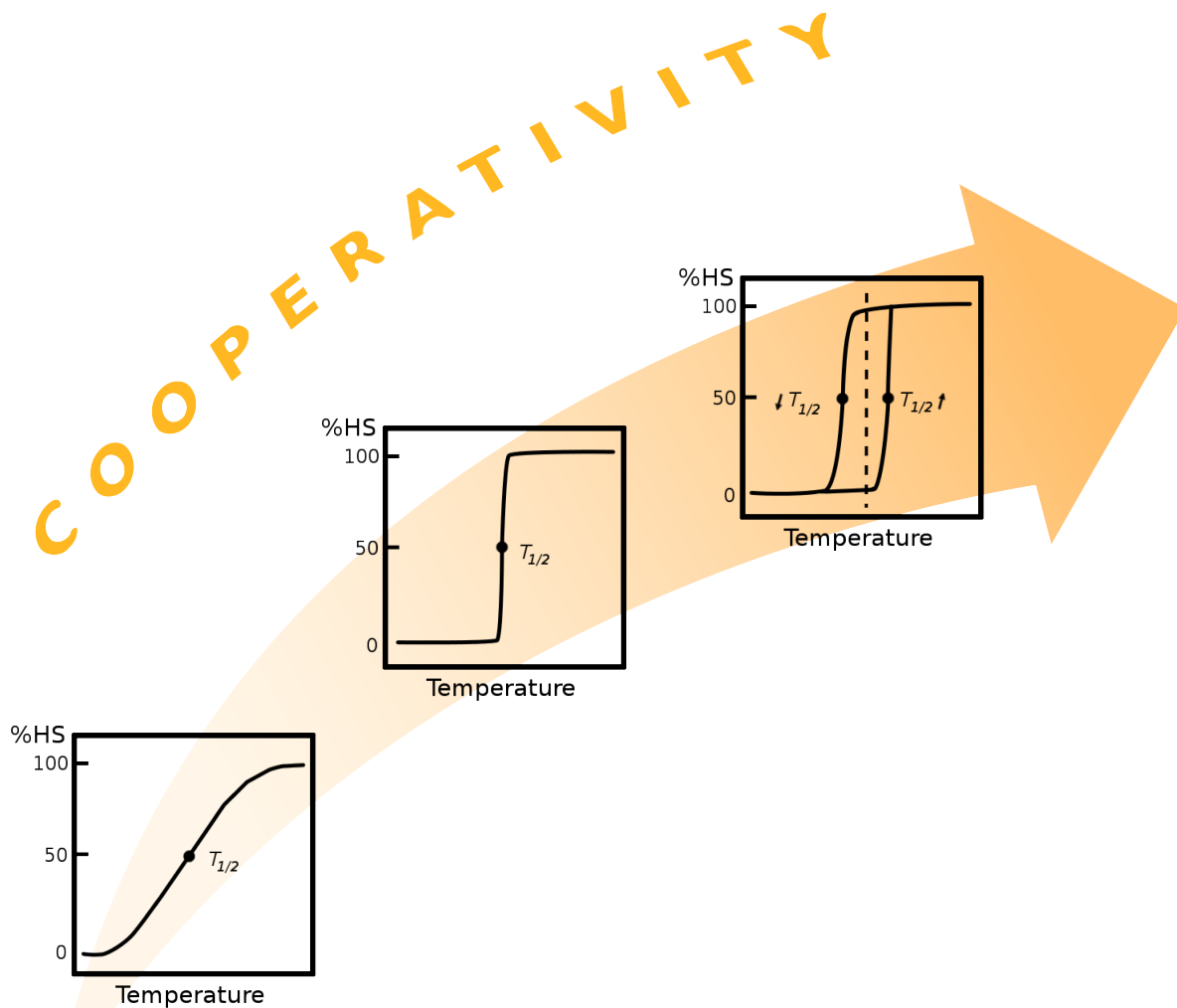


**Figure 1.3.** The continuum of SCO behaviors observed depending on the extent of cooperative effects in the lattice. When cooperativity between molecular centers is low, SCO occurs as a gradual process. As cooperativity is increased, the spin transition becomes more abrupt. When cooperativity is very high and efficient communication occurs across large domains, an hysteric spin transition can result in which the transition temperature differs depending on the direction of the temperature change.

favored process slowed by an activation energy, SCO is a kinetically limited process. The temperature scanning rate of the experiment can influence the width of the hysteresis.<sup>8</sup> Another source of hysteresis lies in the crystallographic phase changes (i.e. changes in space group) that sometimes occur simultaneously with the SCO event.<sup>5</sup> Bistability is also possible at very low temperatures (typically 0 → 50 K) where cooperative resistance to switching can prevent relaxation back to the LS ground state after optical excitation to the HS state. This process is termed light-induced excited spin state trapping, or LIESST.<sup>9</sup>

There are two primary changes associated with SCO that manifest themselves in myriad ways observable by experiment. These are the change in magnetic spin state caused by the population of the  $e_g$  orbitals and the lengthening of the metal-ligand (e.g. Fe-N) bonds that result from the antibonding character of those orbitals. The first change, most directly impacts the magnetic properties of a material - observable by magnetometry, Mössbauer spectroscopy, and magnetic resonance techniques (NMR and EPR) - but also increases the magnitude of spin-orbit coupling within the complex. This shows up time and again as small perturbations in other properties, such as the degree of multiplet splitting in photoelectron spectra. Ultimately, control of the spin state might form the basis for binary memory storage or influence spin-polarized transport through a material. More pervasive is the impact of the change in metal-ligand bond distance. The decrease in molecular volume imposes a structural contraction on the rest of the crystal lattice and the leads to the cooperative nature of the spin transition. Diffraction techniques (x-ray, electron, and neutron diffraction) provide a straight-forward means to monitor the SCO event, even though a classic phase change does not usually occur. The shortened metal-ligand separation changes the energy structure of the molecule as well. The structural and energetic changes are revealed through

most spectroscopies, including UV-Vis and diffuse reflectance, fluorescence, FT-IR and Raman, x-ray (XAS, EXAFS, and XANES), and photoelectron (XPS, Auger, and UPS) spectroscopies. SCO has even been observed by more specialized analytical methods such as muon spin relaxation, nuclear forward scattering, and positron annihilation spectroscopy. Recently, the nanometer and sub-nanometer resolution of scanning probe techniques such as AFM and STM have made it possible to witness the structural changes associated with SCO directly.

The effects of SCO, which at its heart involves two simple events, are ubiquitous. Any new understanding in the field of SCO research has the potential to impact countless fields within chemistry and physics.

## **1.2 Spin-Crossover at the Micro- and Nanoscales**

In order to take advantage of the peculiar properties of SCO materials in real-world applications, they must be prepared on a scale compatible with modern devices. First and foremost, this requires that fabrication methods and compatible materials be identified and refined. Most applications will require SCO materials that are bistable under typical operating conditions. That is to say, target materials are those that display a wide hysteresis centered around room temperature. Modern technology is dominated by Si-based electronics. Adoption of SCO materials in cutting edge technologies requires that they can meet the requirements of the production methods of these electronics. Ideally, it should be possible to pattern them as features whose dimensions are less than 100 nm. The question naturally arises as to whether the properties and effects associated with the SCO phenomenon are retained at such small scales. The second goal of SCO research at the nanoscale is therefore to understand how a reduction in size influences SCO behavior.

With the aid of only a microscope, much can be learned by simply observing visually the spin transition as it occurs in single crystals.<sup>10-13</sup> This is possible because many SCO complexes display a color that is dependent on the spin state, i.e. they are thermochromic. Such experiments established very clearly and with photographic evidence that the SCO event proceeds through a process of nucleation and growth. Nucleation begins at defect sites within a crystal and propagate at a finite rate.<sup>11,12</sup> With extremely precise temperature control, it is even possible to control the position of the transition front in high quality crystals. The transition can be halted in a biphasic state as well.<sup>13</sup>

Many of the early reports of SCO materials studied at scales beyond those accessible to simple microscopes were attempts to form thin films by the Langmuir-Blodgett (LB) technique.<sup>14-17</sup> Often, a SCO complex had to be modified by attaching long alkane chains to its ligands in order to form stable monolayers atop polar subphases like water. Fortunately, modification did not prevent SCO from occurring within the LB films. In at least one case, the film was SCO-active where the bulk material was not.<sup>14</sup> The LIESST effect was confirmed in thin films for the first time in LB films based on a modified form of  $\text{Fe}(\text{bipy})_2(\text{NCS})_2$ .<sup>17</sup> However, SCO in LB films can be more gradual than in the bulk phase and exhibit incomplete switching. Nonetheless, these early studies proved that SCO persisted in materials with the reduction of one dimension.

Since that time, many other approaches to forming thin films have been demonstrated. Very thin films can be assembled layer by layer by successive submersion in solutions of the relevant cations and anions in the process known as multiple sequential assembly, or MSA.<sup>18-20</sup> One of the consequences of growing films from aqueous solution is the possible inclusion of waters of hydration which can have strong effects on the SCO characteristics of a material, namely the

transition temperature and abruptness of the transition.<sup>20</sup> Other solution-based film processing techniques include spin-coating, drop-casting, and soft lithography. In these methods, organic solvents with high vapor pressures and short drying times are preferred over water. The films produced are typically much thicker than those made by MSA, especially for drop-casting. Soft-lithography methods have the advantage that patterning is an inherent part of the process. Studies of small patterned squares and circles have shown that SCO can exist in these one-dimensional features as well.<sup>21-23</sup> Stamps can be made in a cost-effective fashion from PMMA and in one unusual case, an onion membrane was shown to be effective.<sup>24</sup> The size limit to soft lithographic techniques is on the order of hundreds of nanometers which should be suitable for many applications.<sup>22</sup>

Probably the most important film processing technique, in the context of modern electronics fabrication, is that of physical vapor deposition. However, the technique imposes special requirements of the materials to be deposited. They must have adequate vapor pressure and they must endure the high temperatures involved in sublimation without decomposing or undergoing unfavorable reactions. In order for molecules to be sublimed intact, they should be neutral, covalently bonded complexes. Only a handful of SCO materials have been shown to meet all of these requirements, most being Fe(II) complexes containing tetrazole- and pyrazolyl-based ligands. One of the first reports of vapor deposition of a SCO complex is that of FeP2, the molecule that is the subject of this work.<sup>25,26</sup> In his Ph.D. thesis, Bernien deposited FeP2 at a coverage of only a few monolayers (ML) on Cu.<sup>25</sup> Significant contamination of nitrogen-containing organic species, possibly including phen, was always present. X-ray absorption spectroscopy revealed a mixture of HS and LS species present at room temperature (above the spin transition temperature of the

material) but also that the HS component was reduced on cooling as expected. In another report, films of thicknesses between 7 and 530 nm were deposited with no mention of decomposition or contamination.<sup>26</sup> The spin transition characteristics of the bulk FeP2 were preserved in those films.

Because physical vapor deposition allows incredibly precise control of the deposition rate, materials can be deposited at sub-monolayer coverage and studied in the limit of isolated molecules. Miyamachi et al. found that for sub-monolayer coverages of FeP2 on Cu, both LS and HS states were present in a nearly 1:1 ratio.<sup>27</sup> The molecules on Cu could not be induced to switch spin states by application of a bias from the STM tip, but for those deposited on CuN, switching in both directions could be affected by application of biases of opposite sign. Thus it was shown that the interaction of molecules with the substrate surface could dominate, even eliminate, SCO behavior. In order to retain SCO properties at ultra-low coverages a substrate that shows little interaction with the deposited material may be necessary. Success has been found with highly ordered pyrolytic graphite (HOPG) substrates.<sup>28, 29</sup>

In recent years, the field of SCO research has increasingly focused on the nanoscale. More thorough reviews than can be offered here are found in Ref.'s 30,31, and 32. Some general conclusions have been identified by research at this scale. 1) SCO persists down to the limit of a single isolated molecule. 2) Direct contact with the substrate can lead to mixed spin states and hindered switching. 3) The spin-transition typically occurs more gradually, at lower temperatures, and with a more narrow hysteresis. 4) Modification of SCO properties for nanomaterials vs. bulk materials is correlated with the increase in the surface-to-volume ratio and increased dominance of surface molecules whose SCO behavior differs from molecules in the bulk. This last point has been verified by both theory and experiment.<sup>33,34</sup>

### 1.3 Spin-Crossover and Electrical Conduction

Many SCO materials are molecular solids in which only weak van der Waals forces bind the molecules. Especially for amorphous solids (most films), delocalization of frontier orbitals is of limited range in comparison to inorganic, covalent semiconductors. Conduction in these materials is relatively weak and SCO materials are expected to fall into the class of materials known as organic semiconductors. Without a typical semiconductor valence and conduction band structure, charge carriers are highly localized on single molecules in this class of materials. Conduction is expected to occur via "hopping" of charge carriers across/through potential barriers into nearby molecules. Unlike band transport, which is thermally deactivated, hopping transport is a thermally activated process, and current increases strongly with temperature. The transport through SCO-active coordination polymers might occur primarily along polymer chains with hopping between the chains. Polymeric materials might have transport properties intermediate between molecular hopping and band transport.

The property of a material that determines what magnitude of current,  $I$ , will flow through the material for a given applied electric field,  $F$ , is the conductivity,  $\sigma$ .

$$I = \sigma F \quad (1.4)$$

The conductivity is limited principally by two factors: the number of intrinsic charge carriers within the material,  $n$ , and the mobility of the material  $\mu$ .

$$\sigma = n q \mu \quad (1.5)$$

where  $q$  is the elementary charge. For traditional inorganic semiconductors, conductivity is

controlled primarily by manipulating the number of charge carriers in a material, e.g. by doping. For organic semiconductors, which are very nearly insulators, the number of intrinsic charge carriers is negligible and nearly all of the transported carriers must be injected from the electrodes. The vital property of organic semiconductors is thus the mobility which simply relates the carrier drift velocity (the speed at which charges travel),  $v$ , to the applied electric field.

$$v = \mu F \quad (1.6)$$

The mobility is different depending on the particular charge carrier. For example, for tris(8-hydroxyquinolato)aluminium ( $\text{Alq}_3$ ), the electron mobility is two orders of magnitude higher than the hole mobility.<sup>35</sup> The overall mobility is the sum of the two and in many cases, as is the case for  $\text{Alq}_3$ , the measurement of only the major carrier mobility gives a good approximation of the overall mobility.

The two fundamental aspects of the SCO event, the change in spin state and the change in molecular geometry, might be expected to affect electrical current in three ways. First, interaction between the spins of charge carriers and unpaired spins of a HS material might cause scattering of those carriers. If scattering is spin-dependent, a HS material might act as a spin filter. Even though hopping transport is expected to occur through primarily ligand-centered orbitals and not through the metal-centered orbitals (except perhaps for coordination polymers), coherent quantum transport calculations of a single molecule of the SCO complex  $[\text{Fe}(\text{btp})_2(\text{NCS})_2]$  (btp = 3-(2-pyridyl) [1,2,3]triazolo[1,5-*a*]-pyridine) revealed that the highest occupied molecular orbital (HOMO) levels are composed primarily of contributions from the  $t_{2g}$  orbitals.<sup>36</sup> The occupancy of the HOMO in the HS state is of  $\beta$ -electrons reflecting the unfilled nature of the  $t_{2g}$  orbitals. The unoccupied

states near the Fermi energy also originate primarily from  $t_{2g}$  bands. The conclusion was reached that transport, either through the HOMO or lowest occupied molecular orbital (LUMO) should be highly polarized when the molecule is in the HS state.

Second, the change in geometry affects strongly the energies of the molecular orbitals. Movement of the frontier orbitals nearer to the Fermi level should increase conduction. For  $[\text{Fe}(\text{btp})_2(\text{NCS})_2]$ , the density of states for both occupied and unoccupied orbitals close to the Fermi level was calculated to be higher for the HS state. Similar calculations on two SCO complexes of the form  $[\text{FeL}_2]^{2+}$  ( $L = 2, 2':6, 2''$ -terpyridine or  $L = 2,6$ -bis(pyrazol-1-yl)) reached the same general conclusions and predict that current in the HS state may be as much as three orders higher.<sup>37</sup> At the electrode interfaces, efficient carrier injection requires that the HOMO (for hole injection) or LUMO (for electron injection) be of similar energy as the Fermi energy (work function) of electrons in the metal. A change in the energies of the frontier orbitals upon SCO can therefore also be imagined to affect the current by modulating the injection efficiency.

Finally, the change in volume that occurs during SCO might simply alter the dimensions of the active layer of material. Many conduction mechanisms are severely dependent on the thickness of the transport layer such that a small change in thickness could have a measurable impact on current through a device.

The interplay of SCO and electrical properties has only begun to be considered heavily within the last decade (for a review see Ref. 38). Possibly the earliest investigation of the coupling of SCO and electrical conductivity is that by Takahashi et al. in 2006.<sup>39</sup> For single crystals of the novel complex  $[\text{Fe}(\text{qsal})_2][\text{Ni}(\text{dmit})_2]_3 \cdot \text{CH}_3\text{CN} \cdot \text{H}_2\text{O}$  (where qsal is the deprotonated form of *N*-(8-quinolyl)salicylaldehyde and dmit = 4,5-dithiolato-1,3-dithiole-2-thione) a small hysteresis

was noticed in the temperature-dependent resistivity ( $\sigma^{-1}$ ). The complex experiences a very gradual spin transition that stretches from 300 to 50 K, but a small hysteresis occurs between 120 and 90 K. The hysteresis of the resistivity occurred in this same temperature range and the coincidence was taken to indicate that the resistivity was reacting to the change in spin state. Within the hysteresis, resistivity was higher during heating, where the LS component is greater. A similar result would be found for another  $\text{Fe}(\text{R-qsal})_2^+$  based material except that an even larger hysteresis was observed for the conductivity.<sup>40</sup>

A year later, another Japanese group reported the first vapor deposition of and vertical junction device incorporating a SCO complex, this time  $[\text{Fe}(\text{dpp})_2](\text{BF}_4)_2$  (dpp = 2,6-di(pyrazolyl)pyridine).<sup>41,42</sup> The spin transition in this material ( $T_{1/2} \approx 260$  K) is much more abrupt than the last. On cooling, the resistance of the thin film increases slowly, peaking near 255 K. It then slowly declines before increasing suddenly again below 230 K. The small increase of the resistivity near the spin transition temperature was taken as evidence of the relationship between the resistance and the spin state. In a follow-up paper, the group showed that by doping the material in an electroluminescent layer, the electroluminescence could be switched on and off by heating and cooling the device across  $T_{1/2}$ .<sup>42</sup> The effect was proven not to be simple quenching of excitons, but the mechanism by which the SCO material prevents the electroluminescence of the biased device was not established conclusively.

Chronologically, the next report to appear was that of Shi et al. in which the I-V characteristic for a vapor deposited thin film of the title complex,  $\text{FeP}_2$ , was given.<sup>26</sup> For the first time, a mobility was reported for a SCO complex, though only for the HS state. The authors found the mobility to be on par with other typical organic semiconductors, e.g.  $\text{Alq}_3$ . The work by Shi et

al. largely served as the motivation for the work presented here. However, in the course of this endeavor, it was realized that the interpretation of the spectroscopic characterization in that work may be in error. These points are discussed throughout the chapters below.

In the time since these early accounts, research into the relationship between a material's electrical properties and SCO behavior have spanned in physical scale from bulk powders to the single molecule limit. When three different bulk preparations of  $[\text{Fe}(\text{Htrz})_2(\text{trz})](\text{BF}_4)$  (Htrz = 1,2,4-4H-triazole), in which the constituent crystallites differed in morphology, were pressed as powders or drop-casted films between two stainless steel electrodes, all produced temperature-dependent conductivities that were strongly correlated with the SCO event.<sup>43</sup> The conductivity of the LS state was as much as two orders higher than that of the HS state. This result is unexpected given the experiments already mentioned, both theoretical and empirical. Yet, the behavior was confirmed when the conductivities of nanoparticles ( $\sim 3 \mu\text{m}$ ) of the same material laid across gold electrodes were measured by the same group.<sup>44</sup> When the conductivity of a single 11 nm nanoparticle of  $[\text{Fe}(\text{Htrz})_2(\text{trz})](\text{BF}_4)$  was measured by a second group, the HS state was found to be more conductive, in opposition to the works just mentioned.<sup>45</sup> It is likely the case, though, that the mechanism of conduction in the single nanoparticle (e.g. tunneling) is not the same as it is in the larger nanocrystals. It is interesting to note that the behavior of the single nanoparticle is in agreement with the theoretical studies of single molecules. A fourth study of electrical conductivity for this material found that conductivity through  $\sim 650$  nm long nanoparticles improved significantly after polling them with higher bias.<sup>46</sup> The conduction mechanism might rely on the treatment of the sample and the conditions of the electrical characterization as well.

So far, the prediction made in theoretical works that the HOMO-LUMO gap should be

smaller for the HS state than for the LS state has been unequivocally confirmed by studies of ultra thin films and single molecules. Measurements of the HOMO density of states by UPS of a 7 nm SCO thin film and of the UPS and IPES of a 5 nm thin film of an analogous SCO material showed the HOMO-LUMO gap is increased in size for the LS state.<sup>47,48</sup> This same dependence of the HOMO-LUMO gap size on spin state was observed for differential conductance ( $dI/dV$ ) measurements made on bilayer and monolayer films, and on single molecules of the same complexes within an STM.<sup>49-51</sup> Finally, and importantly, some of these single molecule studies have demonstrated that it is possible to affect a change in spin state by application of an electric current or bias so long as the interaction with the surface is not too great.<sup>27,28,49,52</sup>

#### **1.4 Aims of this Work**

At the outset, the goal of this work was to investigate the sensitivity of electrical conduction through FeP2 films to the spin state of those films. FeP2 was chosen because this molecule has traditionally been at the forefront of SCO research and has served the community as standard reference. A review of the history of FeP2 research would be a review of SCO itself. Its SCO properties are by now well-established which will provide a firm foundation from which to explain any electrical conductivity effects. Identification of SCO-modulated electrical current could lead to applications incorporating SCO materials as passive electrical components. Identification of current- or voltage-induced SCO would make these materials useful as active components as well, with applications in the realm of memory storage, displays, etc. Since it was discovered that physical vapor deposition from FeP2 did not yield FeP2 films, the focus of this work became the identification and characterization of the films that were produced. Then, this knowledge would be

used to develop a successful method of obtaining FeP<sub>2</sub> films so that their electrical properties could be studied. A tertiary goal of this work was to improve the yields, convenience, and product material quality of the FeP<sub>2</sub> synthesis.

The characterization of the as-deposited films and the modified vapor-deposition technique for producing FeP<sub>2</sub> films have already been published.<sup>53</sup> The structural and electrical characterization of the FeP<sub>2</sub> films are the subjects of a forthcoming publication.

## CHAPTER 2

### METHODS, MATERIALS, AND SYNTHESSES

#### 2.1 Details of the Physical Vapor Deposition System

The physical vapor deposition system consists of a stainless steel domed chamber with a glass viewport, resistive heating elements for subliming materials, a quartz crystal microbalance (QCM) for monitoring deposition rates, associated vacuum pumps for maintaining the system at low pressure, and various accessories (Figure 2.1). Two shutters are operable from outside of the deposition chamber and allow the ability to quickly start/stop deposition to the sample surface as well as to cover samples in sequence in order that the film thickness may be varied among multiple samples in a single batch. Patterning of films on the samples was achieved by the use of thin Ti shadow masks (Figure 2.2). A high current power supply feeds electrical current to three electrodes, one being a common ground, that allow the selective heating of two different deposition boats during a single deposition. Another set of low power electrical feedthroughs were used here to provide power to a heater used to control substrate temperature. Additionally, feedthroughs for two thermocouples are present.

Film thicknesses reported by the QCM were independently verified by profilometry when possible (Dektak IIA). Standard densities and z-ratios were used for LiF and Al. Typical deposition rates were  $< 0.1 \text{ \AA/s}$  and  $1 \text{ \AA/s}$ , respectively. For FeP<sub>2</sub>, a z-ratio of 1 and density of  $1.5 \text{ g/cm}^3$  was used. These parameters were not optimized and tended to overestimate the film thickness by a

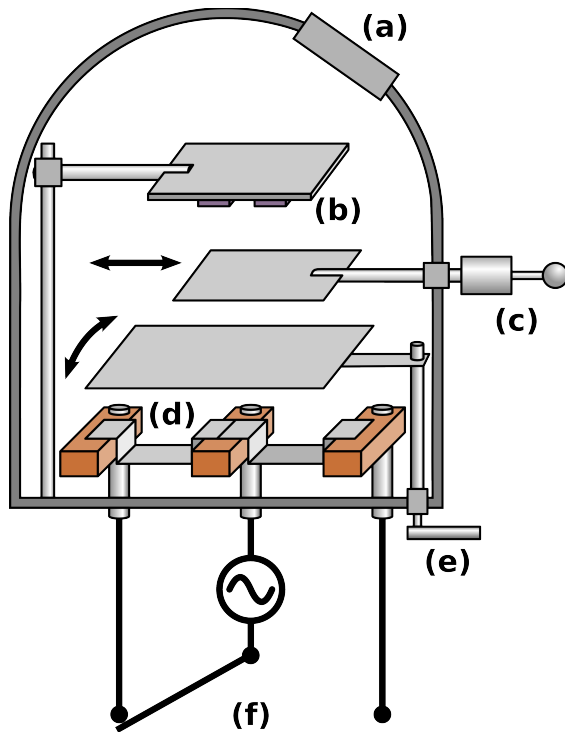
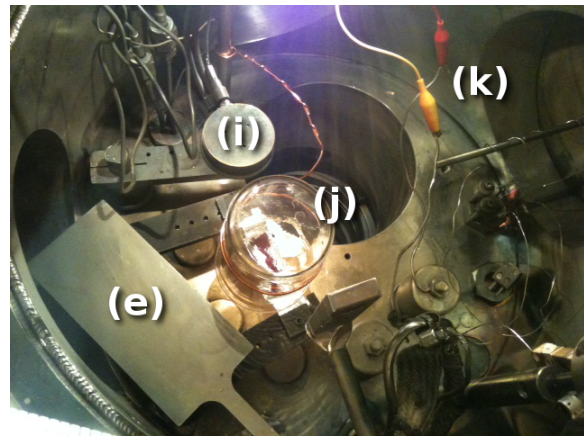
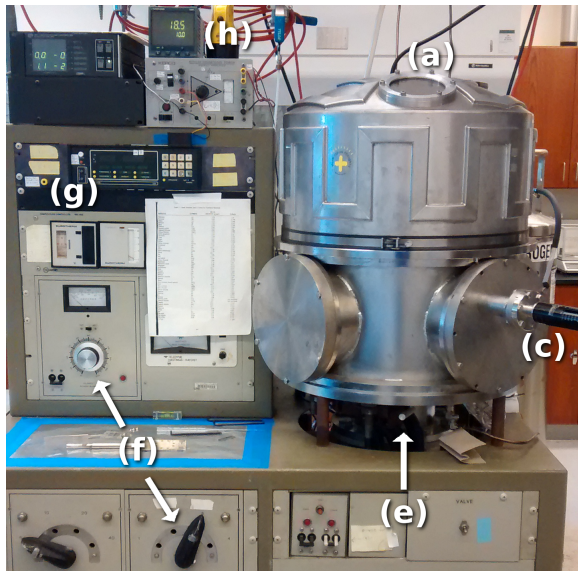


**Figure 2.1.** Details of the physical vapor deposition system. Clockwise from bottom-left corner are a schematic of the deposition chamber, the view from outside of the chamber, and the view inside the chamber seen through the top viewport window (with sample holder and primary shutter removed). The various components are labeled as:

- (a) viewport window
- (b) sample holder, optionally heated
- (c) secondary shutter, moves laterally
- (d) deposition boat
- (e) primary shutter, rotates in plane
- (f) high current power supply
- (g) QCM controller
- (h) temperature controller and power supply for sample heater
- (i) QCM sensor
- (j) beaker covering deposition boat (see Chapter 4)
- (k) electrical feedthroughs for sample heater

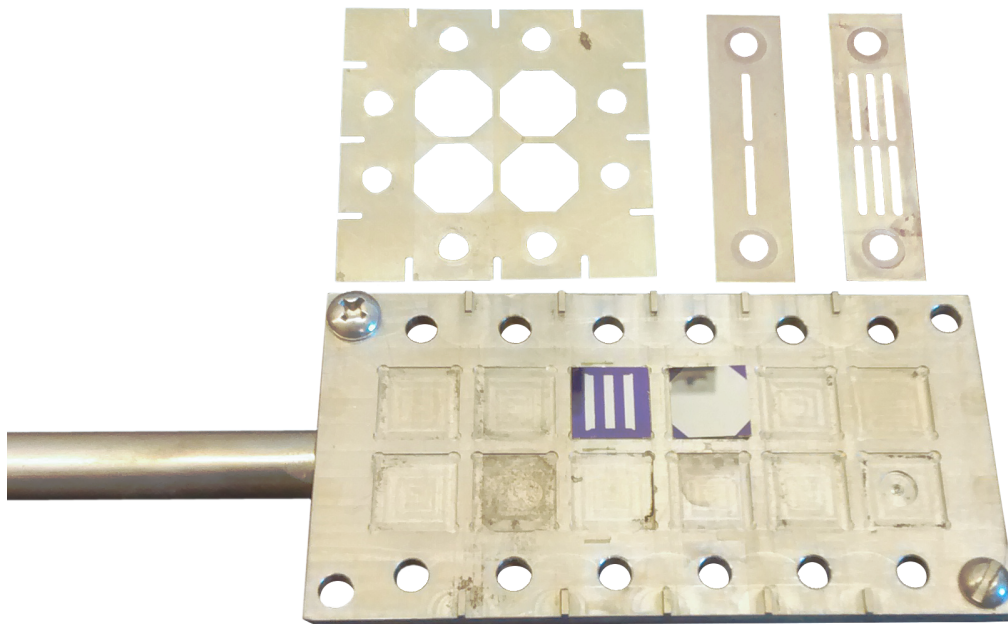


**Figure 2.2.** The Al sample holder used during deposition of films along with three shadow masks made of thin Ti. Two  $1 \times 1 \text{ cm}^2$  Si wafers are shown resting inside the sample holder. Each has had an Al film deposited through masks. Small nuts and bolts are used to attach the masks to the sample holder.

factor of two to three. Though the absolute deposition rate achieved when depositing from FeP2 was unknown, the rate was found to be difficult to control anyway (see Chapter 3).

Materials were deposited from tungsten boats. In the case of Al deposition, the boats used are coated with an Al<sub>2</sub>O<sub>3</sub> layer that prevents alloying with the boat. When FeP2 is deposited, boats were lined each time with clean Al foil so that charred material was not left on the deposition boat that was reused. A base pressure of 10<sup>-7</sup> Torr is achieved via an oil diffusion pump with a liquid nitrogen cooled cryotrap. Pressures during sublimation were maintained near 10<sup>-6</sup> Torr.

When samples were to be annealed in situ during or following the deposition, samples were clipped to a copper block with an internal cartridge heater (12V, 400W) made for this purpose. Sample temperatures were monitored by a thermocouple clipped to the surface of one of the samples. The sample heater was controlled by a PID temperature controller and powered by an operational amplifier. Glass sheets buffered the sample surfaces from the metal retaining clips preventing significant heat transfer through the clips and uneven heating. The pressure with which samples were held to the Cu heater was found to impact their surface temperatures greatly. In order to distribute the force from the clips evenly among samples, crumpled wads of Al foil were placed between the clips and the glass slides. These measures were found necessary to achieve uniform films and reproducibility within a batch and across depositions. Samples were allowed to cool to at least 30 °C before the chamber was opened following annealing. Cooling usually requiring several hours during which high vacuum was maintained. When depositing multiple layers from FeP2, samples were allowed to cool to 30 °C between successive depositions.

## 2.2 Details of the Electrical Characterization System

Within the custom-built electrical characterization system, samples are held under vacuum ( $10^{-2}$  Torr) in a small chamber and mounted on a copper cold head (Figure 2.3). Samples are cooled through conduction of heat through the cold head which is removed by the flow of He from a closed-cycle refrigerator. To achieve a desired temperature a small heating element balances the cooling from the chiller. A cryogenic temperature controller (Model 32B, Cryogenic Control Systems, Rancho Santa Fe, CA, USA) was used to set the temperature either manually or programmatically. For this purpose, a custom software interface was built. When the temperature was selected either at the controller or via the software interface the reading was monitored and stability was decided by the user. In this case, the temperature is assumed to be accurate to within  $\pm 2$  K. Alternatively, the temperature controller was operated through a Python script attached to graphing software. The script allowed careful control of the temperature to within  $\pm 0.5$  K.

Current-voltage (I-V) characteristics were measured with a general purpose source meter (Model 2400 Keithley Instruments, Cleveland, OH, USA). Sweeps were made starting at zero applied bias and increasing in magnitude. The resulting current at each voltage was recorded. When single sweeps were required, a custom-built software interface was used to program and read data from the sourcemeter. In later experiments, where sweeps were made as a function of temperature and experiments sometimes required 30 hours or more, the custom Python script mentioned above performed the scanning automatically at each temperature. There is no difference in scans measured in either way. The resistances of the measured devices were  $> 10^6 \Omega$  while the total resistance of wiring and contacts was found to be less than  $100 \Omega$ . As expected, measurement in a

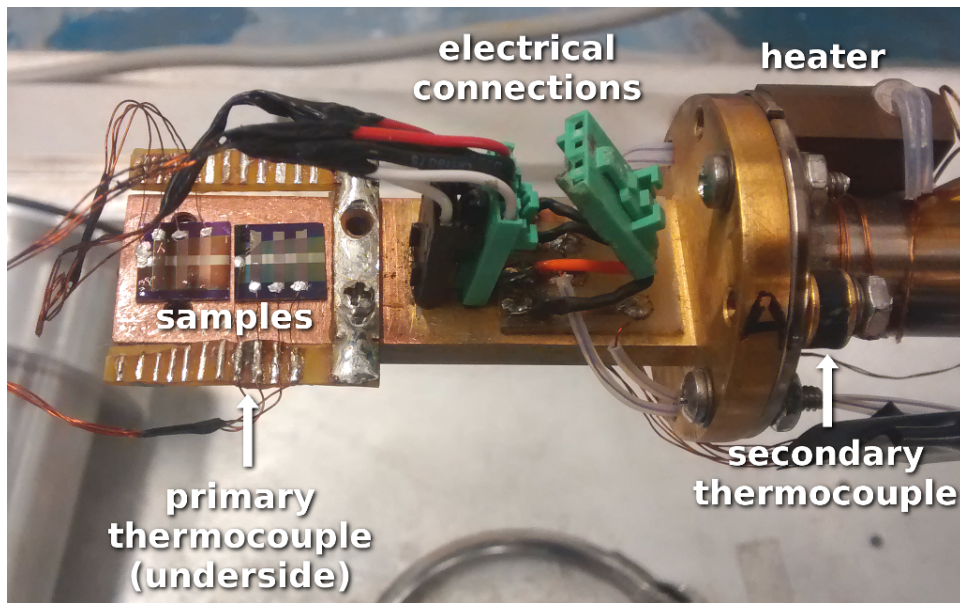
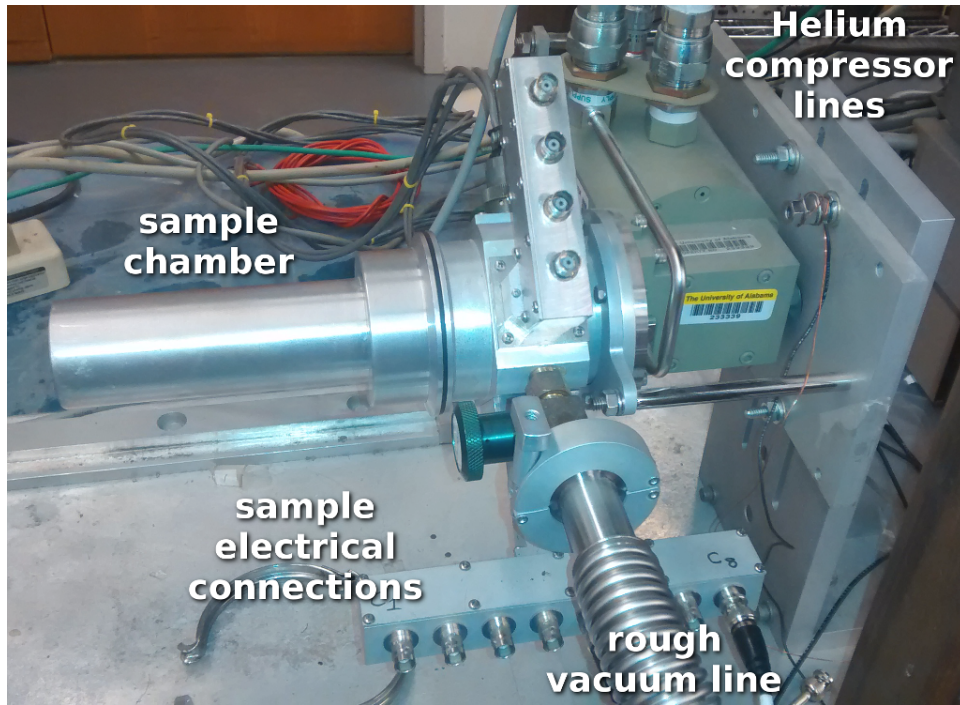


**Figure 2.3.** The cryostat used for making temperature-dependent electrical measurements (top). The samples are mounted to the cold head contained within the evacuated sample chamber (bottom). Not visible is the primary thermocouple located on the underside of the cold head.

4-wire configuration had no advantage over a 2-wire configuration and the latter was used here in order to use the limited electrical feedthroughs most efficiently.

### **2.3 Details of Other Instrumentation**

Thermogravimetric analyses (TGA) of the FeP<sub>2</sub> powder was performed using a TGA 2950 (TA Instruments, New Castle, DE, USA) under an air atmosphere and measured in a dynamic heating regime. The roughly 2 mg sample was heated from 20 to 400 °C under a constant heating ramp of 5 °C/min with a 30 min isotherm at 75 °C.

FT-IR spectra were collected in both transmission and ATR modes using a Jasco FT/IR-4100 spectrometer (Jasco Analytical Instruments, Easton, MD, USA) at 4 cm<sup>-1</sup> resolution. Typically, 256 scans were averaged. For transmission experiments, either KBr crystals or Si substrates were used. Raman spectra (Jobin Yvon LabRam HR800 UV, Horiba Scientific, Kyoto, Japan) were collected by sending the 632.8 nm laser light through the 10X, 50X, and 100X objectives of a confocal microscope. Powder samples were packed into small metal pans and rotated during analysis. Films could be analyzed without damage resulting from the laser by careful selection of the microscope objective and sampling time. The vibrational spectra presented in this work have been adjusted (baselines straightened, normalized) in order that they might be more conveniently plotted and interpreted.

UV-Vis absorption analysis was made with a Varian Cary 50 UV-Vis pseudo-double beam spectrophotometer (Agilent Technologies, Santa Clara, CA, USA). Ethanolic solutions of FeP<sub>3</sub> were recorded in quartz glass cuvettes. The spectrum of FeP<sub>2</sub> could not be collected because a suitable solvent could not be identified. Glass slides were used as substrates for thin films. X-ray

photoelectron spectra were collected using the Kratos Axis Ultra 165 spectrometer (Kratos Analytical, Manchester, United Kingdom) housed in the Central Analytical Facility at The University of Alabama which has a 165 mm mean radius hemispherical analyzer and 8 channeltron detectors. Samples were excited with monochromatic Al  $K_{\alpha}$  radiation (1486.6 eV) from an Al target (12 kV, 12 mA). Films were deposited onto conductive ITO-coated glass substrates or Al-coated Si substrates. Powders were scraped onto double-sided Cu tape. The offset of the C(1s) line from 285 eV was measured in high resolution spectra of the C(1s) region and this offset was applied to the other high resolution scans.

Magnetometry of the FeP2 film (300 to 500 nm estimated thickness) deposited on a 6 x 6 mm<sup>2</sup> Si wafer was performed at The University of New Orleans using an MPMS-XL superconducting quantum interference device (SQUID) magnetometer (Quantum Design, San Diego, CA, USA) with the DC head option. The applied field was 5000 Oe. Magnetic data was obtained in the condition of in-plane cooling in 1 K steps at a rate of 0.5 K/min. After analysis, the substrate was cleaned, measured independently, and its signal subtracted from that of the film. Measurement by SQUID of ~ 10 mg of FeP2 powder was performed at The University of Alabama also on an MPMS magnetometer. In this case, scans were collected every 10 K on cooling while a 1000 Oe field was applied.

AFM images of films grown on Al/LiF electrodes on Si wafers or on bare Si wafers were collected using a Digital Instruments 3100 Dimension AFM with a NanoScope IV controller (Bruker, formerly Veeco, Billerica, MA, USA). Images were taken with high aspect ratio probes (tip radius 10 → 15 nm) in the intermittent contact mode. Software processing of images was used to remove line scars and to level scans (<http://gwyddion.net/>).

## 2.4 [Fe(phen)<sub>3</sub>](SCN)<sub>2</sub>

In discussing FeP3 (Figure 2.4), it is perhaps appropriate to begin the discussion with the cation, [Fe(phen)<sub>3</sub>]<sup>2+</sup>, for it is the cation that dominates the properties of the molecule. Many [Fe(phen)<sub>3</sub>]<sup>2+</sup> salts exist and their chemistries are generally the same. The cation is known traditionally as ferriin. The oxidized, Fe(III) form of the cation is appropriately known as ferriin. The ferriin-ferriin redox couple forms the basis of a common redox colorimetric indicator system (Figure 2.5). Notably, ferriin-ferriin provides the means for visualizing the dynamic oscillations in the famous Belousov-Zhabotinsky reactions. In one novel application, the color changing ferriin-ferriin system was exploited as the active element in an electrochromic display.<sup>54</sup> By itself, ferriin is commonly found in analytical chemistry experiments as a means for detection of Fe(II). Upon dissolution of a sample containing Fe(II) (or Fe(III) with an appropriate reducing agent), addition of phen forms the ferriin complex immediately and quantitatively. The concentration of Fe(II) in the sample is then determined by measuring the absorption of the solution at  $\lambda_{\text{MAX}} = 510$  nm. This strong absorption band stems from a metal-to-ligand charge transfer excitation.<sup>55,56</sup> Only one crystal structure of the dithiocyanato complex exists in the Cambridge Structural Database.<sup>57</sup> In the trihydrate crystal, the complex is distorted from ideal octahedral geometry. FeP3 is chiral and the trihydrate crystal is racemic.

At all temperatures at which the complex is stable, it is found in a LS state. It must be noted however, that the strong ligand field imposed by the *tris*-phenanthroline coordination does not preclude SCO behavior, at least not as a single factor. By following the calculations in Ref. 58 it is possible to estimate that the HS state of FeP3 lies  $\sim 3500 \text{ cm}^{-1}$  above the LS state and SCO should

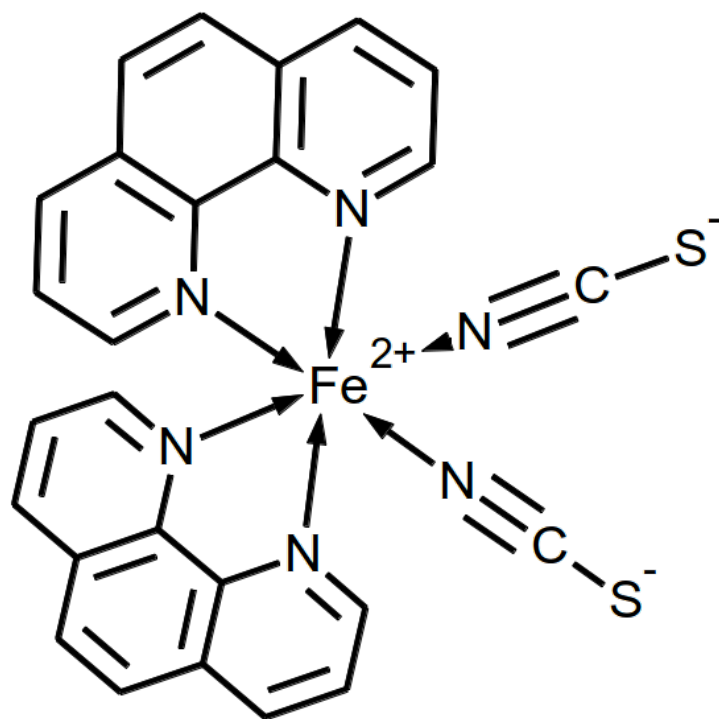
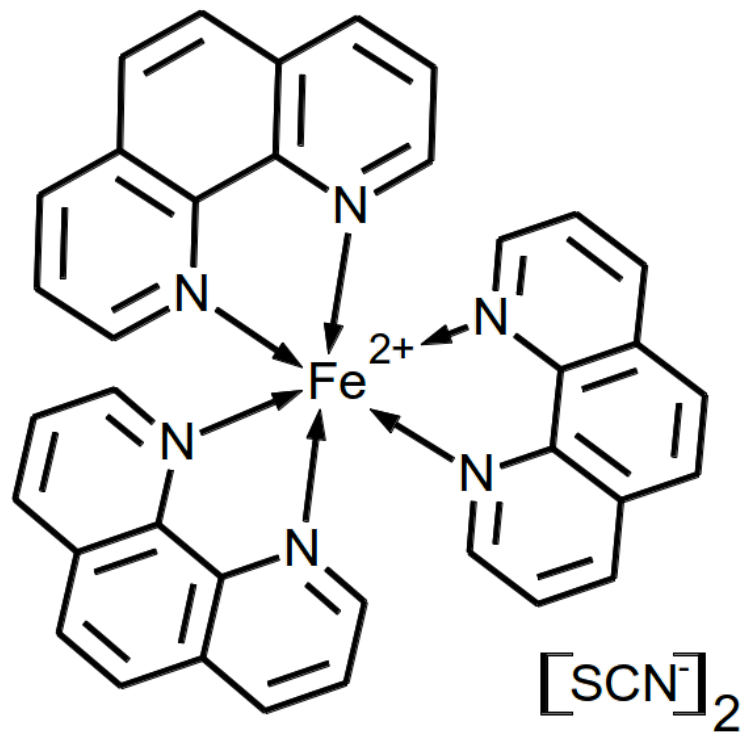


**Figure 2.4.** Molecular structures for FeP3 (*top*) and the title complex FeP2 (*bottom*).

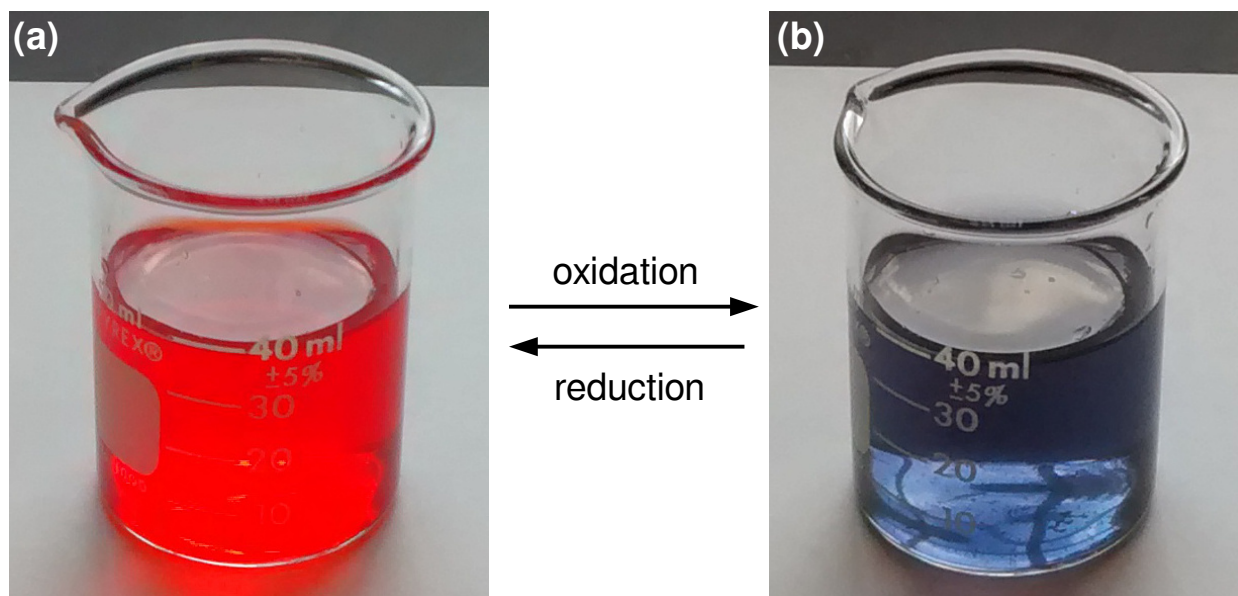


**Figure 2.5.** A ferriin solution (a) and the same solution after oxidation with  $\text{KMnO}_4$  at low pH to form a ferriin solution (b).

occur for the complex around 700 K.<sup>58</sup> Of course, such a high temperature is not accessible to this material. Still, it might be considered a starting point from which the spin transition temperature may be tuned by ligand modification. For example,  $[\text{Fe}(\text{2-me-phen})_3]^{2+}$  (2-me-phen = 2-methyl-phenanthroline) salts are SCO-active with spin transition temperatures below 300 K.<sup>59</sup> Apparently, the steric repulsion introduced by the methyl group lowers the ligand field to the necessary range for SCO to occur without thermal decomposition. One can imagine that with the right chemical modification,  $[\text{Fe}(\text{R-phen})_3]^{2+}$  based salts might display SCO even at room temperature. With proper crystal design, a hysteresis might even be introduced. Additionally, the HS state of  $[\text{Fe}(\text{phen})_3]^{2+}$  is at least optically accessible, though the lifetime is only on the order of nanoseconds.<sup>56,60</sup>

In this work, films of FeP3 will be deposited and used as organic semiconductors in vertical junction devices (see Chapters 3 and 5). This represents the first time that FeP3 has been used as an active layer in such a device. However, it is not the first ferriin-based material to find its way into the realm of vertical, thin film, transport measurements. In devices of the geometry ITO/ $[\text{Fe}(\text{phen})_3]\text{Cl}_2/\text{Al}$ , in which the organometallic film was spin-coated, the ferriin-based complex performed as a p-type semiconductor with a mobility of around  $1 \times 10^{-5} \text{ cm}^2/\text{V}\cdot\text{s}$ .<sup>61</sup> The mobility was found to be strongly temperature-dependent. Results remarkably similar to these are presented in Chapter 5 for FeP3.

## 2.5 $\text{Fe}(\text{phen})_2(\text{NCS})_2$

The role of the title complex (Figure 2.4) with respect to the development of the understanding of SCO phenomenon cannot be overstated. FeP2 was the first synthetically derived

SCO complex.<sup>62</sup> Since the discovery of its unusual magnetic behavior - an abrupt change in spin state at 175 K - it has frequently been the molecule in which various SCO effects were first shown. Despite its poor solubility, FeP2 has been chosen time and time again probably because of its ease of preparation, its highly cooperative spin transition, and because that transition lies within a convenient temperature range (accessible by liquid nitrogen cooling). Only recently has FeP2 been displaced in popularity by other SCO complexes. The attention of the SCO community has shifted to the nanoscale and the fabrication of thin films and nanoparticles. Solution-based film processing techniques are generally not possible with FeP2 because of its low solubility in common solvents. In fact, instead of dissolution, restructuring of FeP2 to the *tris* cation frequently occurs, especially when water is present, even at low levels.<sup>62,63</sup> The author is aware of only one report in which FeP2 was successfully dissolved in DMSO but attempts to do the same were unsuccessful.<sup>21</sup> Additionally, while FeP2 was the first SCO material reported to be successfully vapor deposited, others have reported that decomposition occurs during processing.<sup>25,26</sup> In fact, the challenges associated with the vapor deposition of FeP2 are the subject of this work. In Chapter 4 it is shown that thin films of FeP2 can be obtained by a modified vapor deposition and annealing process.

The first preparations of FeP2 come from two closely timed papers in 1963 from Baker and Bobonich and from Madeja and König.<sup>64,65</sup> These authors would go on to establish much of the fundamental understanding of the SCO phenomenon. Madeja and König recognized that the fields presented by phen ligands should lie near the threshold level where the octahedral splitting energy approached the spin pairing energy and that either the HS or LS state might be possible for *bis*-phen complexes.<sup>65</sup> But, it was Baker and Bobonich who first observed the SCO phenomenon in FeP2.<sup>62</sup> Because of faulty Mössbauer spectroscopy and a flawed interpretation of vibrational

spectra, they proposed a binuclear polymeric structure within which exchange interactions modified the overall magnetic response depending on temperature. The invalidity of those ideas was recognized by them in a subsequent paper.<sup>66</sup> On the other hand, Madeja and König identified a change in spin state between the  $^5T_2$  state at high temperature and the  $^1A_1$  spin state at low temperature as the cause of the unusual magnetic behavior.<sup>67</sup> Confirmation of that proposal was provided by Mössbauer spectroscopy and NMR in another study.<sup>68</sup> As for the origin of the change in spin state, it was natural to suggest that a phase change might occur at the critical temperature.<sup>69</sup> Powder x-ray diffraction (XRD) by Madeja and König showed this was not the case and instead explained that the explanation lay in the relatively close energy spacing of the two electronic configurations.<sup>70</sup>

The relationship of SCO to molecular structure was noticed early on. Madeja and König correctly predicted that a change in the Fe-N bond lengths should result from population of the  $e_g$  orbitals.<sup>70</sup> From the discontinuity in the temperature-dependent heat capacity curve, Sorai and Seki determined  $\Delta H_{HS-LS} = 8.607$  kJ/mol and  $\Delta S = 48.78$  J/mol·K.<sup>4,71</sup> Importantly, they estimated the electronic component of the entropy to be only about 27 % of the total - the remainder coming from molecular and lattice vibrations. Other authors would later use computational methods to show that the vibrational component was dominated by the shift to lower energies of the lowest energy vibrational modes, especially the Fe-N stretching modes.<sup>72,73</sup> The changes in the Fe-N bond lengths predicted by Madeja and König were shown directly by the temperature dependent single-crystal XRD of Gallois et al. in 1990.<sup>74</sup> The crystal in this study was grown via slow diffusion and precipitation in methanol. It possessed the magnetic properties of the so-called "polymorph II" (see below) of FeP2 and was assigned as such by the authors. A crystal structure for "polymorph I"

has yet to be reported. However, the crystal structure of "polymorph I" of  $\text{Fe}(\text{phen})_2(\text{NCSe})_2$  is known and is expected to be isostructural with "polymorph I" of  $\text{FeP}_2$ . In this case, measurement was made possible because of the intense x-ray beam from a synchrotron source.<sup>75</sup> The crystals analyzed were no more than 60  $\mu\text{m}$  long in any one dimension and about 1/50th the size of the crystals used by Gallois et al.

The modern era of  $\text{FeP}_2$  research began around 2008, the year in which the first thin film was produced from the material.<sup>21</sup> The soft lithographic techniques of MIMIC and LCW were used to pattern the material from a solution in DMSO with feature sizes as narrow as 1  $\mu\text{m}$ .  $\text{FeP}_2$  became the first SCO material to be vapor deposited in 2009.<sup>25,26</sup> Since then *ca.* one monolayer thin films have been used to show that SCO molecules directly in contact with an otherwise compatible substrate are often present in a mixture of HS and LS states.<sup>76,27</sup> Molecules in contact with a less reactive substrate (e.g. CuN or HOPG) or located above the first monolayer can be switched individually by application of an electrical bias.<sup>27,29</sup> Finally, within the past year, a calculated density of states has been reported for  $\text{FeP}_2$ .<sup>77</sup> Since the HOMO-LUMO gap is smaller for the HS case and the number of occupied and unoccupied states near the Fermi level is higher for the HS state, conduction through the HS state is expected to be higher than through molecules of the LS state. Additionally, these densities of states in the HS molecule are comprised mainly of  $\beta$  electrons. Therefore, conduction in HS  $\text{FeP}_2$  is also likely spin-dependent. The electrical measurements made on  $\text{FeP}_2$  films in this work are the first step in verifying those theoretical predictions and perhaps in expanding  $\text{FeP}_2$  research further toward the goal of commercial application.

## 2.6 Synthesis of Fe(phen)<sub>2</sub>(NCS)<sub>2</sub>

Within the literature there can be found three primary routes of synthesis for FeP2. The simplest of these is direct precipitation from water or methanol. Both of the other methods begin with the preparation of FeP3 that is also easily prepared from aqueous precipitation. In the first, referred to here as the solvent extraction method, the FeP3 reagent is refluxed in an organic solvent until a phen ligand has been cleaved and FeP2 remains.<sup>78</sup> This synthesis is known to yield the highest quality FeP2 in that the spin transition observed for the material is the most abrupt and complete at both high and low temperatures. The performance of the material has been ascribed to its high degree of crystallinity and is typically referred to as "polymorph I".<sup>79,80</sup> The drawbacks of this method include the use of precarious organic solvents (e.g. pyridine) and the time required (~1 week reflux). For these reasons this method was avoided here. Instead, a third route was employed. In the chosen method FeP3 is pyrolyzed in vacuum to yield FeP2.

The pyrolyzation method is that of Akabori et al.<sup>81</sup> To water, stoichiometric amounts of Fe(NH<sub>4</sub>)<sub>2</sub>(SO<sub>4</sub>)<sub>2</sub>·6H<sub>2</sub>O and phen are added to water along with an excess of NaSCN (or KSCN). As soon as the third component is added, a dark red precipitate forms and is collected by filtration. In the preparations performed here, the solid FeP3 was rinsed with ethanol and water, dried in a lab oven, and used without further recrystallization. Yields were typically 25 to 30 %. Elemental analysis combined with various spectroscopies confirmed the chemical make-up for FeP3. Akabori et al. showed that when heated in a vacuum, *tris* Fe(phen)<sub>3</sub><sup>2+</sup> solids can undergo thermal decomposition, release a phen ligand from each molecule, and form FeP2 through coordination of the anions to the metal center. Here, pyrolyzation was carried out in an evacuated tube furnace (*ca.* 10<sup>-2</sup> Torr) at 190 °C overnight. The mass lost during the pyrolyzation was the magnitude expected

for the loss of 1/3 of the phen ligands in the complex. Figure 2.6 shows the mass lost by FeP3 as a function of temperature as it is heated in air. The identity of the product of pyrolysis was confirmed by elemental analysis and by comparison of many spectroscopic measurements with the literature. Overall yield was limited only by the initial yield of the FeP3 precipitation reaction. The product that results from this synthesis exhibits a cooperative spin transition but with some residual HS component at low temperature. The lower quality FeP2 is often referred to as "polymorph II." It should be noted though that the two forms of FeP2 are not necessarily polymorphs in the traditional sense. Indeed, outside of their magnetic properties, the two materials are nearly indistinguishable by spectroscopic comparison. It has been shown that the primary difference between these materials is the crystalline quality of the powders and the degree to which defects are present.<sup>80</sup>

Synthesis of FeP2 by direct precipitation from solution also produces a material of substandard crystallinity, i.e. "polymorph II." It begs the question as to why the thermal decomposition method was chosen in favor of a seemingly simpler method that produces product of the same quality. In fact, initial attempts at direct, one-pot syntheses of FeP2 were attempted, and were unsuccessful. Instead of FeP2, synthesis by precipitation yielded largely FeP3. If one compares the single-pot, aqueous synthesis of FeP2 given by Schilt and Fritsch to the aqueous precipitation of FeP3 used by Akabori, et al. few differences are found, only the addition of a small amount of weak acid *after the Fe<sup>2+</sup> and phen have been combined* (this point is important later) and an aging step.<sup>82</sup> By the former's admission, the precipitate is impure until the powder has been aged for a sufficient period. Even in following the procedure of Schilt and Fritsch to the letter, the compound produced here was always FeP3, at least in majority. Whatever preparation method was

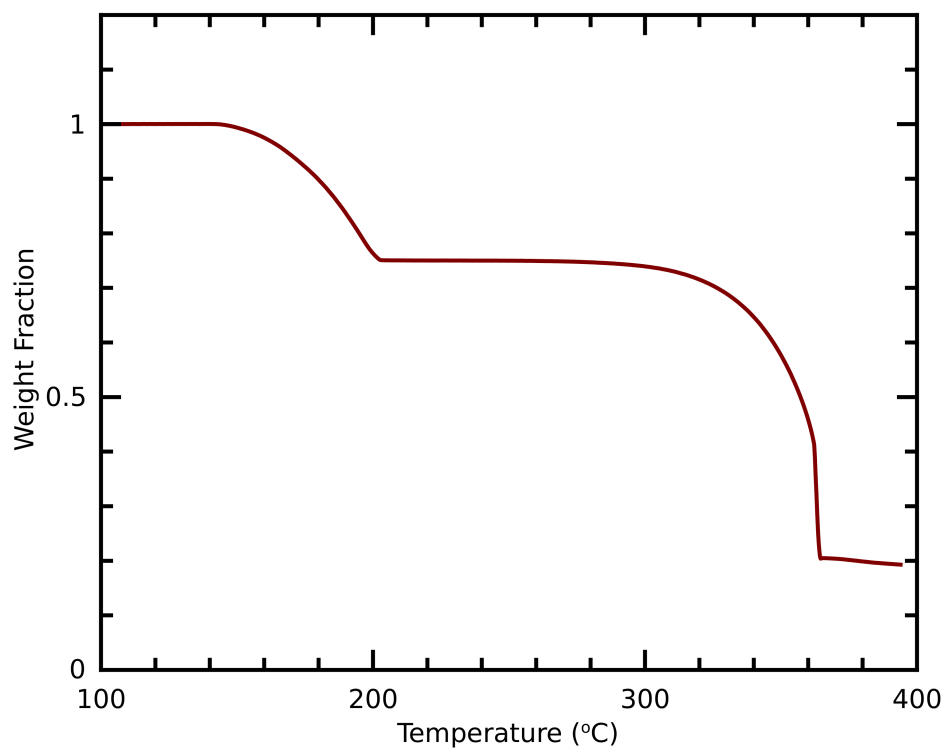


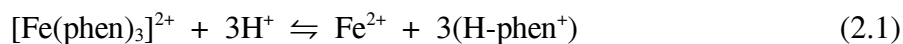
**Figure 2.6.** The result of a TGA experiment in air starting with FeP3. The initial mass loss is equivalent to a single phenanthroline molecule while the second mass loss indicates the simultaneous ejection of the remaining two phen ligands.

used, careful examination of the Raman and FT-IR spectroscopy revealed that the FeP3 precipitate contained traces of FeP2 (spectra in Chapter 3).

Review of the earlier FeP2 literature finds some confusion among those pioneering scientists concerning the products produced during their attempts to synthesize FeP2 by precipitation.<sup>82-87</sup> Often times red complexes (FeP2 is purple) with triplet ground states, and lacking the characteristic  $\nu(\text{N-CS})$  doublet in the vibrational spectra are presented as various hydrates of FeP2. After recognizing that precipitation reactions sometimes produce both FeP2 and FeP3, it seems likely that these authors were suffering from product impurities, probably mixtures of FeP2 and FeP3, or even co-crystals or solid solutions. Many of those authors relied on elemental analysis in order to assign chemical identity, a practice which is unreliable.

Instead of abandoning the aqueous precipitation method completely, small empirical tests were performed on many trials. Two general observations were made: 1) an excess of  $\text{Fe}^{2+}$  improved yield and 2) addition of a small amount of acid to the main reaction vessel *at the beginning of the synthesis* resulted in a single product, purple FeP2, being produced. These two observations are easy to rationalize. The reaction of  $\text{Fe}^{2+}$ , phen, and thiocyanate anion can reasonably be presumed to follow Scheme 2.1. Phenanthroline ligands are sequentially added to the metal until  $[\text{Fe}(\text{phen})_3]^{2+}$  is fully formed (reactions (a), (b1), and (c1)). At that step, and after the formation of the *mono* and *bis* cations, reaction with  $\text{SCN}^-$  can occur yielding one of the dithiocyanato complexes (reactions (b2), (c2), and (d)). Under normal conditions, reactions (a), (b1), and (c1) happen in quick succession and the ferriin cation is formed quickly and quantitatively. The total equilibrium constant of those three reactions together is around  $10^{22}$ .<sup>88</sup> At high starting concentrations of  $\text{Fe}^{2+}$ , phen, and  $\text{SCN}^-$ , the product yield will exceed the solubility

and FeP3 will precipitate in reaction (d). Now, if acid is present, the ferriin cation might undergo dissociation following



The equilibrium constant for Equation 2.1 can be written as:

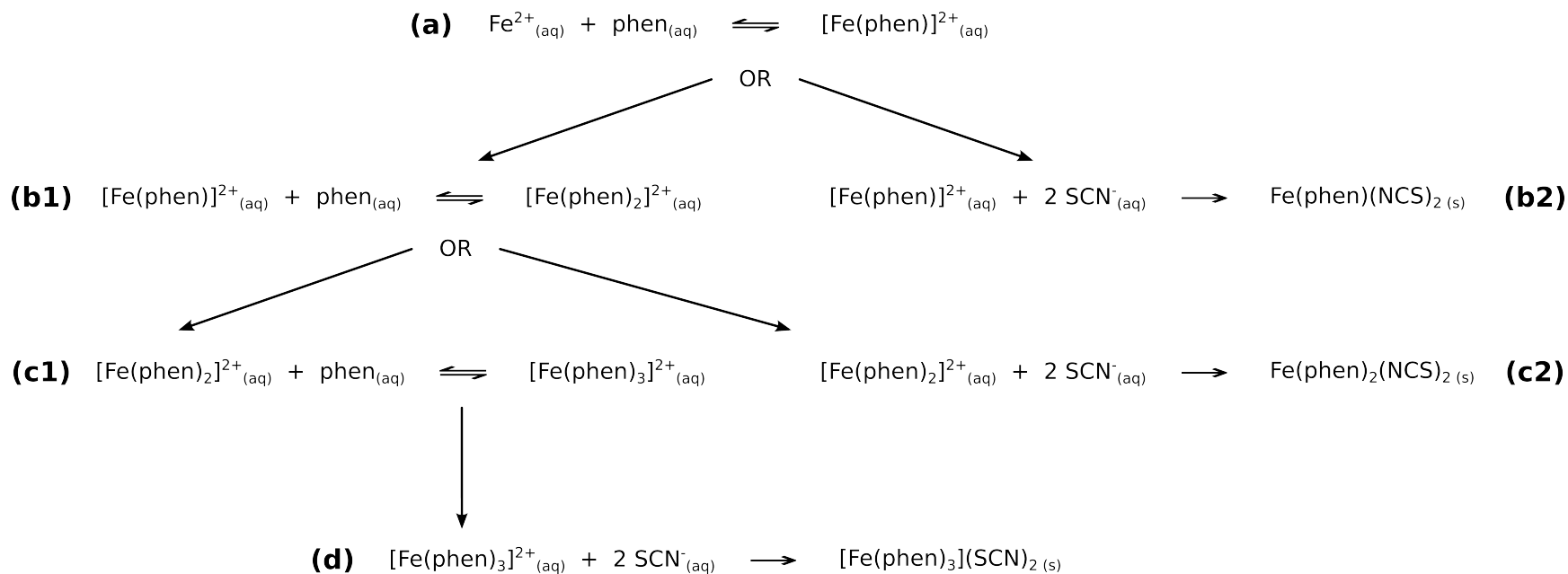
$$K_{\text{eq}} = [\text{Fe}^{2+}] [\text{H-phen}^+]^3 / [\text{Fe}(\text{phen})_3^{2+}] [\text{H}^+]^3 \quad (2.2)$$

The dependence of the ferriin cation concentration on the acid concentration is then:

$$[\text{Fe}(\text{phen})_3^{2+}] \propto [\text{H}^+]^{-3} \quad (2.3)$$

Addition of acid at the beginning of the synthesis will hinder the formation of the ferriin cation severely. The instantaneous concentration of ferriin is unlikely to exceed the solubility and little to no precipitation of FeP3 is expected. On the other hand, the kinetically slower reaction of the *bis* cation with the  $\text{SCN}^-$  (reaction c2) now has an opportunity to proceed. As this precipitation occurs, product is removed from solution, pulling the equilibrium toward the formation of more FeP2 until all reagents are consumed. Finally, beginning with an excess of  $\text{Fe}^{2+}$  will, through Le Chatelier's principle, improve the yields of both FeP2 and FeP3. The end result is a mostly pure FeP2 product in high yield. Putting this together, a new synthesis procedure was designed:

1. To 100 mL  $\text{H}_2\text{O}$ , 1 mL of 1.8 M  $\text{H}_2\text{SO}_4$  is added.
2.  $\text{Fe}(\text{NH}_4)_2(\text{SO}_4)_2 \cdot 6\text{H}_2\text{O}$ , NaSCN, and  $\text{phen} \cdot \text{H}_2\text{O}$  are measured so that the ratio of  $\text{Fe}^{2+}:\text{phen}:\text{SCN}^-$  is 2:1:5.
3. The  $\text{phen} \cdot \text{H}_2\text{O}$  is dissolved in the acidified water by applying gentle heating. The solution is allowed to cool to room temperature.
4. The  $\text{Fe}(\text{NH}_4)_2(\text{SO}_4)_2 \cdot 6\text{H}_2\text{O}$  and NaSCN are dissolved in 15 mL  $\text{H}_2\text{O}$ .



**Scheme 2.1.** Sequential reaction with phen yields the *mono* (a), *bis* (b1), and *tris* (c1) cations. Reaction with thiocyanate after each step potentially yields the *mono* (b2), *bis* (c2), and *tris* (d) dithiocyanato complexes.

5. The two solutions are combined slowly.
6. The purple precipitate that forms is collected by gravity filtration, rinsed with water, and placed in the laboratory oven at 80 to 100 °C for at least 1 hr.

The FeP2 product created in > 95% yield by this procedure is relatively pure. In this work, the FeP2 material used for deposition of thin films was created by thermal decomposition of FeP3 following Akabori et al., or by the method listed above.<sup>81</sup>

## **2.7 Summary**

The two storied complexes FeP3 and FeP2 are closely related, so much so that the synthesis of one is tied to the synthesis of the other. In the solvent extraction method and the thermal decomposition method, FeP2 is produced from FeP3 by removal of a single phen ligand and coordination of the thiocyanate ligands to the metal center. During a precipitation synthesis of either, mixtures of these two complexes can result. A modified precipitation synthesis procedure has been developed for FeP2 which increases the yield to a maximum and requires only a single step.

## CHAPTER 3

### PREPARATION AND CHARACTERIZATION OF $[\text{Fe}(\text{phen})_3](\text{SCN})_2$ FILMS

#### 3.1 Physical Vapor Deposition of Films from $\text{Fe}(\text{phen})_2(\text{NCS})_2$

In following the report from Shi et al., it was attempted to grow FeP2 thin films by physical vapor deposition directly from FeP2 powder.<sup>26</sup> Deposition was carried out within the vacuum deposition chamber described in Chapter 1. The conditions of this system are similar to the conditions reported by those authors. FeP2 powder was loaded into a cleaned deposition boat and heated resistively. The temperature of the powder in the boat was not controlled accurately. Rather, the power to the boat was manually adjusted in attempting to maintain a desired deposition rate, as measured by the QCM. However, a consistent rate was nearly impossible to maintain due to the erratic vaporization of the material.

The deposition boat can be monitored during the deposition by looking through the chamber window. At the conditions employed here, deposition begins when the FeP2 powder liquefies suddenly in random spots. The liquid that forms evaporates quickly and produces a rapid burst of film growth where the deposition rate correlates with the size of patch of material that has vaporized. These bursts of film growth usually occur soon after each power increase but cease when that power level is maintained such that increasingly higher power levels (boat temperatures) are required to deposit all of the material from the boat. In addition, the powder is observed to turn from its purple color to a light orange around the edges of piles of powder.

QCM parameters were not calibrated but a z-ratio of 1.00 and a density of  $1.50 \text{ g/cm}^3$  are found to yield films of roughly two to three times the indicated thickness. Actual film thicknesses were determined directly ex-situ by profilometry. To this end, masking the substrates with a thin ( $40 \text{ }\mu\text{m}$  diameter) wire produces trenches with sharp profiles well-suited for profilometry.

### **3.2 Topography and Air Sensitivity**

While difficult to control, the erratic deposition process described yields high quality films of an intense red color. AFM reveals that the films are smooth at the nanoscale and the RMS roughness is typically around 1 nm (Figure 3.1). While initially smooth, the films produced as described above suffer severe changes in morphology upon exposure to air. In most cases, these changes manifest as nucleation and growth of rough circular domains that increase in size until the entire sample surface is no longer smooth (Figure 3.2). In the case of thicker films, dewetting of the film from the sample surface sometimes occurs leaving isolated blobs that are liquiform in appearance. Micrographs of dewetted films are presented in Figure 3.3. The rate of change is slower for samples that are allowed to cool for several hours before removal from the chamber and even for films in the process of rapid transformation, removal to a low moisture, low oxygen nitrogen atmosphere (i.e. a glove box) halts any changes. Likewise, while under vacuum films remain smooth.

Observation of air sensitive films deposited from FeP2 is not unprecedented. Shi et al. reported that films produced in the same manner were "smooth with no visible grains" with RMS roughnesses less than 1 nm.<sup>26</sup> But, the authors noted that "the film morphology is sensitive to the environment and becomes coarse when exposed to air." The exact origin of these morphological

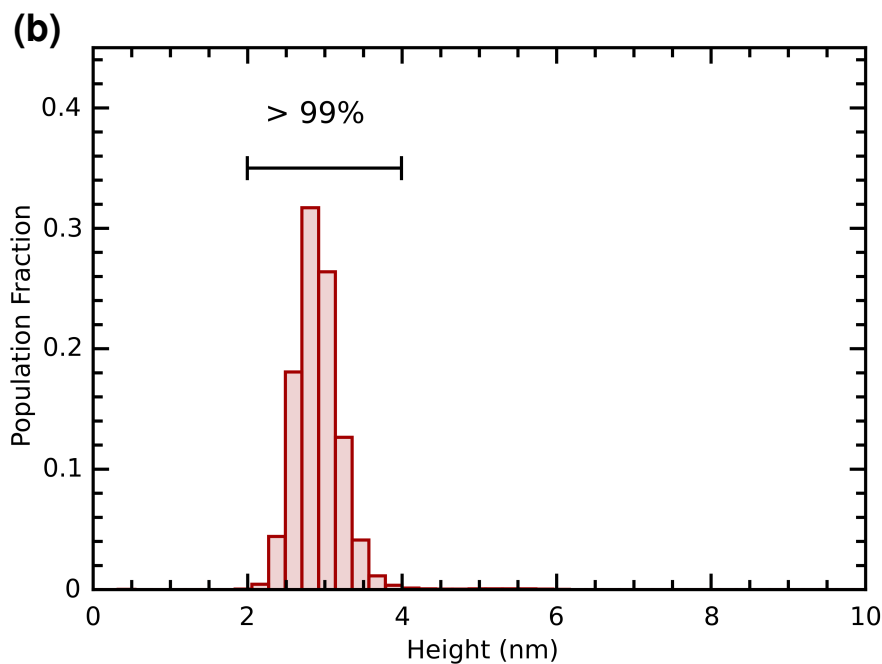
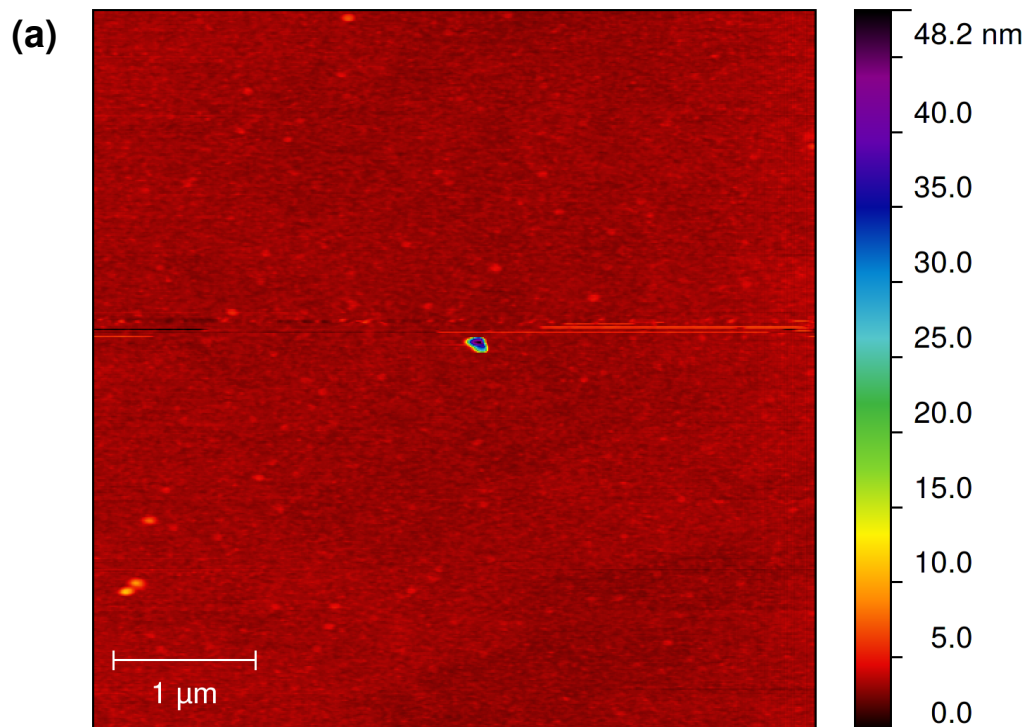


**Figure 3.1.** AFM topography scan of a  $\sim 20$  nm red film deposited from FeP2 onto a Si substrate (a) and the corresponding height distribution of the pixels in the image (b). Greater than 99% of pixels lie within 2 nm (height) of each other. The film was scanned within 1 hour of removal from vacuum before it had roughened from exposure to air.

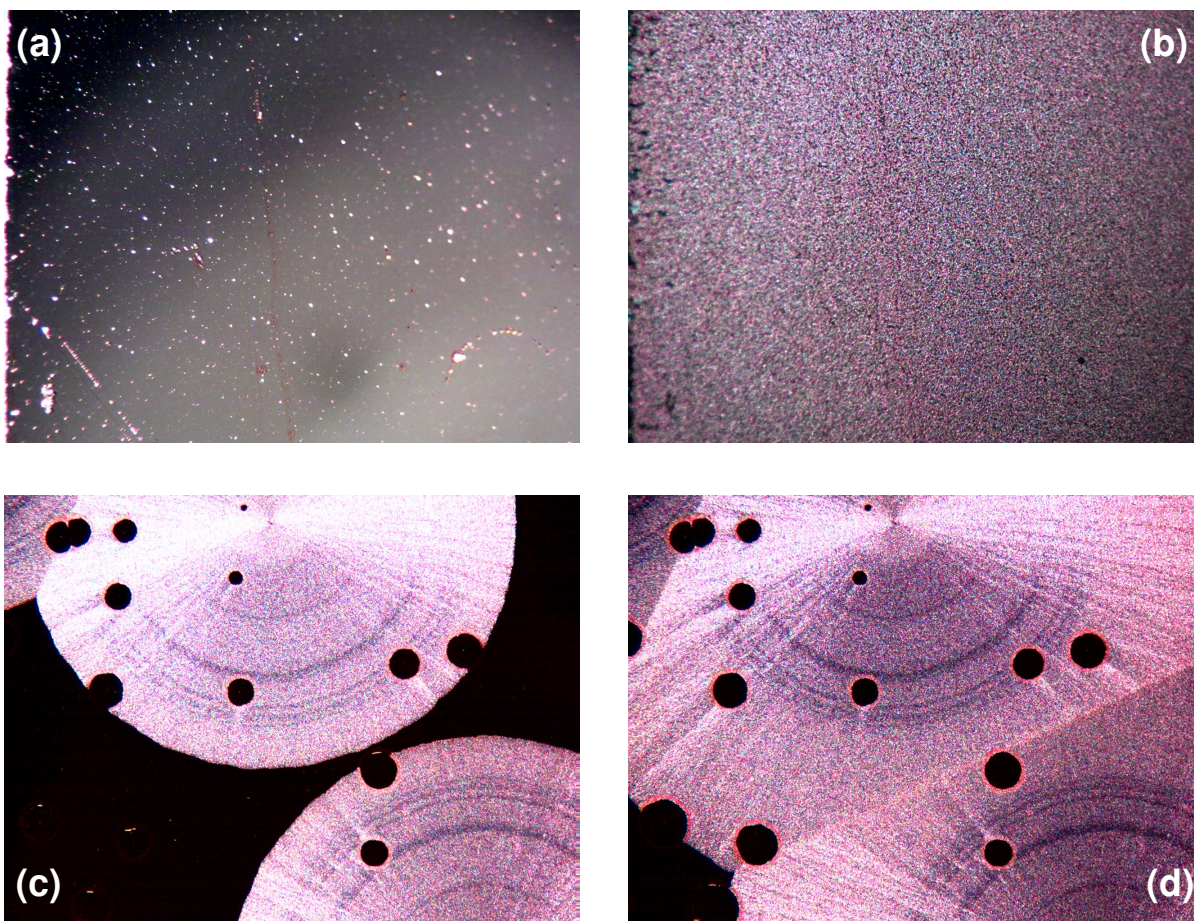


**Figure 3.2.** Optical micrographs (10x) of a red film deposited from FeP2 onto gold (*top*) taken shortly after removal from the deposition chamber (*a*) and after being exposed to air for 140 min (*b*). A time-lapse video of this sample is available as Supplemental File S1. *Bottom* frames show optical micrographs (10x) from a second sample of a red film on a Si substrate taken shortly after removal from the deposition chamber (*c*) and after only 3 min exposure to air. The small black circles are areas where the film has dewetted from the Si surface.

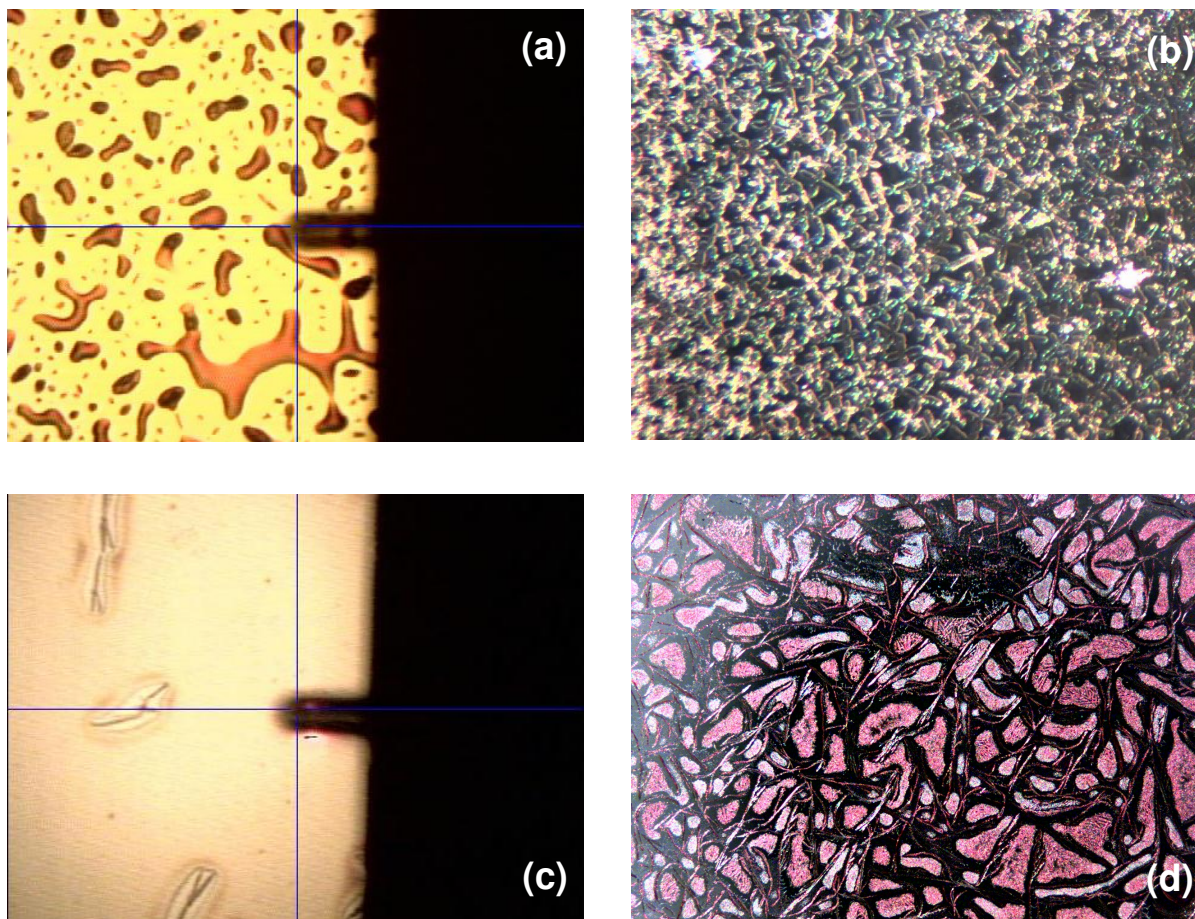


**Figure 3.3.** Examples of morphological changes in films deposited from FeP2 that occur on exposure to air. Top panels show examples of dewetting (*a*) and crystallization (*b*) in films deposited onto Si and Si/Al, respectively. Bottom panels show both dewetting and crystallization occurring simultaneously in a single film on a Si/Al substrate after ~ 30 min of air exposure (*c*) and again after 24 hrs (*d*). The images in panels *a* and *b* were captured through the camera of the AFM. A time-lapse movie of the changes occurring in panel *c* is available as Supplemental File S2.

changes was not intensely investigated here, but it is hypothesized that the instigator of the air sensitivity is water vapor. Oxygen gas is another possible suspect. Any reaction with oxygen is almost certainly to be chemical in nature but no chemical difference between the smooth and roughened films is seen in the spectroscopy. Hence, water vapor is the more likely candidate.

The problem of air sensitivity of films deposited from FeP2 is ameliorated by a post-deposition, in situ annealing step. The development and details of this process can be found in Chapter 4. From the observations presented therein, it is hypothesized that the air sensitivity of the films is related to the presence of a phen impurity in the films. Upon exposure to water vapor, highly hygroscopic phen might undergo crystallization. The post-annealing process is believed to improve air-durability by expunging any phen impurity. Encapsulation of films may also provide adequate protection.<sup>26</sup> Attempts to protect films with top layers of LiF only marginally increased survival time.

Powder x-ray diffraction of a freshly prepared, smooth, post-annealed film on Si exhibits no discernible Bragg reflections but a roughened film shows the spectrum in Figure 3.4. The reflections do not appear to match that expected for phen.<sup>89</sup> Of course, the films cannot be pure phen (owing, at least, to the color) and a mixture of species might produce a crystal structure unseen in previous studies. The major peaks in the spectrum occur below  $15^\circ 2\theta$  which means that the d-spacing between the observed Miller planes is large. The crystalline material is therefore molecular. That relatively few planes are observed might indicate textured crystalline domains. Further investigation into the exact nature of the air sensitive films was not undertaken once the post-annealing process was discovered to remove the sensitivity. It is believed that post-annealed films are amorphous and of a single component.

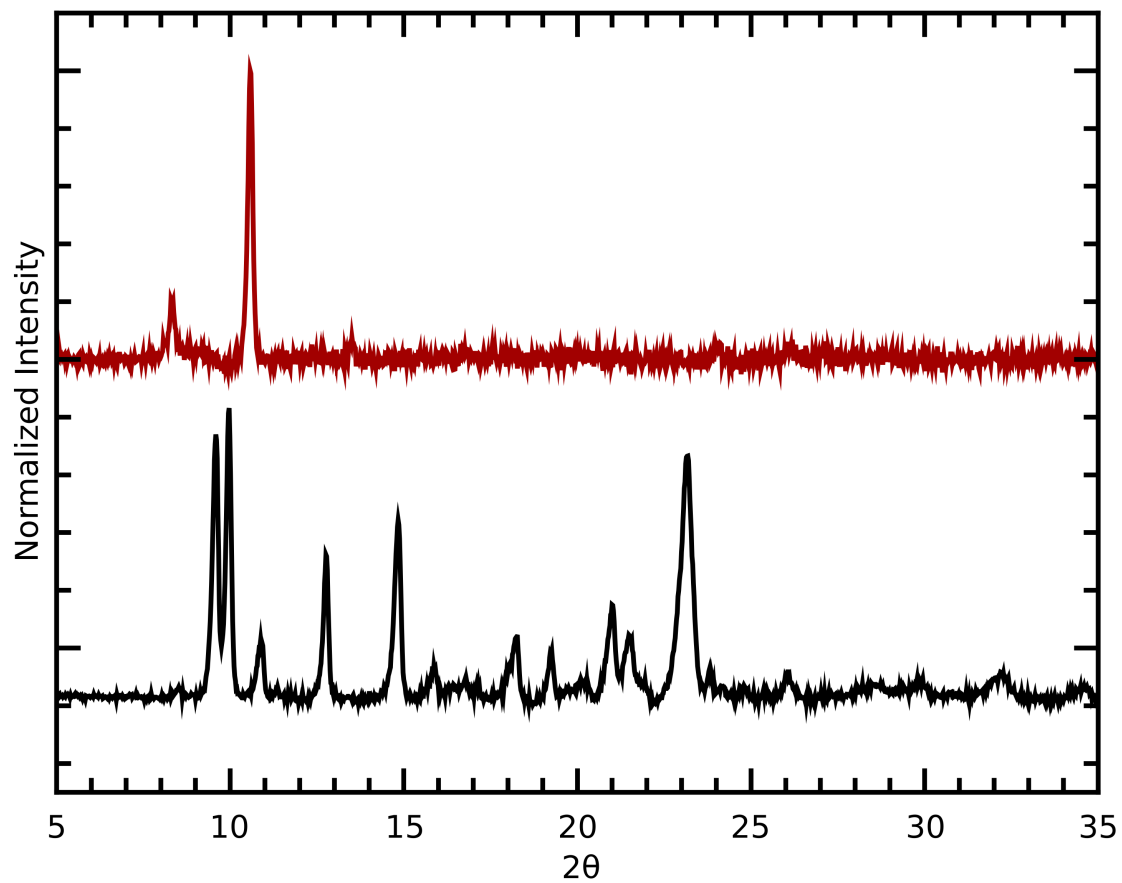


**Figure 3.4.** X-ray diffraction ( $\text{Cu K}\alpha$ ) spectrum of a red film deposited from FeP2 onto a glass substrate (top) compared to that of FeP3 powder (bottom). The film spectrum was collected after the film had roughened due to air exposure.

### 3.3 Ultraviolet-Visible Spectroscopy

The UV-Vis absorption spectra of the films deposited from FeP2 were measured by depositing thick films onto a glass substrate and measuring in the normal transmission mode. Figure 3.5 compares a resulting spectrum to the spectrum from the  $\text{Fe}(\text{phen})_3^{2+}$  cation collected by dissolving FeP3 powder in ethanol. For the films on glass, absorption below 350 nm is from the glass substrate. In the spectrum of the *tris* cation presented, the extremely strong absorbance below 350 nm due to the phen ligands is omitted for clarity.<sup>90</sup>

The strong band at 510 nm in the spectrum of the ferrioxalate cation gives rise to its intense red color and forms the basis of a common spectrophotometric test for iron.<sup>91-94</sup> The origin of this band is a metal-to-ligand-charge-transfer (MLCT) of an electron from an Fe  $d^6$  orbital to a  $\pi^*$  orbital of a phen ligand.<sup>55,56</sup> The higher energy shoulders at 443 and 481 nm have been attributed to vibronic coupling with the  $1505\text{ cm}^{-1}$  vibrational mode based on their near constant energy spacing and with the  $1635\text{ cm}^{-1}$  mode based on the results of a resonant Raman spectroscopy experiment.<sup>55,95</sup> However, Ito et al. have given evidence that a second charge transfer mode may also contribute to the low energy peak intensity.<sup>90</sup>

Whatever the origin of the complex energy structure of the ferrioxalate cation in the visible region, that structure is largely preserved in the films deposited from FeP2. The wavelength of maximum absorption is shifted 13 nm to 523 nm. The two shoulders each experience similar shifts to 453 and 492 nm. The energy difference in wavenumbers between the two shoulders is 1783 and  $1750\text{ cm}^{-1}$  in the ferrioxalate cation and the film, respectively. The energy difference in wavenumbers between the lower energy shoulder and the main absorption band is 1182 and  $1205\text{ cm}^{-1}$  for the

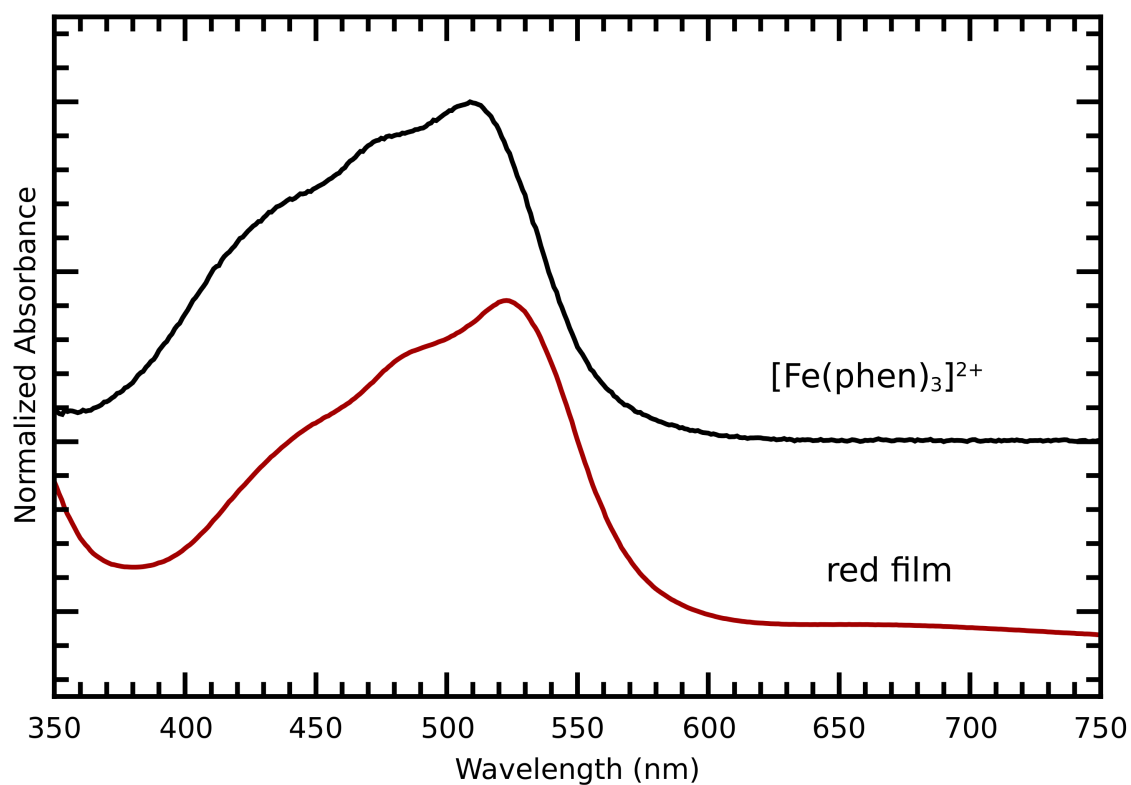


**Figure 3.5.** UV-Vis spectra of [Fe(phen)<sub>3</sub>]<sup>2+</sup> ions in ethanol (top) and of a red film deposited from FeP2 onto glass (bottom). Absorbance maxima occur at  $\lambda_{\text{MAX}} = 510$  and 523 nm, respectively.

cation and the film, respectively. Given the uncertainty in determining the positions of the shoulders, energy spacings can be considered equivalent between the cation and the film. Thus, the electronic structure of the film matches with that of the ferriin cation but with a minor shift of about 13 nm ( $\sim 500 \text{ cm}^{-1}$ ) to lower energy.

A small shift in peak positions should not be surprising when comparing the solid state of a species with a solvated state where solvent effects are likely to perturb the electron orbitals through intermolecular interactions. If the high energy shoulders are in fact a result of electronic-vibronic coupling, the retention of these shoulders without significant modification suggests that the vibrational modes of the ferriin cation and film are also very similar, at least. Therefore, the transmission UV-Vis spectra strongly suggest that the species within the films deposited from FeP2 contain the ferriin cation. If this is true, the most likely anion to be produced from decomposition of FeP2 during deposition is the thiocyanate anion and films are likely FeP3. More evidence to this conclusion is provided in this chapter.

Shi et al. also measured the UV-Vis transmission spectra of films deposited onto glass from FeP2 and at different thicknesses (530, 230, 48, 11, and 7 nm).<sup>26</sup> Except for the expected change in intensity, those spectra are identical at all measured thicknesses and perfectly consistent with the spectrum of the thin film deposited from FeP2 in this work. If one plots the absorbance of the films (at  $\lambda_{\text{MAX}} = 523 \text{ nm}$ ) in that work as a function of thickness one finds a slope of roughly  $2.2 \times 10^4 \text{ cm}^{-1}$  (Figure 3.6). The slope represents the product of the extinction coefficient and concentration, i.e. the density, of the absorbing species. For FeP3, this product is expected to be about  $2.2 \times 10^4 \text{ cm}^{-1}$  given that the density of IP3 is  $1.43 \text{ g/cm}^3$  (or 2.01 M) and the extinction coefficient in solution is

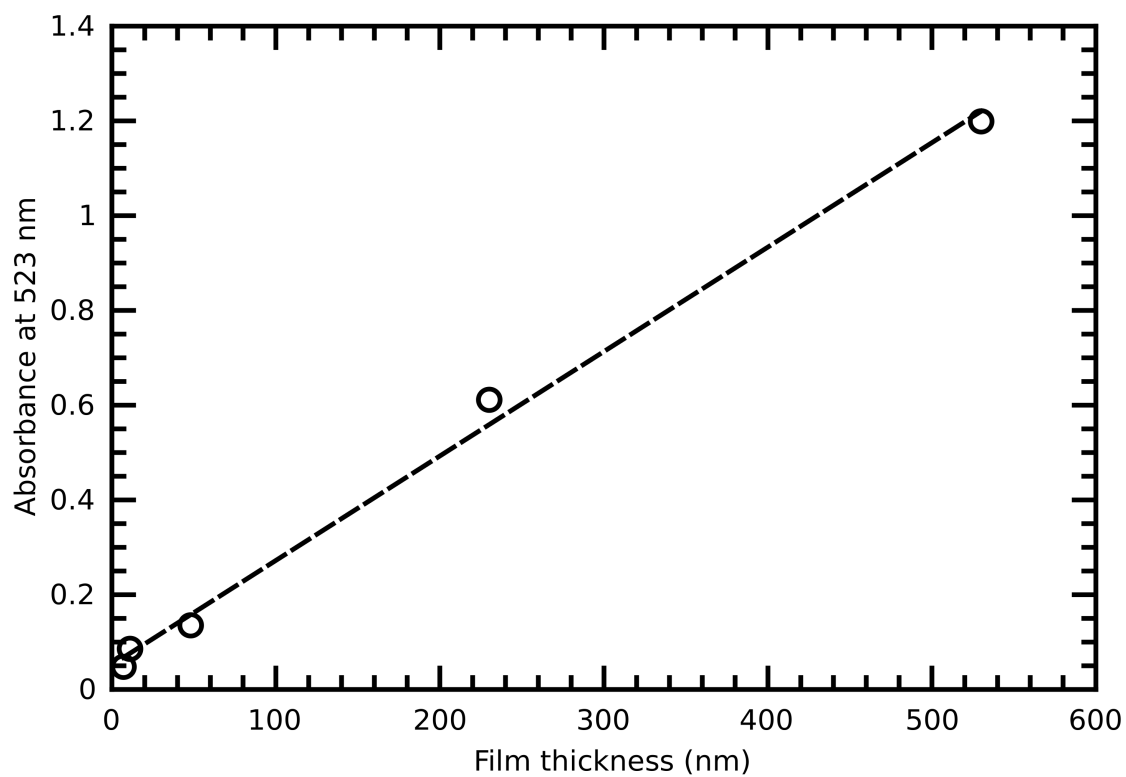


**Figure 3.6.** Absorbance vs. film thickness for films deposited on glass from FeP2. Data points were extracted from Figure 3 in Ref. 26 using image analysis software. The dashed line represents a linear fit to the data (slope =  $2.2 \times 10^4 \text{ cm}^{-1}$ , y-intercept =  $5.2 \times 10^{-2}$ ).

about  $11,000 \text{ cm}^{-1} \text{ M}^{-1}$ .<sup>55</sup> This analysis suggests that the films measured by Shi et al. and that measured in this work can reasonably be identified as FeP3.

### 3.4 Vibrational Spectroscopy

The FT-IR spectra of FeP3 powder and of a red film deposited from FeP2 onto a Si wafer are compared in Figure 3.7. The powder spectrum was collected by ATR FT-IR while the film spectrum was collected in transmission mode through the Si substrate which is largely transparent to infrared radiation in the region shown. The absorbance from the native oxide of the Si wafer near  $1100 \text{ cm}^{-1}$  has been removed from the film spectrum. A list of peak positions for the FeP3 powder and another red film on KBr are given in Table 3.1.

For FeP3, the region from  $1800$  to  $900 \text{ cm}^{-1}$  is comprised entirely of ligand modes. Above and below this region, the thiocyanate ligands are expected to exhibit three modes: the N-CS stretch, the NC-S stretch, and a bending mode, the last of which occurs outside of the mid-IR region shown.<sup>96</sup> The N-CS stretch is the easiest to identify and is observed at  $2048 \text{ cm}^{-1}$  which is expected for uncoordinated  $\text{SCN}^-$ . For comparison, the N-CS stretch is found at  $2049 \text{ cm}^{-1}$  in the ionic compounds KSCN and  $\text{NH}_4\text{SCN}$ .<sup>97,98</sup> In the synthesized FeP3 powder, an energy shoulder appears to also be present suggesting contamination by thiocyanate in another bonding environment. The Raman spectrum of the FeP3 powder shown in Figures 3.8 and 3.9 and discussed below suggests that FeP2 contamination is present in the precipitated and unpurified material. The FeP2 molecule exhibits two N-CS modes at  $2072$  and  $2060 \text{ cm}^{-1}$  and its presence as an impurity in the FeP3 powder could account for the high energy shoulder of the  $2048 \text{ cm}^{-1}$  peak. The red film shows only a single peak in the N-CS stretching region at  $2050 \text{ cm}^{-1}$ . This energy is

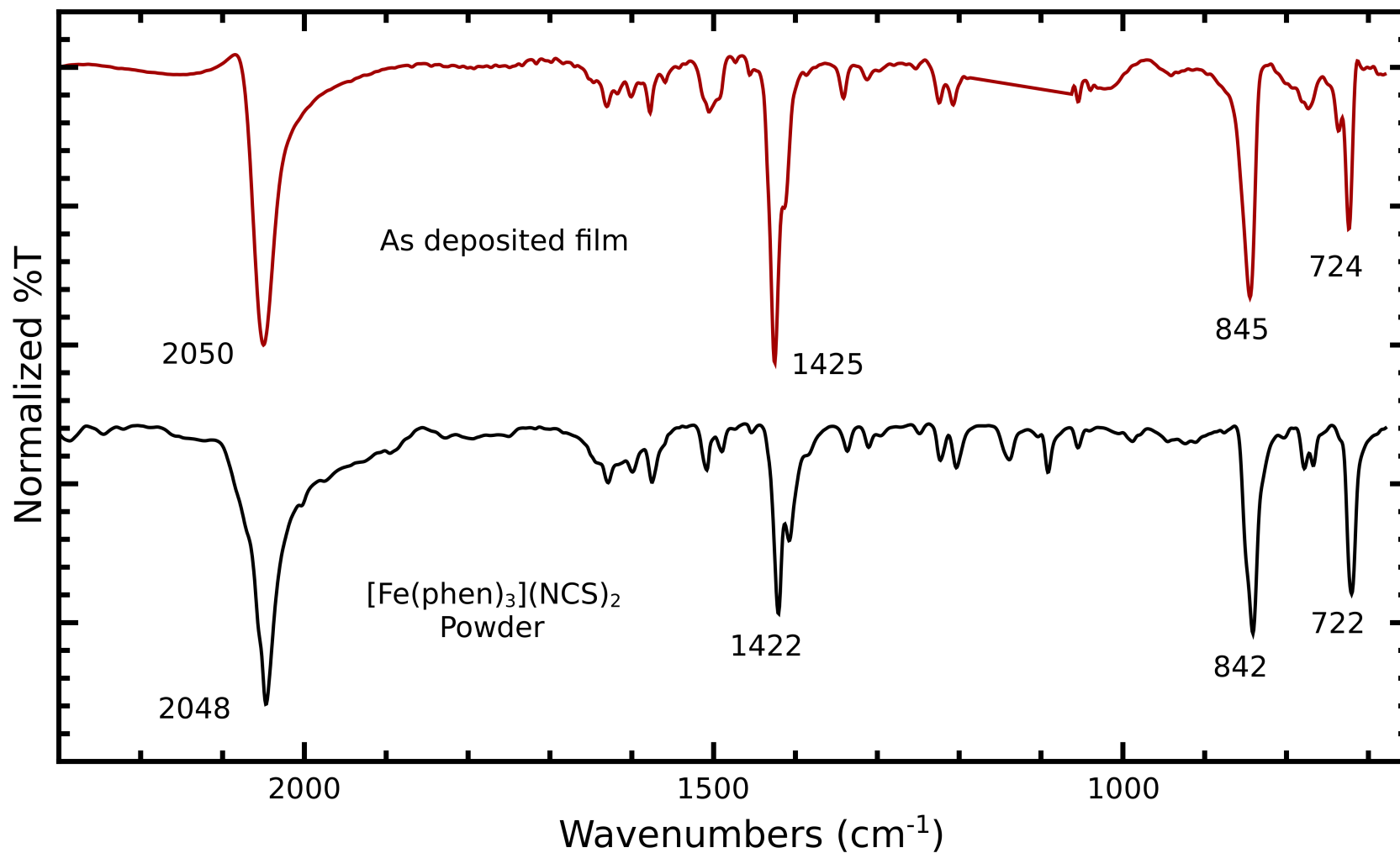


**Figure 3.7.** FT-IR spectra of FeP3 powder (bottom) compared with a red film deposited from FeP2 onto a Si substrate (top) in the region from 680 to 2300  $\text{cm}^{-1}$ . The  $\text{SiO}_2$  absorption of the substrate in the region near 1100 to 1200  $\text{cm}^{-1}$  has been removed from the top trace.

**Table 3.1.** Peak positions and peak assignments from the vibrational spectroscopy of FeP3 powder compared to red films<sup>a</sup> deposited from FeP2.

Fe[(phen) <sub>3</sub> ](NCS) <sub>2</sub>		red film		Assignment	Fe[(phen) <sub>3</sub> ](NCS) <sub>2</sub>		red film		Assignment
IR	Raman	IR	Raman		IR	Raman	IR	Raman	
		2103 w			990 w				
	2068 w				982 w				
2048 s	2053 w	2053 s		v(N-CS)	946 w				
2004 sh					925 w				
1976 sh					913 w	912 m		913 w	
1631 m		1629 w			877 w	876 w		878 w	
		1621 sh					865 w		
1601 m	1599 m	1602 w	1603 m	v(C-C), v(C-N)	842 s		843 s		carbocyclic ring deformation
1577 m	1575 s	1577 w	1581 s		804 w		809 w		
		1561 w					801 w		
1510 m	1510 s	1513 m	1515 s		779 m		773 m		
1492 m		1494 w			768 m				
1456 w	1451 s	1453 w	1456 s		736 w	737 s	734 w	738 s	
			1434 w		722 s	723 m	724 s	724 m	heterocyclic ring deformation
1422 s	1428 w	1424 s				645 w		645 w	
1408 s	1416 m	1413 sh						619 w	
1388 sh								583 w	
1338 m	1337 w	1342 m	1345 w		560 m			561 m	
1311 m		1312 w			495 m			495 w	
1297 w	1295 s		1301 m		464 w				
1250 w	1249 w	1252 w	1254 w		435 w			436 w	
1224 m	1224 w	1223 w			419 w				
1204 m	1206 s	1207 w	1212 m		407 w				
1141 m	1144 m	1142 m	1144 w		368 w		369 w		v(Fe-N(phen))
1105 w	1105 w	1102 w	1107 w		314 w		314 w		
1092 m	1092 w	1094 w			296 w		296 w		
1056 m	1055 m	1056 w	1057 w		281 w				
1042 w		1040 w			177 w				
1007 w					154 w		153 m		

<sup>a</sup> IR comes from a film on KBr, Raman from a film on glass.

compatible with uncoordinated  $\text{NCS}^-$ , as seen in the FeP3, but is also compatible with N-coordinated thiocyanate (isothiocyanate). However, the energy observed largely excludes S-coordinated thiocyanate and bridging thiocyanate modes.<sup>96</sup> McKenzie has observed that octahedral  $\text{Fe}^{2+}$  complexes of the type  $\text{Fe}(\text{phen})_2\text{X}_2$  are almost exclusively found with a *cis* arrangement of the ligands.<sup>99</sup> In this configuration, a doublet is expected for the N-CS asymmetric and symmetric stretches, yet only a single mode is observed in the spectrum of the films deposited from FeP2. Of course, the doublet may simply be unresolved, but since these modes are clearly defined in the case of FeP2 powder, it is safe to conclude that the deposited films cannot be identified as such.

The NC-S stretch occurs near  $750$  and  $748\text{ cm}^{-1}$  for KSCN and  $\text{NH}_4\text{SCN}$ .<sup>97,98</sup> The FeP3 powder shows small peaks at  $779$  and  $768\text{ cm}^{-1}$  that might be assigned to this mode. Similarly, the red film has peaks at  $781$  and  $774\text{ cm}^{-1}$ . In the same region is a shoulder at  $736\text{ cm}^{-1}$  which is much more pronounced in the film than in the powder. The phen ligands also show small peaks in this region which complicates the issue further.<sup>100</sup> Unfortunately, a definite assignment of the NC-S stretch cannot be made without a more sophisticated experiment, such as isotopic labeling.

The phen ligands are responsible for the majority of the peaks in the middle of the FeP3 spectrum and many arise from C-C and C-N stretching modes. Upon coordination of a phen molecule to a metal center, these modes may not show significant changes and so cannot be used to identify free or coordinated phen in the film spectrum.<sup>101,100</sup> Within this region, the most significant difference between the spectrum of the FeP3 powder and that of the red film is the larger relative intensity of the mode near  $1425\text{ cm}^{-1}$  in the case of the film. The mode in question is almost certainly centered on the phen molecule but the origin of the increased intensity is unknown.

Two strong phen peaks are also found in the low energy portion of the FeP3 powder spectrum at 842 and 722  $\text{cm}^{-1}$  which result from the carbocyclic and heterocyclic ring deformations of the phen ligands, respectively.<sup>101</sup> Presumably, the peaks at 845 and 724  $\text{cm}^{-1}$  in the red film spectrum are of the same origin. It must be mentioned that in the spectrum of free phen, these two peaks are each split into two doublets that occur at approximately 853/837 and 738/730  $\text{cm}^{-1}$ .<sup>100</sup> Assignment of the small shoulder at 736  $\text{cm}^{-1}$  in the red film spectrum, mentioned previously, to one half of the 738/730  $\text{cm}^{-1}$  doublet of free phen is tempting. However, it would be expected then to see the second peak of the doublet near 730  $\text{cm}^{-1}$ . Instead of a peak, a trough between peaks is found at this location. Thus it is doubtful that the shoulder at 736  $\text{cm}^{-1}$  in the red film spectrum results from the split heterocyclic ring deformation modes of free phen and the presence of free phen in the film cannot be confirmed in this way.

Figures 3.8 and 3.9 compare the Raman spectrum of the FeP3 powder to that of the red film deposited directly from IP2 onto a Si substrate. In the case of the FeP3 powder, small peaks are present that are assigned to FeP2 present as an impurity. These are bracketed with parentheses in the figures. These assignments are based on the spectra collected of FeP2 powder and films (see Chapter 4) and show that the aqueous precipitation synthesis of FeP3 results in an impure product. Recrystallization from water would likely remove the impurity as well as any co-precipitated, uncoordinated phen. Since this FeP3 powder was used here as a precursor to FeP2 and in that process annealed in a tube furnace (where any phen should evaporate) it was thought unnecessary to recrystallize the FeP3 product.

The Raman spectrum of the FeP3 powder compares extremely well with those of the ferroun ion in solution and of  $[\text{Fe}(\text{phen})_3]\text{Cl}_2$ .<sup>95,102</sup> Comparison with the spectrum of free phen

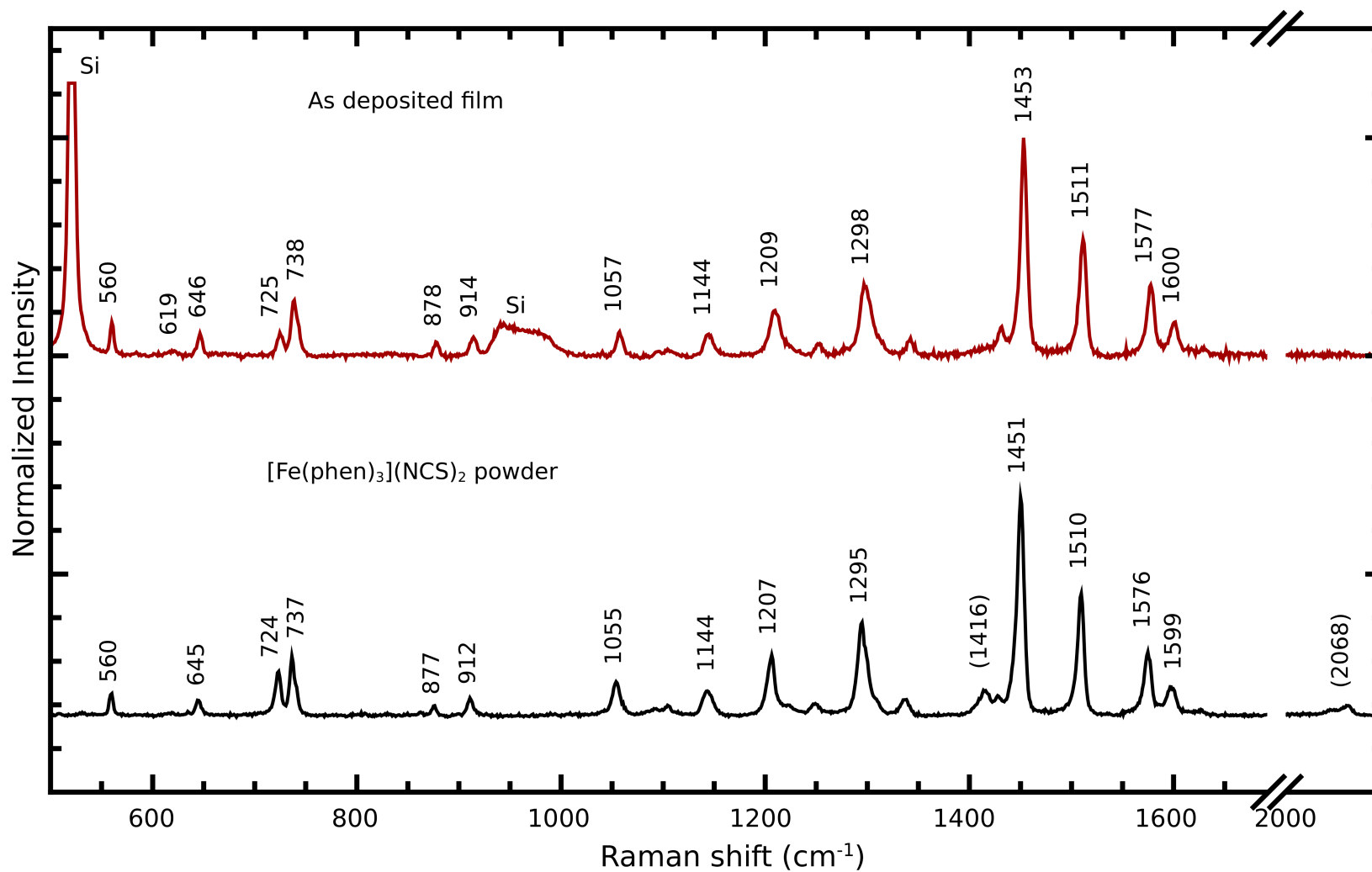


**Figure 3.8.** Raman spectrum of FeP<sub>3</sub> powder (bottom) compared to a red film deposited from FeP<sub>2</sub> onto a Si substrate (top) in the region from 500 to 2100 cm<sup>-1</sup>. Peaks in parentheses denote probable contamination from FeP<sub>2</sub> in the FeP<sub>3</sub> powder.

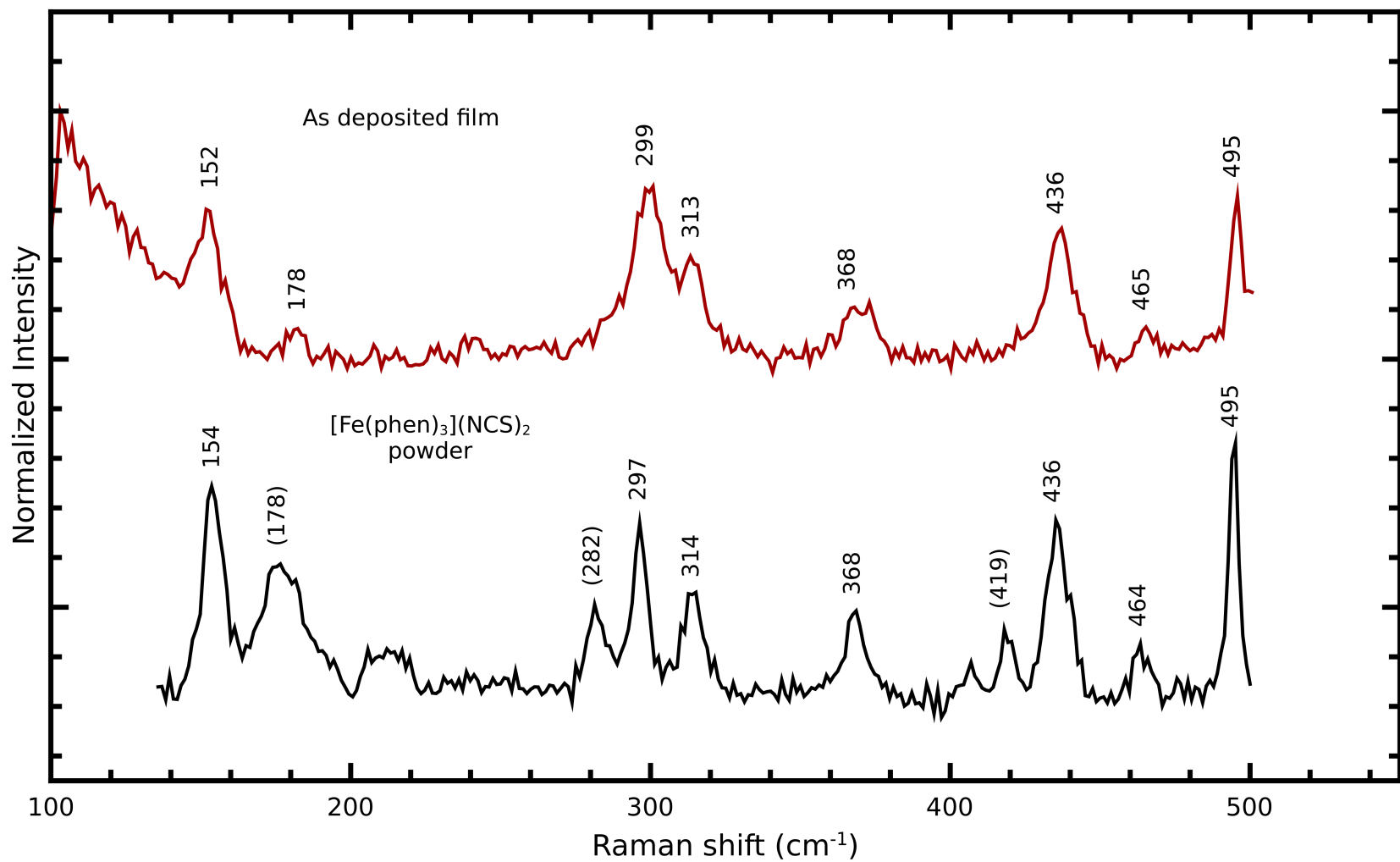


**Figure 3.9.** Raman spectrum of FeP3 powder (bottom) compared to a red film deposited from FeP2 onto a Si substrate (top) in the region from 150 to 500  $\text{cm}^{-1}$ . Peaks in parentheses denote probable contamination from FeP2 in the FeP3 powder.

shows that all but a few peaks originate from the modes of this ligand.<sup>102</sup> However, the metal-ligand stretches which are of more diagnostic value are expected to be found in the low energy region of the spectrum (Figure 3.9).

Through <sup>57</sup>Fe isotopic labeling, Hutchinson et al. found that Fe-N stretches in the far-IR spectra of Fe(bipy)<sub>3</sub><sup>2+</sup> (bipy = 2,2'-bipyridine) and Fe(phen)<sub>3</sub><sup>2+</sup> ions in solution (both diamagnetic ions) occur in the range from 360 to 390 cm<sup>-1</sup>.<sup>103</sup> In the spectrum of Fe(phen)<sub>3</sub><sup>2+</sup>, these authors assigned a set of peaks at 359 (m) and 375 cm<sup>-1</sup> (w) to the Fe-N(phen) stretch. In another experiment, Hofer assigned the Fe-N(phen) stretch to a peak at 366 cm<sup>-1</sup> in the Raman spectrum of the LS (diamagnetic) form of FeP2, based on <sup>15</sup>N isotopic labeling.<sup>104</sup> For the FeP3 powder measured here, only a single peak at 368 cm<sup>-1</sup> is detected.

Considering now the spectrum of the red film deposited from FeP2, with the exception of the few substrate peaks, the compatibility of this spectrum with that of the FeP3 powder is unmistakable. The mode at 368 cm<sup>-1</sup> can be assigned to the Fe-N(phen) stretch and is consistent with such a complex in a diamagnetic spin state, as demonstrated by the examples given above. In a paramagnetic Fe-N(phen) complex the Fe-N bond lengths are longer and the Fe-N(phen) stretch should be found in the region from 200 to 300 cm<sup>-1</sup>. This region is blank for these films.

Being identified as FeP3, these films provide a better spectroscopic reference than even the as-synthesized FeP3 powder and they make it possible to spot contamination in the latter. In the Raman spectra in Figures 3.8 and 3.9, peaks resulting from FeP2 contamination in the precipitated FeP3 powder are marked by enclosing their energies in parentheses. The only other differences sometimes observed between the red films deposited from FeP2 and the FeP3 powder are very weak bands (not visible in Figures 3.8 and 3.9) near 214, 242, 582, and 619 cm<sup>-1</sup>. These peaks

were not reported for  $\text{Fe}(\text{phen})_3^{2+}$  ions in solution nor  $[\text{Fe}(\text{phen})_3]\text{Cl}_2$ . For the latter, the Raman spectrum reported by Andrade and Temperini appears to show very weak peaks near those energies though they are unlabeled in the spectrum given.<sup>102</sup> It remains ambiguous whether these peaks are expected for the  $\text{Fe}(\text{phen})_3^{2+}$  cation.

### 3.5 X-ray Photoelectron Spectroscopy

Figure 3.10 compares the high-resolution x-ray photoelectron spectra for the synthesized FeP3 powder to that of a red film deposited from FeP2 onto an ITO-glass substrate. The survey spectra for each sample are unremarkable and are not presented in full here; all expected elements are detected. A conductive substrate was chosen for the thin film to help alleviate charging as much as possible during the analysis. The powder sample exhibits severe charging while the film does not charge appreciably on this choice of substrate. Even though an attempt has been made to correct for charging effects by shifting the high resolution spectra, the amount of this shift is based on separate scans of the C(1s) region and the extent of charging is assuredly different between each scan/region. For this reason, the absolute peak positions for the powder spectra should not be taken to be accurate. The collection parameters were optimized in each region to obtain the best quality spectra. Since the collection parameters for each region are different, it is not possible to determine the relative atomic concentrations for each element from these spectra. The spectra can still be compared qualitatively.

The number and shape of the peaks in each region are the same for the film and the powder with the caveat that the powder peaks are somewhat broadened. This, too, likely originates from the charging experienced by the powder. The top panel (panel *a*) in Figure 3.10 shows the Fe(2p)

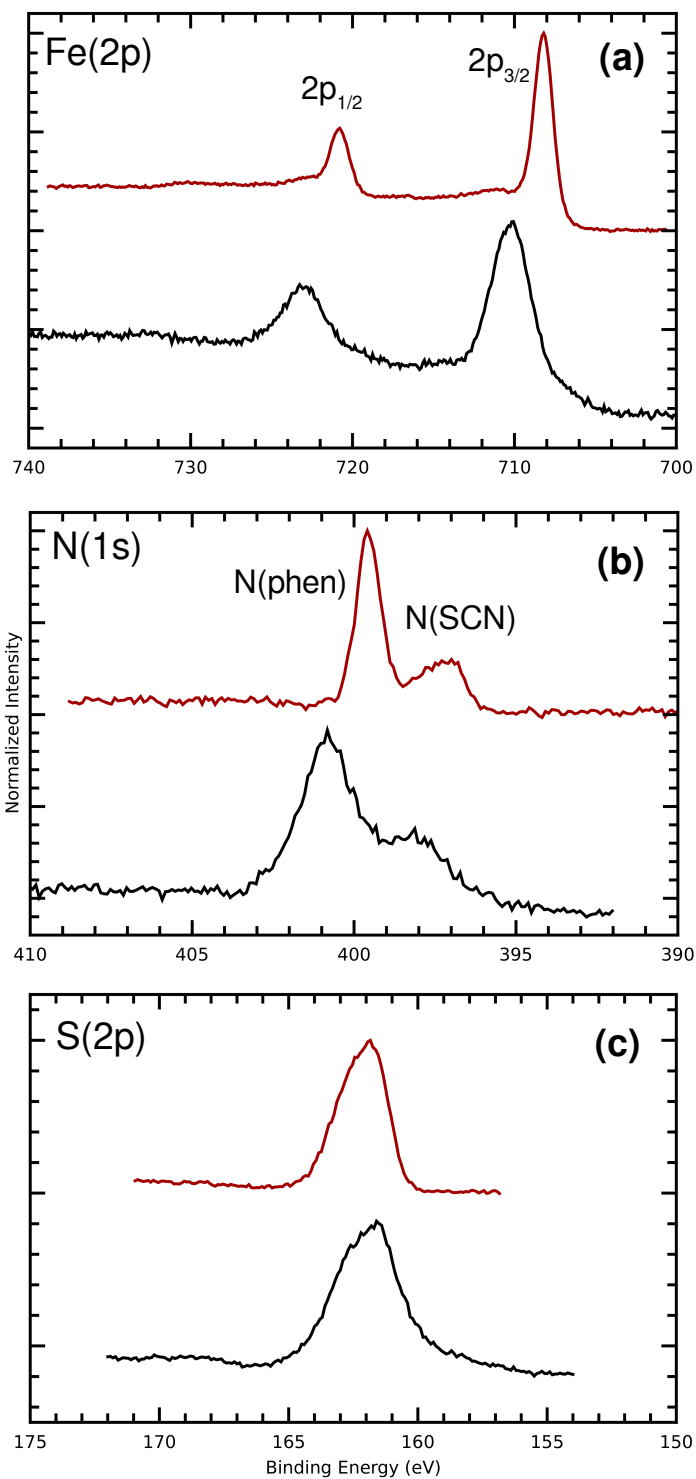


**Figure 3.10.** X-ray photoelectron spectra ( $Al K_{\alpha}$ ) of FeP3 powder (bottom traces in each panel) and of a film deposited onto ITO/glass from FeP2 powder (top traces). Three regions are shown, the Fe(2p), N(1s), and S(2p) in panels *a*, *b*, and *c*, respectively.

region for each sample. Both lack any shake-up satellite peaks which indicates that the Fe present in both exists in a low spin state since such satellites are only expected for paramagnetic Fe.<sup>105</sup> Despite the disparity between the absolute peak positions of the film and powder due to the charging described above, the relative separation between the Fe( $2p_{3/2}$ ) and the Fe( $2p_{1/2}$ ) is nearly the same for each sample. The separation is 12.8 eV in the case of the FeP3 powder and 12.6 eV for the film. This indicates that the degree of spin-orbit coupling is the same for the Fe in the film as it is for the Fe in the diamagnetic FeP3 powder which could only be the case if the spin states were similar. Thus, the x-ray photoelectron spectra suggest that the red films deposited from FeP2 are diamagnetic, whereas FeP2 powder at room temperature is paramagnetic. The possibility that the films might be comprised of FeP2 trapped in the LS state should be considered highly unlikely since spin-state trapping occurs primarily only for the first layer in contact with the substrate.<sup>27,76</sup>

Two different species of N are expected for FeP3 as N is found in the phen ligands and the thiocyanate anions. Indeed, two species are detected for the FeP3 powder here as well as for the red films. The ratio of the N(phen) to N(thiocyanate) is ideally 3 to 1 for FeP3. Deconvolution of the N(1s)-phen and N(1s)-thiocyanate peaks was attempted by subtraction of a Shirley-type background and fitting with GL(30) (30% Gaussian-Lorentzian) curves with the requirement that the FWHM for the two deconvoluted peaks be the same. The N(phen):N(thiocyanate) ratio is found to be about 2.2 for the FeP3 film and 2.5 for the red film by this analysis. That the ratios do not match the ideal ratio is not surprising given the difficulty involved in XPS fitting and peak deconvolution. For example, when the same fitting procedure is applied to the Fe( $2p_{3/2}$ ) and Fe( $2p_{1/2}$ ) peaks whose ratio must necessarily be 2 to 1, respectively, values of ~2.5 are found for both the FeP3 powder and the red films.

After fitting the two N(1s) peaks in each spectrum as described, it is possible to compare the relative separations of these peaks. The peak positions from fitting are much less affected from the choice of baseline subtracted, fitting model, or fitting parameters. For the FeP3 powder, the N(1s)-phen peak occurs 2.8 eV higher than does the N(1s)-thiocyanate peak. The separation of the two peaks in the film spectrum is about 2.3 eV. The difference of 0.5 eV is probably significant, even considering the uncertainty introduced by peak broadening from charging of the powder sample. Still, the N(1s)-phen to N(1s)-thiocyanate separation for FeP2 is ~ 1 eV less than either observed in these samples (see Chapter 4). The chemical environments of the film N atoms appear more similar to those of the FeP3 powder but with a slight modification. This modification might be explained by a difference in crystalline structure (or lack thereof); powder XRD presented in a previous section indicated that the red films are amorphous whereas the FeP3 powder is polycrystalline.

Finally, only one species of S is detected for both the FeP3 powder and the red film. This is consistent for the formula and structure of  $[\text{Fe}(\text{phen})_3](\text{SCN})_2$ . Because impurities have already been identified by vibrational spectroscopy in the precipitated FeP3 powder, another potential source of S from the  $\text{SO}_4^{2-}$  anions of the  $\text{Fe}(\text{NH}_4)_2(\text{SO}_4)_2 \cdot 6\text{H}_2\text{O}$  must be considered. Highly oxidized S is expected to show a S(2p) binding energy between 168 to 171 eV, far above that expected for thiocyanate and the peaks observed here. The possibility of contamination from  $\text{SO}_4^{2-}$  is rejected.

### 3.6 Summary

When attempting to deposit films by thermally evaporating FeP2 under the conditions used

in this experiment, vaporization occurs by liquefaction of the deposition material followed by evaporation and then condensation on the substrate. The process is erratic and difficult to control yet produces smooth red films reliably. Without further treatment (i.e. annealing) the films are highly sensitive to the air, most likely to the humidity in the air. As-deposited films roughen usually within an hour or two forming surface patterns and geometries that suggest crystallization is occurring. The rate of deterioration of the film surface increases with the temperature of the sample upon removing it from the deposition chamber as well as the quality of the starting material.

The evidence from the electronic, vibrational, and photoelectronic characterization of the films deposited from FeP2 overwhelmingly supports the conclusion that the films produced are in fact FeP3 and not FeP2. This conclusion is reached in contrast to that of a previous study even while the films share similar spectroscopic characteristics.<sup>26</sup> If the identification of these films as FeP3 is accepted, it must be the case that during deposition, FeP2 decomposes and the rearranges to yield FeP3. Other unidentified products must necessarily result. This conclusion is supported as well by the observation of charring of the deposition boat. Thus, in the course of this study, a successful method for direct deposition of FeP2 films by thermal evaporation has not been realized. However, an indirect route to the production of FeP2 films was later developed and is described in the next chapter.

## CHAPTER 4

### PREPARATION AND CHARACTERIZATION OF $\text{Fe}(\text{phen})_2(\text{NCS})_2$ FILMS

#### 4.1 Physical Vapor Deposition from $\text{Fe}(\text{phen})_2(\text{NCS})_2$ into Glass Beakers

During a normal deposition onto a substrate, the top surface of the substrate is inverted and not visible through the chamber window. As described in Chapter 3, during deposition of FeP3 films from FeP2 powder, the material in the deposition boat vaporizes in a highly irregular way, with small patches suddenly liquefying and vaporizing. This leads to questions about how the deposition of film proceeds on the samples' surfaces. In order visually monitor the deposition with the hope of correlating these spurts of vaporization with resultant film growth, it was decided to cover the deposition boat with a transparent glass container.

When an overturned beaker (e.g. 400 mL) is placed over the deposition boat, the film grown from the deposition can be monitored visually by looking through the chamber viewport and through the transparent walls of the beaker. This solution has the advantage that the directionality of the deposition can also be observed. In the early stages of deposition from FeP2, small white spots nucleate on the glass, concentrated most heavily at the top of the inverted beaker, and grow in two dimensions across the beaker's inner surface, eventually merging to form large areas of an opaque white film. The number of initial white spots and total coverage of this white film is greatest when the starting material is prepared by thermal decomposition from FeP3 and varies from batch to batch. Typically, not more than the upper third of the overturned beaker is covered

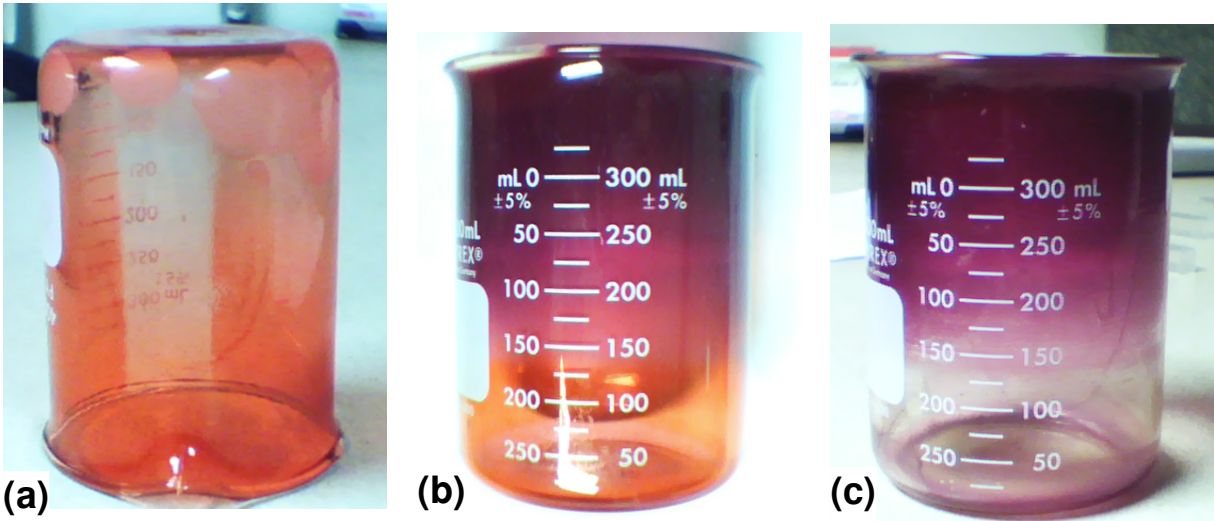


**Figure 4.1.** Example of white spots and red film deposited onto the inside of a beaker covering the deposition boat during heating of  $\text{FeP}_2$  (a). After the growth of the white spots ends, deposition into a second beaker shows only red film growth until the heat from the electrodes becomes intense enough to turn the red film purple (b). An ethanol rinse preferentially removes remaining red film (c).

by the white film before its growth ceases. Then, if the deposition material is recovered from the boat and used in subsequent depositions no white film results, showing that its source is removed from the FeP2 powder during the first use. After this observation, FeP2 prepared by the thermal decomposition method was thereafter heated in the vacuum deposition chamber until white film growth ceased before it was used subsequently to grow films on substrates for analysis. FeP2 prepared by direct precipitation in a solution of excess iron at low pH (see Chapter 2) does not produce a noticeable amount of white condensation. Once this direct, high-yield, aqueous synthesis method for FeP2 was discovered, bulk material was no longer synthesized by thermal decomposition of FeP3.

It is likely that in synthesizing FeP2 via thermal decomposition from FeP3, the phen liberated from the FeP3 molecules remains trapped in the powder matrix as an impurity and is then liberated within the deposition chamber in the early stage of heating, producing the white spots and film. Phenanthroline is easily sublimed and grows long white needles on condensing. If not present purely as an impurity, the phen might be evolved from residual FeP3 present in the FeP2 powder.

After the white film growth has ceased, or in cases where no white film is observed, the next event is the uniform growth of a clear red film that darkens with increasing thickness but remains always perfectly transparent (within the chamber). Growth of the red film continues until the FeP2 powder is exhausted. Upon removing the beakers, it was noticed that the film near the open end of the beaker was sometimes an opaque purple instead of red. When rinsed with water or ethanol, the red film removes easily but the purple film is left intact. Purple is the color of bulk FeP2 powder which is insoluble in common solvents.

## 4.2 Effect of Post-Annealing [Fe(phen)<sub>3</sub>](SCN)<sub>2</sub> Films

From the observation of the purple film, especially its color, from the beaker experiments, it was hypothesized that conversion from FeP3 to FeP2 was occurring near the open end of the beaker starting at the lip and moving up the beaker walls. Heat from the deposition boat transferred through the metal electrodes with which the beaker was in contact was identified as the source of this possible conversion. It was thought that the deposited FeP3 film was pyrolyzed to form FeP2 in the same way that FeP2 powder can be prepared by pyrolysis of FeP3 powder. Since a beaker is not a substrate that lends itself to easy analysis, this hypothesis was tested by depositing FeP3 films onto Si substrates (~600 nm artificial oxide) and annealing them in situ afterwards to different temperatures.

The transmission FT-IR spectra collected from these samples are shown in Figure 4.2. Spectra are shown for annealing temperatures between 80 and 270 °C. Lower annealing temperatures did not significantly affect the spectra of the FeP3 films. The large abnormalities that occur between 1000 and 1300 cm<sup>-1</sup> are due to imperfect background correction of the substrate oxide layer. The size of the abnormality is correlated to the size of a broad lobe near 770 cm<sup>-1</sup> that has the same origin. These effects give rise to some uncertainty in assignment of peaks in the low energy region so they will not be discussed in detail here. It seems certain, however, that the relative intensities for the carbocyclic and heterocyclic ring deformation modes near 845 and 725 cm<sup>-1</sup>, respectively, decreases as the temperature is raised. This may be a sign that concentration of phen (as a ligand) decreases.

The most obvious changes to the spectra occur in the region of the N-CS stretch. At 80 °C, the single mode that occurs at around 2050 cm<sup>-1</sup> in FeP3 has broadened and shifted to 2060 cm<sup>-1</sup>.

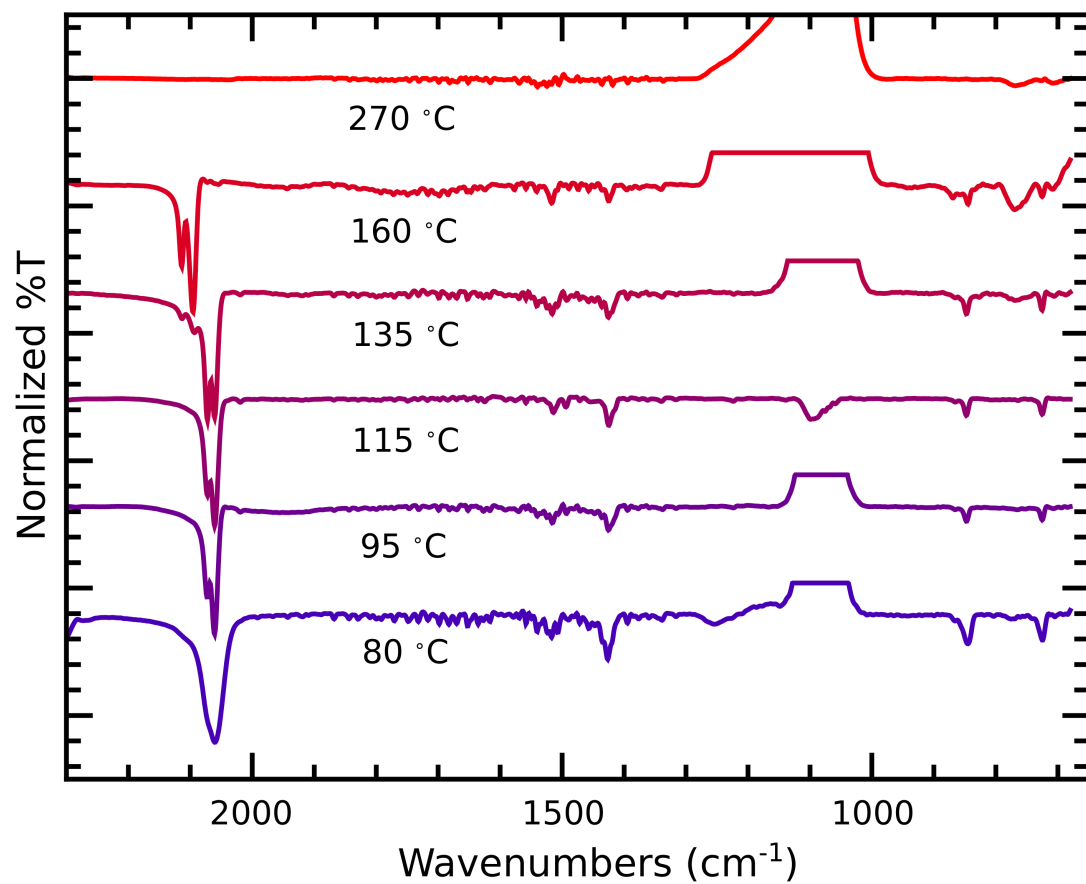


**Figure 4.2.** Transmission FT-IR of films deposited from FeP2 onto Si substrates and then annealed in situ to the temperatures indicated for 8 hrs.

The single mode transforms into two distinct peaks at 2072 and 2060  $\text{cm}^{-1}$  for annealing temperatures of 95 °C and 115 °C. This doublet survives to 135 °C but is joined by a second, higher energy doublet at 2014/2094  $\text{cm}^{-1}$ . By 160 °C little remains of the 2072/2060  $\text{cm}^{-1}$  doublet while the 2014/2094  $\text{cm}^{-1}$  doublet is dominant. Finally, at the extreme temperature of 270 °C all traces of analyte have vanished indicating that the film decomposes or evaporates by this point.

These FT-IR spectra of the films annealed to 95 and 115 °C are found to be compatible with that of FeP2 as shown in Figure 4.3. The spectrum presented comes from a film deposited onto a KBr crystal and does not suffer from background correction effects as do films measured through Si wafers with thick oxides. During pyrolysis of FeP3 and its conversion to FeP2, a phen ligand is lost and the two thiocyanate anions join the  $\text{Fe}^{2+}$  center through the N atoms in a *cis* arrangement. This arrangement, as opposed to a *trans* arrangement, yields a characteristic doublet in the case of the N-CS stretching mode.<sup>99</sup> The narrowness of this doublet in the case of the annealed films suggests that the transformation from FeP3 to FeP2 is complete at temperatures between 95 and 115 °C. It also implies a higher degree of order for the film in comparison to the FeP2 powder.

At temperatures higher than 115 °C, the N-CS doublet moves to even higher energy. There are four possible origins for this shift: 1) reorganization of the metal d-electrons to a LS configuration, 2) a change in coordination of the thiocyanate ligands to M-SCN bonding, 3) a change in coordination of the thiocyanate ligands to M-NCS-M bonding (bridged), or 4) a combination of the aforementioned effects. A switch to a LS configuration is easily ruled out. The  $\nu(\text{N-CS})$  modes are known to occur at 2107 and 2110  $\text{cm}^{-1}$  in LS FeP2 and, more importantly, the HS state is the thermodynamic ground state at room temperature. This fact would remain

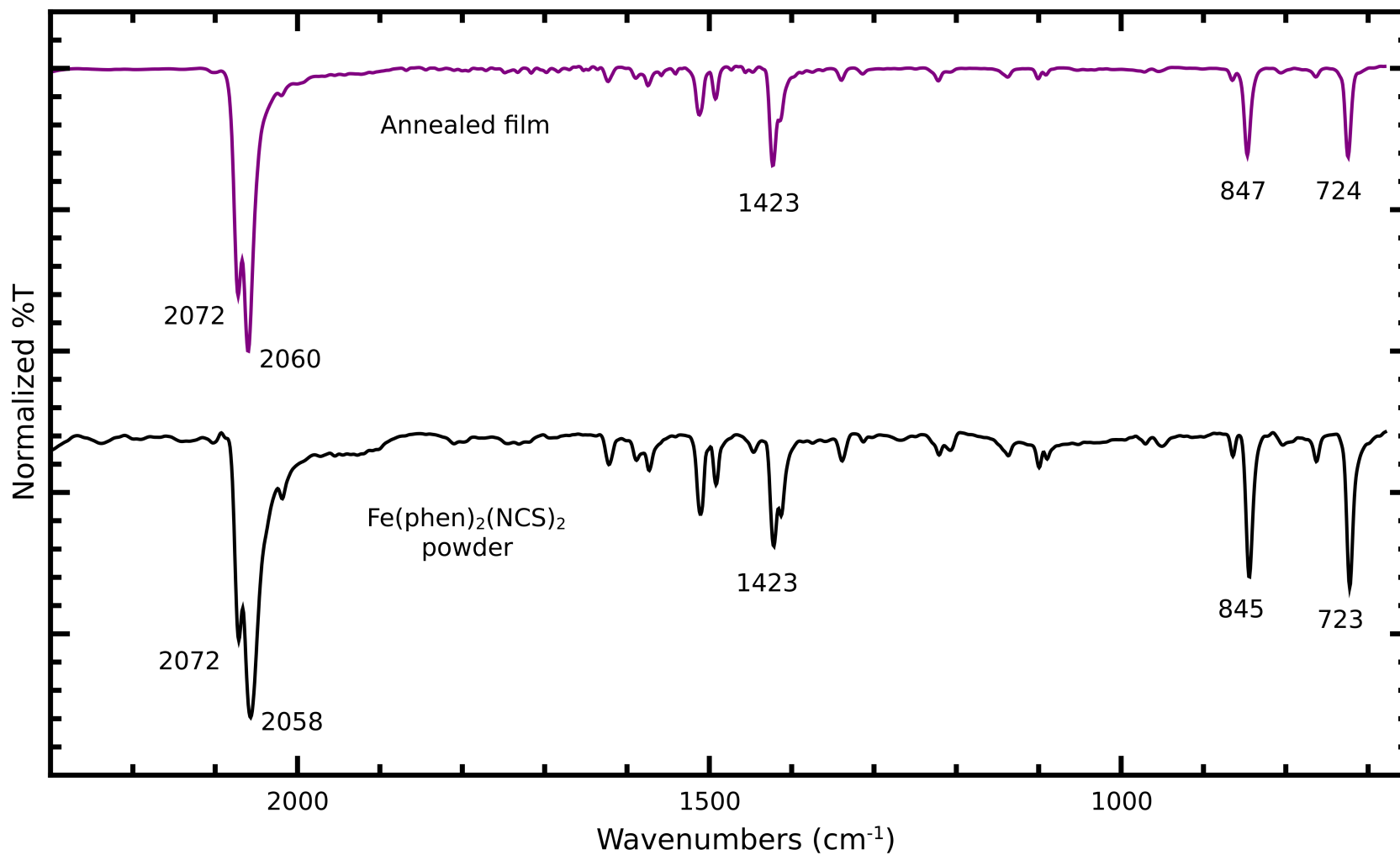


**Figure 4.3.** FT-IR spectrum in the region from 680 to 2300 cm<sup>-1</sup> of FeP2 powder (bottom) compared to that of a purple film on a KBr substrate produced by annealing an FeP3 film (top).

unchanged in the event that another phen ligand is lost from FeP2, i.e. the total ligand field is reduced. A simple change to S-bonded NCS is also unlikely regardless of whether a phen ligand is lost upon heating to these temperatures. Fe being a hard, first row transition metal and N a hard base, complexation exclusively through the softer S end of the thiocyanate ligand would be less stable. Therefore, the most probable explanation for the increase of the  $\nu(\text{N-CS})$  frequencies is a change in coordination mode to a M-NCS-M bridging configuration. To accommodate polymerization, either a phen ligand or NCS ligand must be liberated from each FeP2 molecule. Since two thiocyanate ligands are required in order to balance the charge of each  $\text{Fe}^{2+}$  center, it is most likely the case that a phen ligand is lost from each FeP2 molecule and a coordination polymer,  $\text{Fe}(\text{phen})(\text{NCS})_2$  (hereafter FeP1) is formed.

Only two prior reports of FeP1 could be found in the literature but neither were conclusive. In a series of papers spanning 1948-1950, Lee and coworkers saw evidence for its formation at low concentration in aqueous solution while studying the formation and dissociation of FeP3 at low pH.<sup>88,106,107</sup> And, Gasgnier et al. suspected to have formed FeP1 by thermal decomposition of FeP2 in a transmission electron microscope after discovering a new polycrystalline phase at high temperatures.<sup>108</sup> However, the analogous species  $\text{Fe}(\text{bipy})(\text{NCS})_2$  was prepared by Dockum and Reiff in 1982.<sup>109,110</sup> Notably, this compound was prepared by thermal decomposition of the parent compound  $\text{Fe}(\text{bipy})_2(\text{NCS})_2$  which might be called a sister complex of FeP2. In comparing the vibrational spectra, these authors found that the  $\nu(\text{N-CS})$  frequencies shifted from around 2062  $\text{cm}^{-1}$  (unresolved doublet) in the parent complex to 2110 and 2080  $\text{cm}^{-1}$  once a bipy ligand was lost. The structure of  $\text{Fe}(\text{bipy})(\text{NCS})_2$  was suggested to be a 1D zigzag coordination polymer and this has recently been confirmed by single crystal XRD.<sup>111</sup> An analogous structure is therefore suggested

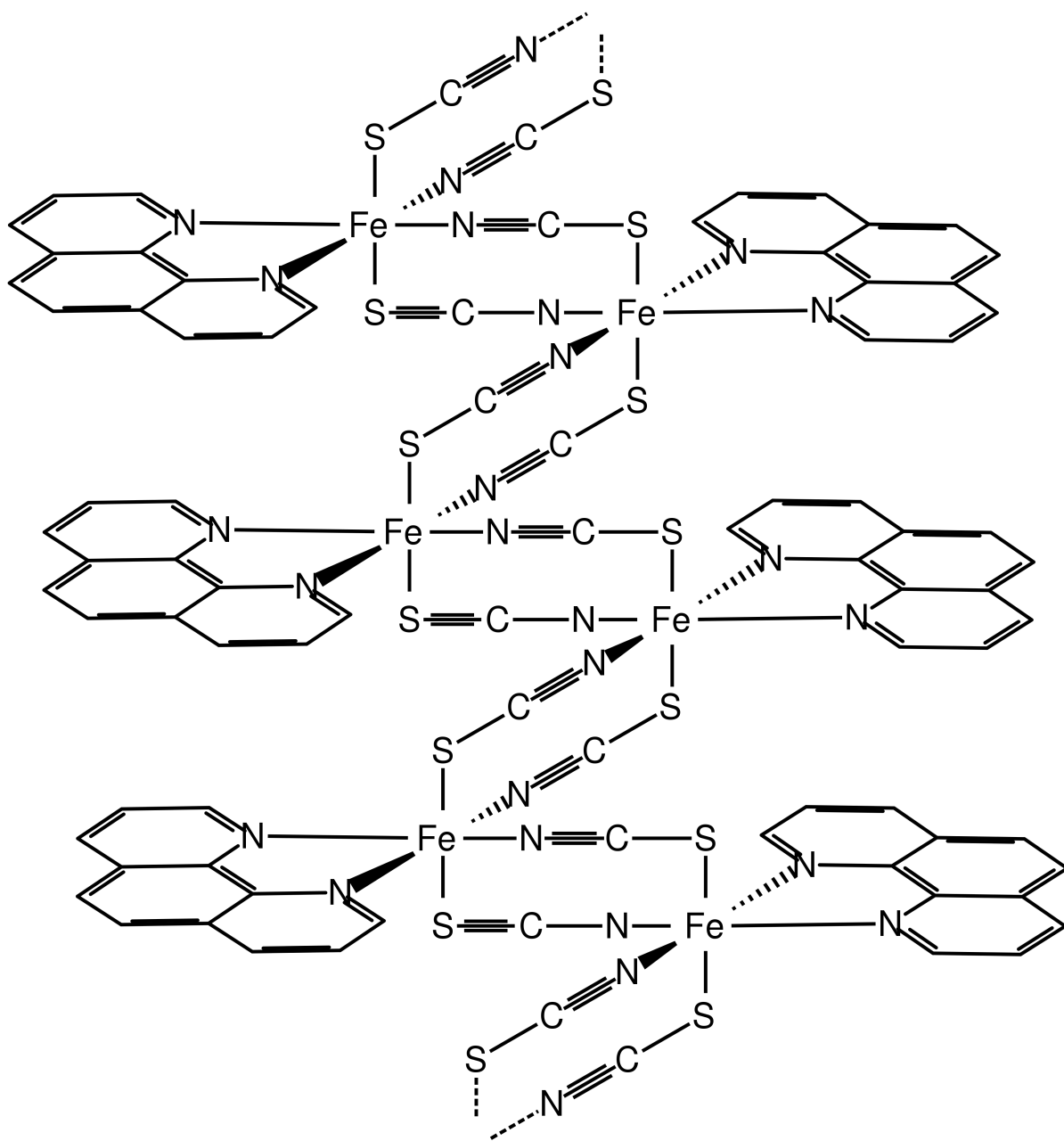


**Figure 4.4.** Proposed structure for FeP1 1D coordination polymer.

for FeP1 and is presented in Figure 4.4. In this structure, the isothiocyanate linkage is linear whereas the thiocyanate coordination occurs at an angle ( $\angle MSC \sim 107^\circ$ ). This type of thiocyanate coordination is common and has been suggested to stabilize the M-S bond by allowing increasing  $\pi$  interactions between the ligand and metal.<sup>112</sup> With respect to the expected magnetic behavior of FeP1, Dockum and Reiff found that  $\text{Fe}(\text{bipy})(\text{NCS})_2$  was high spin at all temperatures above 20 K with the magnetic moment decreasing only at very low temperatures due to antiferromagnetic interactions between  $\text{Fe}^{2+}$  centers.<sup>109</sup> FeP1 is thus not expected to exhibit any SCO activity. It must be noted that isolation of FeP1 via thermal decomposition of FeP2 was otherwise unexpected since no such species appeared in the thermogravimetric analysis performed here or by other authors.<sup>81,113</sup> This leads one to suspect that formation of FeP1 by thermal decomposition of FeP2 is a kinetically controlled process.

Raman spectra for the post-annealed films were measured and are presented in Figure 4.5. Once again, when annealed to only 80 °C, the spectrum matches that of FeP3. Whereas the broad N-CS mode in the FT-IR spectrum suggested that some FeP2 might also be present, no peaks other than those that could be attributed to FeP3 were found in the Raman spectrum. At the other temperature extreme, at 135 °C the peaks due to the substrate begin to dominate the spectra and at 270 °C only substrate peaks can be detected.

Annealing temperatures of 95 and 115 °C produced Raman spectra that were entirely compatible with that of the FeP2. The spectrum of a film annealed to 115 °C is compared with FeP2 powder in detail in Figures 4.6 and 4.7. The low energy region (Figure 4.6) is especially important in identifying these films as FeP2 instead of FeP3. In the paramagnetic FeP2, the Fe-N(phen) and Fe-NCS stretches occur near 220 and 250  $\text{cm}^{-1}$ , respectively, as confirmed

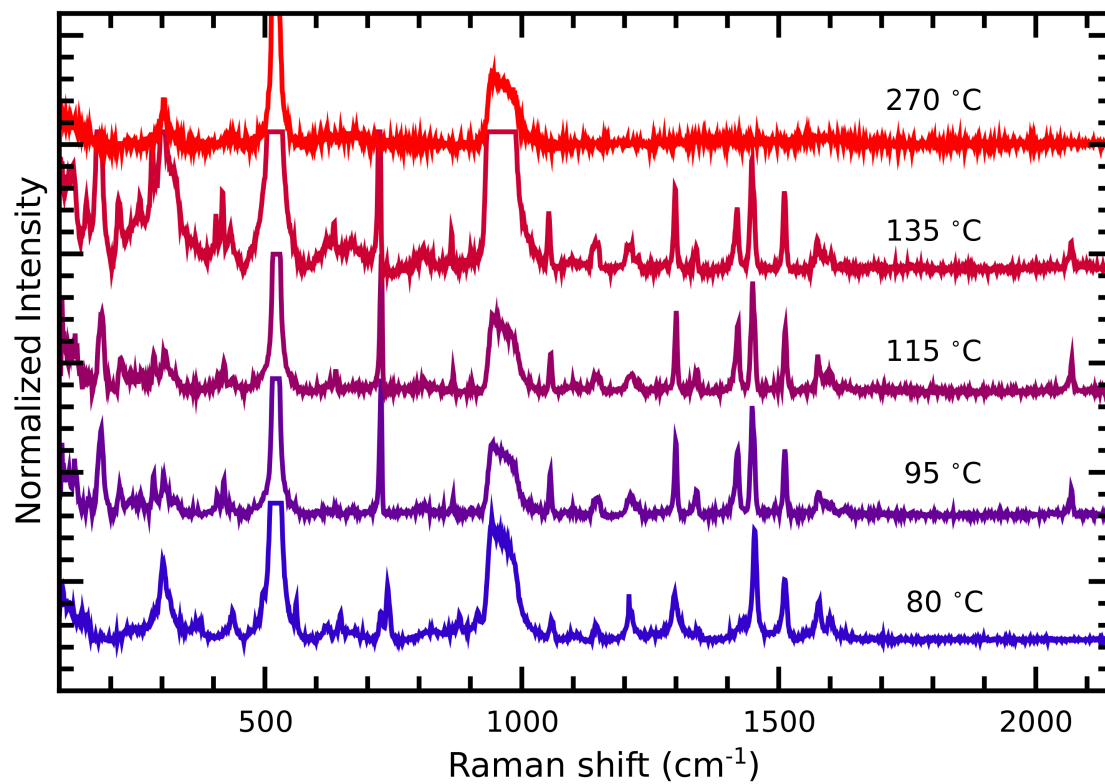


**Figure 4.5.** Raman spectra of films deposited from FeP2 onto Si substrates and then annealed in situ 8 hrs at different temperatures. The spectrum of the film annealed at 270 °C represents the spectrum of the Si substrate.

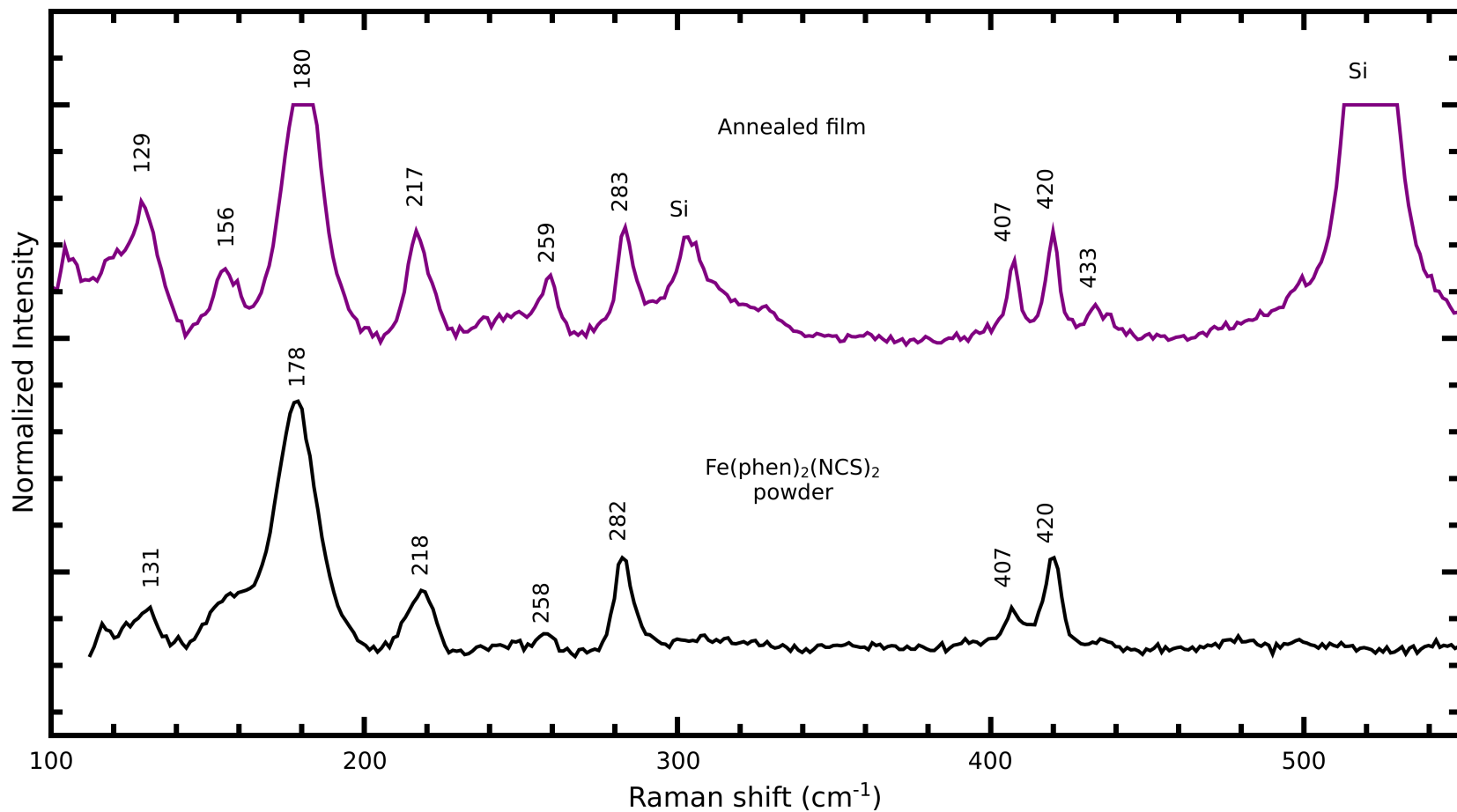


**Figure 4.6.** Raman spectrum in the region from 150 to 500  $\text{cm}^{-1}$  of FeP<sub>2</sub> powder (bottom) compared with that of a purple film on a Si substrate made by annealing an FeP<sub>3</sub> film at 115 °C for 8 hr (top). Features around 300 and 520  $\text{cm}^{-1}$  in the film spectrum are due to the Si substrate.

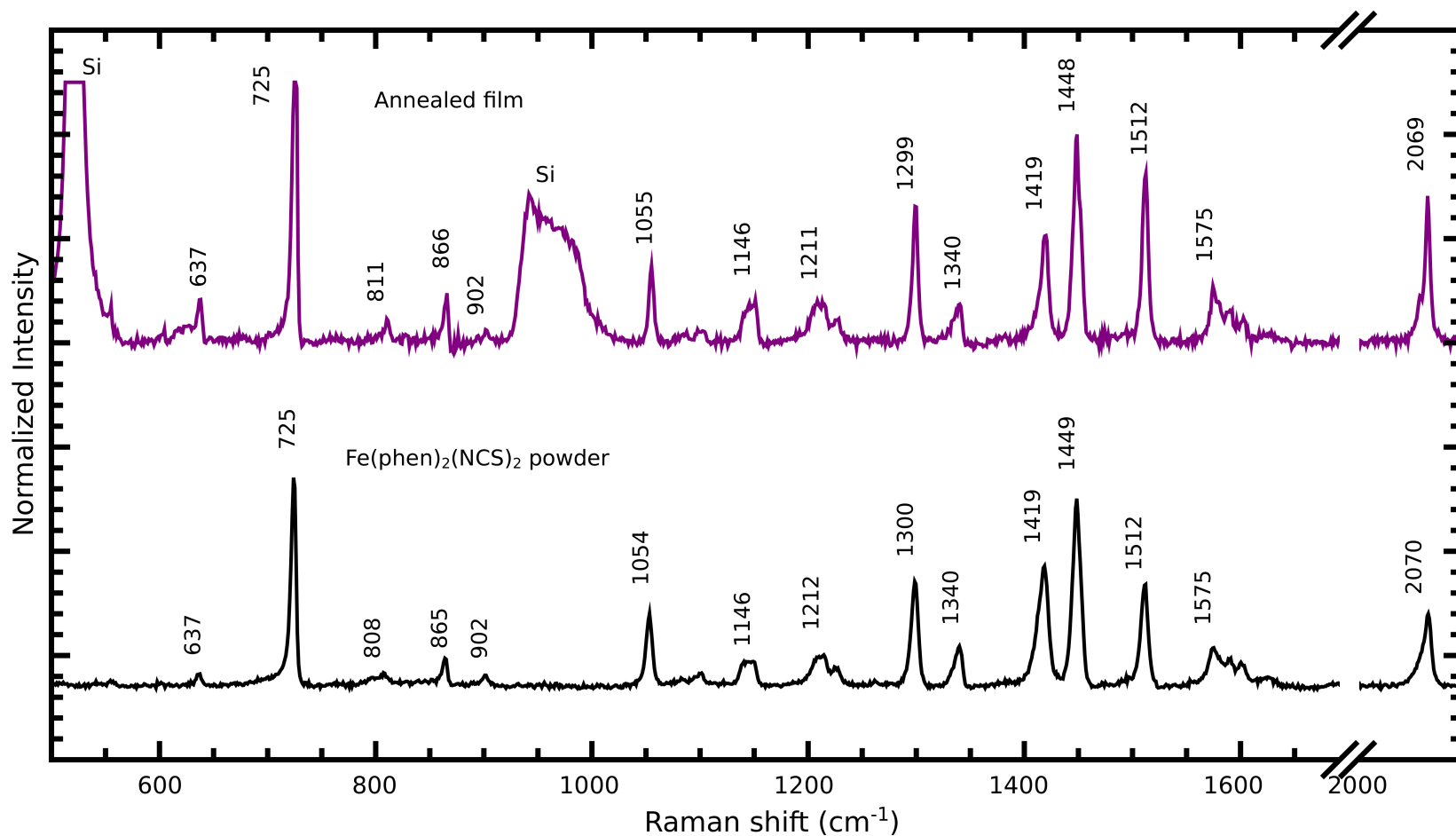


**Figure 4.7.** Raman spectrum in the region from 500 to 2100  $\text{cm}^{-1}$  of FeP<sub>2</sub> powder (bottom) compared with that of a purple film on a Si substrate made by annealing an FeP<sub>3</sub> film at 115 °C for 8 hr (top). Features at 520 and around 950  $\text{cm}^{-1}$  in the film spectrum are due to the Si substrate.

previously by  $^{15}\text{N}$  and  $^{13}\text{C}$  isotopic labeling.<sup>104</sup> Both modes are found to be present in the films annealed to 95 and 115 °C. The relatively low energy of these modes reflects the longer Fe-N bond lengths of paramagnetic, HS FeP2. In comparison, when FeP2 transitions to the LS form, the Fe-N bonds shorten roughly 10% and the modes shift to 366 and 375  $\text{cm}^{-1}$ .<sup>104</sup> Similarly, the Fe-N(phen) stretch of FeP3, a diamagnetic species, occurs at 368  $\text{cm}^{-1}$  and is not present in the spectrum of the purple film.

A few higher energy ligand modes also assist in distinguishing FeP2 and FeP3. In the latter, two peaks at 724 and 738  $\text{cm}^{-1}$  are observed near the position expected for the heterocyclic ring deformation. As seen in Figure 4.7, in the case of FeP2, only the mode at 724  $\text{cm}^{-1}$  is observed and its intensity is increased relative to the same mode in FeP3. Therefore, the 738  $\text{cm}^{-1}$  mode is especially useful for identifying the presence of FeP3 in the synthesized FeP2 as well as the annealed films. Likewise, the strong peak near 1420  $\text{cm}^{-1}$  is found only in the case of FeP2 and is a simple and sensitive means for detecting FeP2 as an impurity in FeP3 powders and films. Of course, the N-CS stretch near 2070  $\text{cm}^{-1}$  is another indicator of FeP2, as this mode is not Raman active in the case of FeP3.

Based on the vibrational spectroscopy data presented, the purple films annealed between 95 and 115 °C are identified as FeP2, the target molecule. A complete list of observed vibrations are given in Table 4.1 for such samples. Further characterization was completed on films annealed to 115 C for 8 hrs and is discussed below. Additionally, while lower temperatures yielded only FeP3 films, those films have much less sensitivity to air vs. as-deposited films. It is believed that the as-deposited FeP3 films may contain phen as an inclusion which can be driven from the film by heat. Or, annealing may allow the relaxation of the film to some lower energy physical structure. In any

**Table 4.1.** Peak positions and peak assignments<sup>a</sup> from the vibrational spectroscopy of FeP2 powder compared to purple films made by annealing as-deposited films<sup>b</sup> identified as FeP2.

Fe(phen) <sub>2</sub> (NCS) <sub>2</sub> purple film					Fe(phen) <sub>2</sub> (NCS) <sub>2</sub> purple film				
IR	Raman	IR	Raman	Assignment	IR	Raman	IR	Raman	Assignment
2102 w		2101 w			1221 w	1226 w	1223 w	1224 w	
2072 s	2070 s	2072 s	2070 s	v(N-CS)	1208 w	1212 m	1208 w	1210 m	
2058 s		2060 s		v(N-CS)	1138 w	1145 m	1138 w	1144 m	δ(C-H)
2040 sh				v(N <sup>13</sup> C-S)	1100 w	1101 w	1101 w		
2019 w		2020 w		v(N <sup>13</sup> C-S)	1091 w		1092 w		δ(C-H)
		2000 w			1053 w	1053 s		1054 s	
1974 w					972 w		972 w		
1623 m	1626 w	1623 w			952 w		954 w		
	1601 w		1597 m			902 w		905 w	
1590 m	1590 w	1590 w		v(C-C), v(C-N)	865 m	865 m	865 w	865 m	
1574 m	1575 m	1574 w	1577 s		845 s		845 s		carbocyclic ring deformation
		1558 w			804 w	808 w	805 w	808 w	v(NC-S)
		1541 w			792 w				
1512 m	1512 s	1512 m	1512 s		764 m		763 w		
1493 m		1492 m			723 s	725 s	724 s	725 s	heterocyclic ring deformation
		1474 w				636 w		636 w	
		1456 w						559 w	
1447 w	1448 s	1448 w	1449 s			419 m		419 m	
1422 s	1419 s	1423 s	1420 s			406 w		406 w	
1413 m		1414 sh				282 m		282 s	
1340 m	1340 m	1340 w	1341 m			257 w		258 w	v(Fe-NCS)
1314 w		1314 w				217 m		218 m	v(Fe-N(phen))
	1299 s		1300 s			177 s		179 s	
1268 w						155 w		154 w	

<sup>a</sup> Assignments are based on references 73, 104, and 114. <sup>b</sup> IR comes from a film on KBr, Raman from a film on glass.

case, the practice of annealing FeP3 films after deposition to temperatures between 70 and 80 °C was adopted to improve shelf-life to better than a few days before films would eventually roughen.

It should be noted that the annealing conversion was also attempted under low moisture N<sub>2</sub> atmosphere and in air by heating samples on the surface of a hot plate in a glove box or on the lab bench, respectively. Both sets of conditions produced films with the same vibrational signatures as those annealed under high vacuum. Conversion under such conditions was not investigated further however, because of fear of the risk of oxidation of the Fe<sup>2+</sup> centers and because of the limited access to a suitable glove box. Conversion under these conditions would offer the benefits of greatly improved conversion kinetics due to improved thermal transport between the hot plate and the sample (once a critical temperature was reached, samples on the hot plate showed complete conversion within seconds as opposed to several hours under high vacuum), simplicity of design (no need to have heater wire and thermocouple feedthroughs in vacuum chamber, no need for sophisticated temperature controller), and the ability to perform standard analyses during the conversion process (such as Raman microscopy, etc.). These conditions might also affect the morphology (Section 4.4) of the FeP2 films which was found to be a limiting factor in electrical characterization (Chapter 5) .

### **4.3 Further Spectroscopic Characterization of Fe(phen)<sub>2</sub>(SCN)<sub>2</sub> Films**

By using glass substrates, it is possible to record electronic spectra of the FeP2 films in the visible region. Figure 4.8 shows such a spectrum. A broad peak is observed with  $\lambda_{\text{MAX}} = 551 \text{ nm}$  and with a shoulder at 525 nm which together give rise to the purple color the films. It is assumed that the origin of this absorption is the same as found in FeP3, that is a  $d^6 \rightarrow \pi^*$

metal-to-ligand-charge-transfer (MLCT).<sup>90</sup> The same assignment has been made by other authors.<sup>63,65,70,115,116</sup> Compared to FeP3, the position of the MLCT band is red-shifted which reflects the change from a *tris* phen coordination to a *bis* arrangement. With fewer phen ligands, the degree of interaction between the metal  $t_{2g}$  orbitals and ligand  $\pi^*$  orbitals, known as  $\pi$ -backbonding, is reduced. The  $t_{2g}$  orbitals therefore lie higher in energy and the MLCT energy gap is decreased. The coordination of the thiocyanate ligands is not expected to contribute to metal-ligand backbonding as strongly as phen.<sup>81,112,115</sup> Additionally, it has been observed that the spin state, which changes from LS to HS when comparing FeP3 to FeP2, has only a minor effect on the position of the MLCT band.<sup>63</sup>

In analogy to the assignment of the low energy shoulders in the spectrum of FeP3 (see Chapter 3), the low energy shoulder observed here at 525 nm is expected to arise from vibronic coupling. The energy spacing between the shoulder and absorption maximum is found to be about  $900\text{ cm}^{-1}$  which lies close in energy to a strong peak observed in the Raman spectrum at  $1055\text{ cm}^{-1}$ , though any definite relationship remains unproven.

A thorough exploration of the literature turns up several studies concerning the electronic spectra of FeP2.<sup>26,65,70,81,83,115-120</sup> Among these reports, there is found a variation in the spectra and reported absorption maxima such that no two existing works are entirely consistent. The differences might arise because of differences in sample quality or treatment.<sup>118</sup> The spectrum presented in this work agrees well with that presented by Konig and Madeja and shares at least the general shape of spectra presented by other authors.<sup>70, 117, 118, 120</sup>

In the x-ray photoelectron spectra of FeP2, there are three regions of primary interest: the Fe(2p), N(1s), and S(2p) regions. All three regions are presented for the FeP2 films and powder in

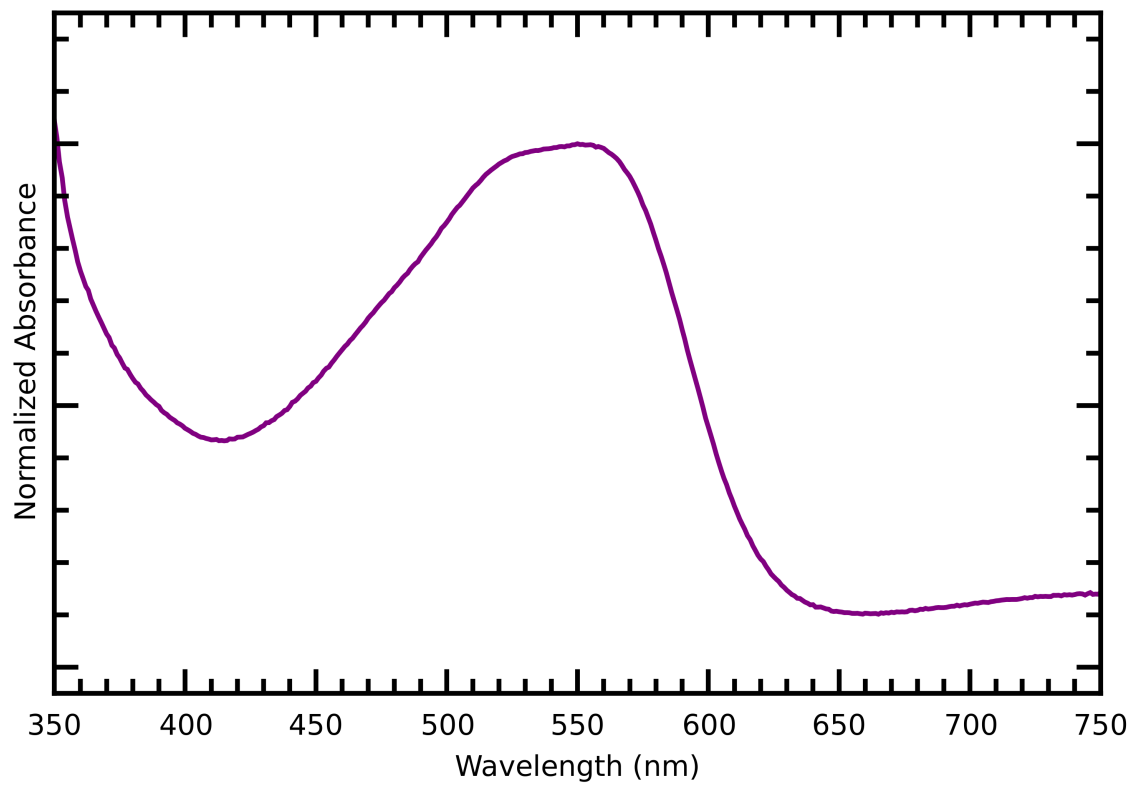


**Figure 4.8.** UV-Vis spectrum of a purple film on glass made by annealing an FeP3 film deposited from FeP2. The absorbance maximum occurs at  $\lambda_{\text{MAX}} = 551$  nm.

Figure 4.9. Not surprisingly, sample charging was problematic in the case of the powder samples. Owing to this, peaks are broad and unresolved and there is much uncertainty in their absolute binding energies, even after correction by shifting the spectra to match the C(1s) to 285 eV. In contrast, charging was not significant in the case of the films.

For either FeP2 sample, powder or film, the Fe(2p<sub>1/2</sub>) and Fe(2p<sub>3/2</sub>) peaks are much broader in comparison to those observed for the FeP3 powder and films (Chapter 3). Higher binding energy satellite peaks of low intensity are clearly evident. Both of these observations can be attributed to the HS electron configuration of FeP2. After the ionization of a 2p electron from the Fe<sup>2+</sup> center, spin-spin coupling of the unpaired 2p electron and the four unpaired 3d electrons results in multiplet splitting of the final 2p states. The convolution of these states gives rise to broad peaks. Also after ionization, the outgoing 2p electron may lose energy in the excitation of a 3d electron. This excitation, termed a shake-up event, is spin-allowed only for paramagnetic 3d electron configurations. Hence, shake-up satellite peaks are observed for HS FeP2 but are absent in the case of FeP3 and other diamagnetic Fe<sup>2+</sup> complexes.<sup>121,122</sup>

In the N(1s) region, two peaks are expected, one for each ligand type. The relative areas should be 2:1 reflecting the relative concentration of each species of N in the complex, i.e. four phen N atoms to every two thiocyanate N atoms. In the spectrum of the FeP2 powder, the two peaks are not resolved due to charging. In the case of the FeP2 films, the peaks are better resolved but still overlapping. Attempts to deconvolute and quantize the component peaks yield lower than expected ratios of N(phen) to N(thiocyanate) in the range of 1 to 1.6, depending on the chosen fitting parameters. It seems evident however, that the N(thiocyanate) component is the minor component but is increased in relative abundance when compared with the same analysis of FeP3.

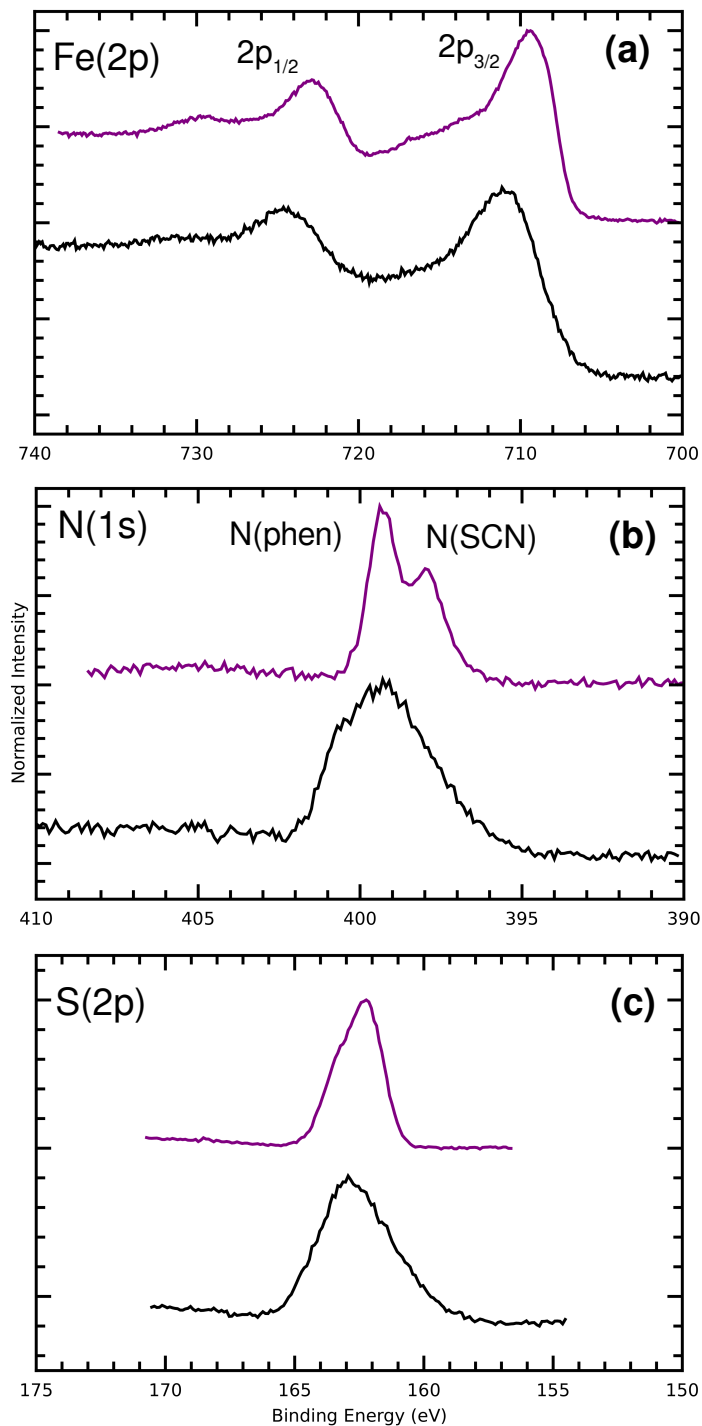


**Figure 4.9.** X-ray photoelectron spectra (Al  $K_{\alpha}$ ) of FeP2 powder (bottom traces in each panel) and of a purple film on ITO/glass made by annealing an FeP3 film in vacuum (top traces). Three regions are shown, the Fe(2p), N(1s), and S(2p) in panels *a*, *b*, and *c*, respectively.

Finally, only one species of S could be identified for the FeP2 films and powders in the S(2p) region. In neither case were the  $2p_{3/2}$  and  $2p_{1/2}$  peaks resolved. Though the peak position is uncertain for the FeP2 powder because of charging, the position observed for the FeP2 film is appropriate for a thiocyanate sulfur atom.<sup>123</sup> The binding energy at the peak maximum (162.2 eV) is slightly higher than that observed for the FeP3 films (161.9 eV). The shift to higher binding energy reflects a reduced concentration of negative charge on the sulfur atom of the coordinated ligand. However, care should be exercised in the interpretation here, since the uncertainty of these binding energies is expected to be on the order of  $\pm 0.2$  eV, at least.

Quantitative elemental analysis is not possible from the presented spectra because scanning parameters (e.g. pass energy and dwell time) were varied between regions to obtain the best quality spectra in a reasonable amount of time. However, relative peak positions of the Fe( $2p_{3/2}$ ) and Fe( $2p_{1/2}$ ) and the N(1s)-phen and N(1s)-thiocyanate peaks can provide qualitative insight, even for the powder spectra where sample charging makes absolute positions uncertain. Table 4.2 shows the relative peak positions for the FeP2 samples compared to those of the FeP3 samples. In agreement with Burger et al., it is found that the Fe( $2p_{3/2}$ )-Fe( $2p_{1/2}$ ) peak separation is greater in the case of the paramagnetic FeP2 samples where spin-orbit coupling is more significant.<sup>105</sup> On the other hand, the N(1s)-phen to N(1s)-thiocyanate separation is reduced for the FeP2 samples compared to the FeP3 samples. Comparison of absolute peak positions is possible only for the thin film samples and shows that the relative separation is due mainly to a shift of the N(1s)-thiocyanate peak to higher binding energy. Donation of electron density from the N to the metal in formation of the dative bond raises the core levels of the coordinated thiocyanate molecule relative to the uncoordinated

**Table 4.2.** Peak positions<sup>a</sup> and peak separations (eV) for the Fe(2p) and N(1s) regions of the x-ray photoelectron spectra of FeP2 and FeP3 powders and films compared with reported values.

		Fe(2p)			N(1s)		
		1/2	3/2	$\Delta$	N <sub>phen</sub>	N <sub>thiocyanate</sub>	$\Delta$
Fe(phen) <sub>2</sub> (NCS) <sub>2</sub>	powder <sup>b</sup>	723.2	709.9	13.3	399.7	398.2	1.5
	film <sup>c</sup>	722.7	709.3	13.4	399.3	397.9	1.4
	Ref. 131	723.7	709.6	14.1			
	Ref. 132	722.6	709.2	13.4	399.0	397.9	1.1
[Fe(phen) <sub>3</sub> ](SCN) <sub>2</sub> <sup>d</sup>	powder <sup>b</sup>	722.8	710.0	12.8	400.8	398.0	2.8
	film <sup>c</sup>	720.8	708.2	12.6	399.5	397.2	2.3

<sup>a</sup> Corrected by matching the C(1s) peak to 285 eV except for Ref. 131 <sup>b</sup> Absolute positions have significant uncertainty (see text). <sup>c</sup> Films on ITO/glass. <sup>d</sup> See Chapter 3.

molecule. Taken together, the Fe(2p) and N(1s) peak separations help to confirm that after post-deposition annealing the FeP3 films have indeed transitioned to FeP2.

#### **4.4 Structural Characterization of Fe(phen)<sub>2</sub>(SCN)<sub>2</sub> Films**

With the chemical identity of the FeP2 films positively identified by vibrational, electronic, and photoelectron spectroscopy, the topography and microscopic structure of the films was investigated. Atomic force microscopy is incredibly well-suited to mapping the three-dimensional surface of films on flat substrates. The intermittent contact mode, or "tapping" mode, has most of the resolution and sensitivity of contact mode scanning but with the benefit of minimizing the lateral force exerted upon the sample surface by the AFM probe tip. AFM scans captured in this mode are shown in Figure 4.10 for the FeP2 films atop three different substrates. In each case the film thickness is between 100 and 200 nm. No systematic study of the effect of film thickness on topography was undertaken, but such an effect was not recognized in the course of the analysis of these and other films.

While other morphologies are occasionally observed, the granular nature of the films shown in Figure 4.10 are by far the most common. Grains are well-defined and irregular in shape. The highest points in the scanned images occur near the centers of grains. These peaks on the film surface typically rise at least 20 nm from the surrounding grain surface. Striations appear to radiate away from these peaks to the grain edges. When small regions are scanned, the striations might be described as strands of material a few hundred nanometers in diameter that give the films a feathered appearance.

The choice of substrate has minor effects on the topography of the FeP2 films. There does

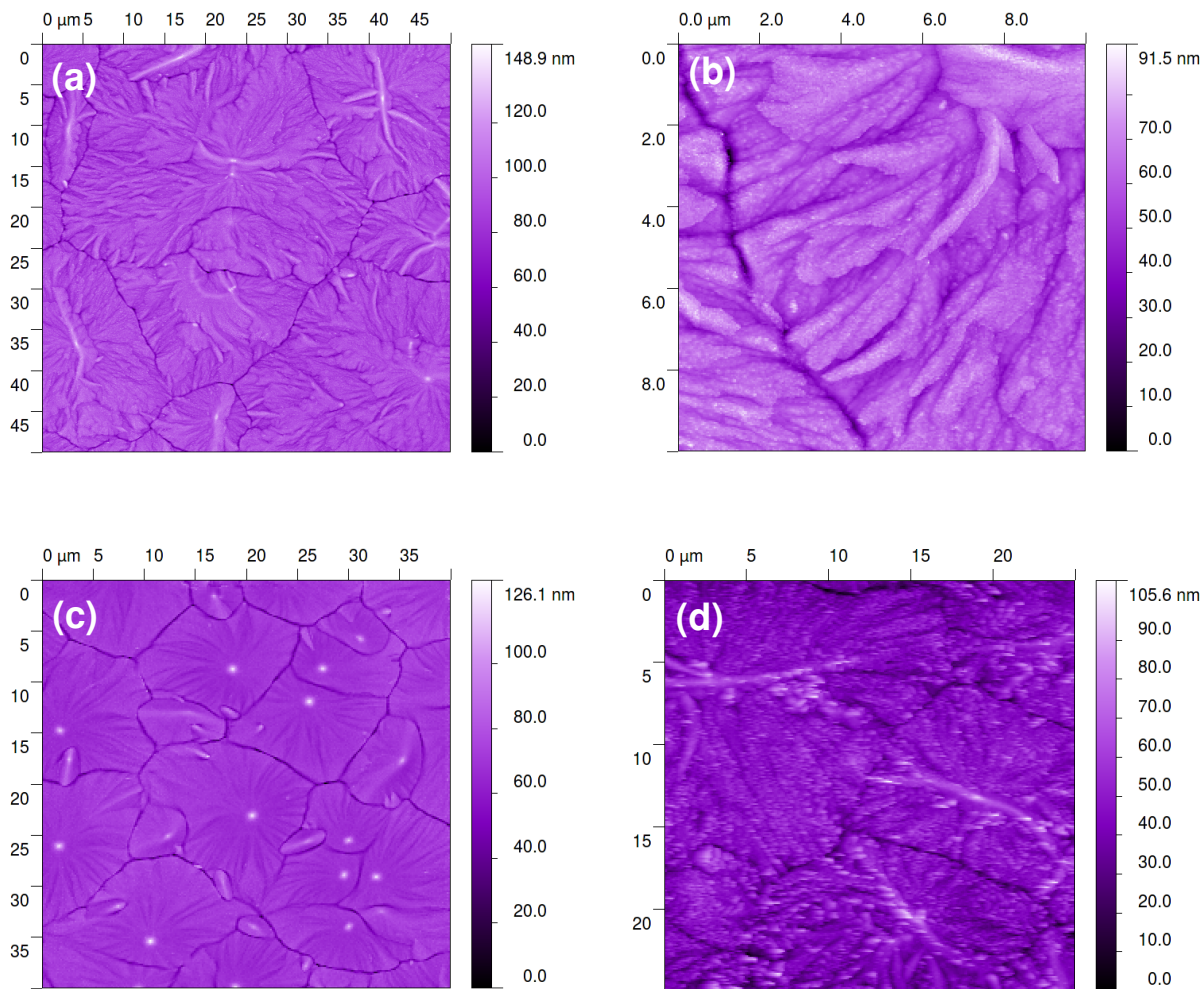


**Figure 4.10.** AFM topography scans of FeP2 films on different substrates. (a) On a Si wafer ( $\text{SiO}_2$ ) covering a  $50 \times 50 \mu\text{m}^2$  area. (b) The same film scanned over a  $10 \times 10 \mu\text{m}^2$  area. (c) Atop a  $\text{Si}(\text{SiO}_2)/\text{Al}(40 \text{ nm})/\text{LiF}(1 \text{ nm})$  layered substrate at  $40 \times 40 \mu\text{m}^2$ . (d) On an ITO covered glass substrate at  $25 \times 25 \mu\text{m}^2$ . The film thickness in each case is within the range of 100 to 200 nm.

seem to be a dependence of the average grain size on the chosen substrate. Films deposited directly atop the bare Si wafer yield the largest average grain size, *ca.* 40 nm. When a metal electrode such as Ag is deposited first on the Si wafer and the film deposited atop the electrode, the typical grain size is reduced to *ca.* 10 nm. The presence of a small ( $\sim 1$  nm) layer of LiF on the metal electrode does not impact the morphology of the grain. The effect of substrate choice on grain size is most clearly recognized for films grown atop Si and a metal electrode on the same surface. The grain size is always smaller for the film that extends over the electrode. The probability for as-deposited FeP3 films to fail to convert to FeP2, in part or fully, is higher for films atop the metal layers. In some samples, the degree of conversion was 100 % for the films on the bare substrate but close to 0 % for films on the metal electrodes directly adjacent. Either the metal films act as an insulating layer preventing efficient heat flow to the FeP3 films above, or the metal acts as a heat sink, maintaining the films a lower temperature than indicated by the thermocouple pressed to the bare Si surface. Therefore, it may be that the temperature at which film conversion occurs controls the grain size.

At the border between two adjacent grains are deep crevices often close in depth to the film thickness (usually measured separately by profilometry). These discontinuities are expected to affect communication of structural changes (SC) across the film laterally. They also have important ramifications for construction of vertical sandwich devices and for electrical measurements made horizontally through a film. This issue is explored further in Chapter 5.

Because of practical limitations, the maximum achievable scan size for an artifact-free AFM image is about  $50 \times 50 \mu\text{m}^2$ . In order to examine larger areas and to determine typical grain features, reflected light optical microscopy was used. The optical photomicrographs presented in Figures 4.11 and 4.12 were taken through the objective of the Raman microscope and captured

by the system's CCD camera. The highest magnification available on the instrument, achieved with a 100x objective, captures an area of roughly  $50 \times 50 \mu\text{m}^2$ . Conveniently, the observable area of the microscope begins just at the point where the area available by AFM ends. The two techniques prove complimentary in this way, though, of course, the surface topography can only be understood in three dimensions through the AFM images.

The optical microscopy reveals that in samples where conversion from FeP3 to FeP2 was not complete across the entire surface area, spots of FeP2 grow within the FeP3 film. Chemical identities are confirmed by collecting Raman spectra from each area independently. In areas dense with FeP2 spots, it can be seen that the intersection of spots leads to the grain structure observed in the AFM. The growth mechanism of the FeP2 films appears to be one of nucleation and growth within the FeP3 film until all of the surrounding film is consumed. Presumably then, the grain density and grain size are directed by the concentration of nucleation sites. As can be seen in Figure 4.11 (and as previously mentioned), for a single film deposited across both the bare Si wafer surface and an Al/LiF electrode (deposited previously atop the Si), size is somewhat larger for the grains formed from the film in contact with the Si. Given that the Al/LiF electrode surface is rougher than the bare Si wafer, the substrate roughness may correlate with the number of nucleation sites and ultimately the FeP2 grain size. In our laboratory, the bare Si wafer surface is one of the flattest and cleanest accessible. So, it is doubtful that the grain density could be reduced nor grain size increased much further through choice of substrate.

After nucleation, as grains grow in size, conversion from FeP3 to FeP2 must result in the loss of mass via the expulsion of one phen ligand from each FeP3 molecular unit. If the volume is reduced concomitantly during the conversion, the direction of shrinkage will be toward the center

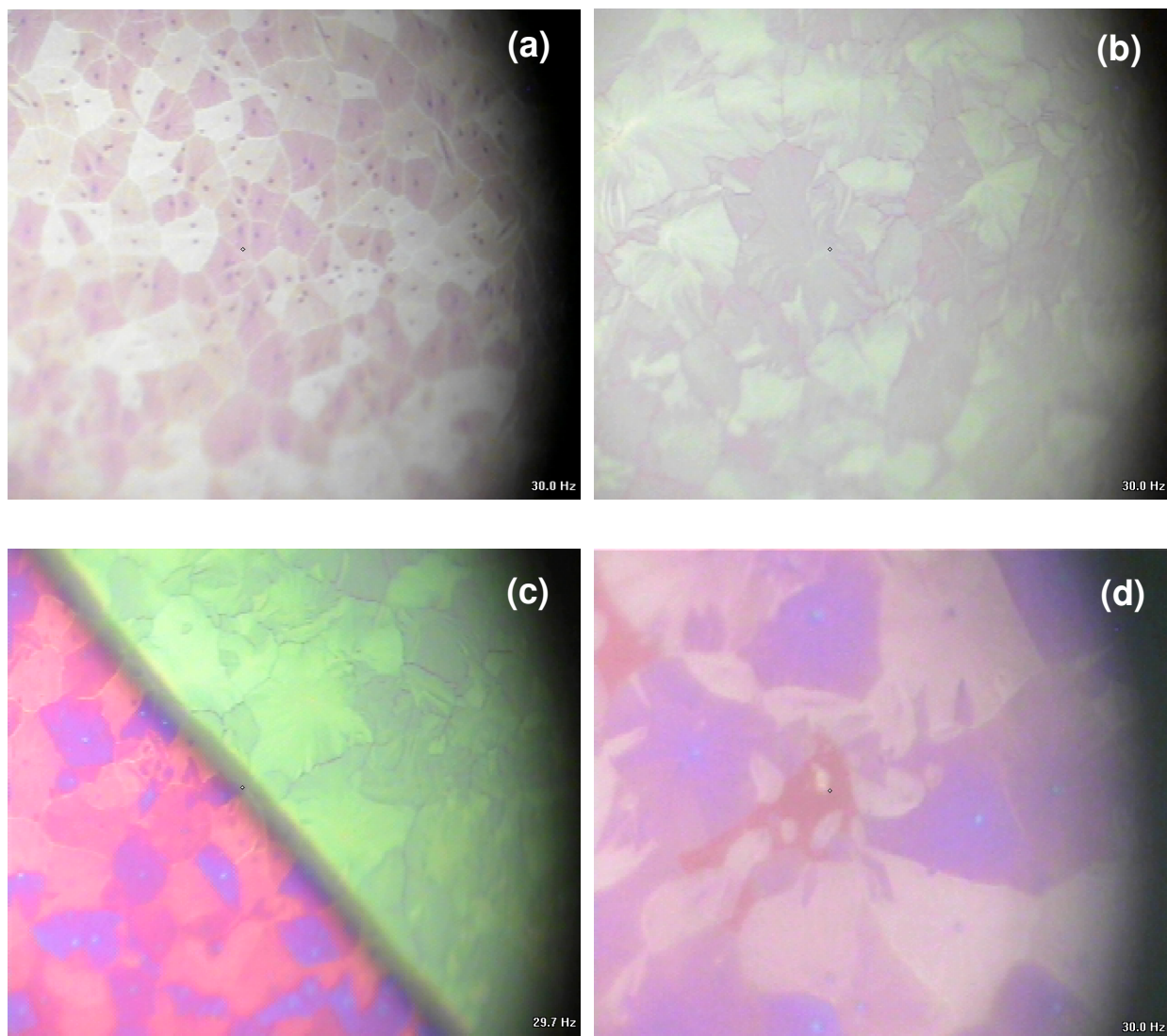


**Figure 4.11.** FeP<sub>2</sub> films made by annealing FeP<sub>3</sub> films 8 hr at 115 °C as seen through the Raman microscope. Grain sizes are typically smaller for films deposited atop Al/LiF electrodes (*a*) vs. the bare Si substrate (*b*). Grains appear to make a continuous transition between the two topographies when deposited across the interface between the two surfaces (*c*). In some cases, regions of unconverted FeP<sub>3</sub> remained between grains (*d*). The images in panels *a*, *b*, and *c* have dimensions of ca. 100 x 100 μm<sup>2</sup>. Panel *d* is at twice the magnification. All images come from different samples, though *c* and *d* were made in the same deposition.

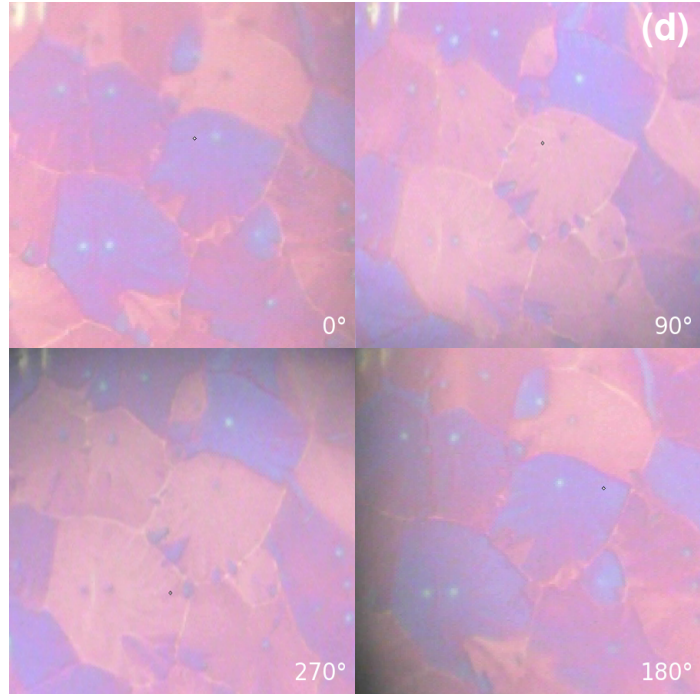
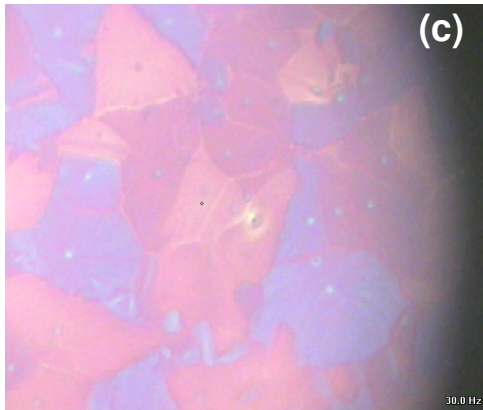
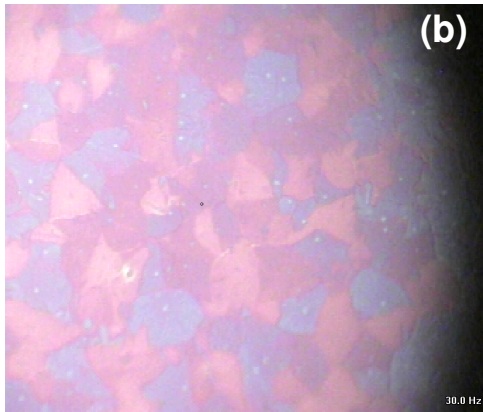
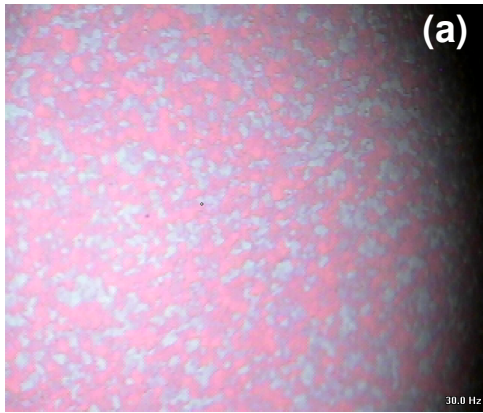


**Figure 4.12.** An FeP<sub>2</sub> film on Si/Al/LiF made by annealing an FeP<sub>3</sub> film in vacuum 8 hr at 115 °C viewed through the Raman microscope at three different magnifications with areas of ca. 500 x 500  $\mu\text{m}^2$  (a), 100 x 100  $\mu\text{m}^2$  (b), and 50 x 50  $\mu\text{m}^2$  (c). When the sample is rotated in-plane about the surface normal grains transition between light and dark contrast (d). The images in panel d have been rotated to maintain the presented orientation of the grains in each image.

of each nucleation site. Termination of grain growth by intersection of neighboring grains would produce tears or fissures at their boundaries, where the grains would compete for remaining FeP<sub>3</sub>. This might explain the deep grain boundaries observed in the AFM images. In addition, the direction of strain within each growing grain might cause the striations that radiate from the center on the surface of the grains.

Perhaps the most striking feature of the reflected light optical microscopy images is the contrast between grains. One must be careful when drawing conclusions based on the colors in such images because the observed color is dependent on the reflection from the film surface, transmission through the film and subsequent reflection from the substrate, the film thickness, the angle of illumination and observation, the spectrum of the illumination source, any wavelength-dependent sensitivity of the CCD detector, and post-collection image optimization performed automatically by the imaging software.

To begin an analysis of the grain coloring, it is necessary to look first to the substrate surface. The Si wafers employed here have a roughly 600 nm thick artificially grown oxide layer at the surface. Diffraction from the oxide layer coupled with absorption in the visible spectrum from the underlying Si gives these wafers a dim green color when viewed through the Raman's microscope where the angle of illumination and observation are constant. On the other hand, the rough, highly reflective surface of vapor-deposited metal films such as Al appears as bright white. Thin coatings of LiF laid over the Al films do not change the appearance.

When an FeP<sub>2</sub> film is formed across these surfaces, such as with the samples presented in Figure 4.11, the color of the film grains depends on the combination of the optical qualities of the film and of those of the underlying surface. Grains that sit directly atop the Si wafer vary in shades

of light and dark green while grains formed over the top of the Al/LiF are brighter and vary from pink to blue. The boundaries between the grains are typically dark for films on Si and light for those on the metal surface. That the grain boundaries take on the reflective qualities of the underlying materials suggests that the film within the boundaries is very thin or even absent.

The observed variation in grain color could result from a variation in the thickness of grains and interference of light reflected off of the underlying substrate and through the film. However, this possibility is immediately ruled out since no such variation in grain thicknesses was observed in the AFM scans. Instead, the colors of the grains are directly related to the orientation of the sample on the microscope stage. As shown in Figure 4.12 (animation in Supplementary File S3), rotation of the sample  $90^\circ$  about the surface normal inverts the contrast in the captured image. For film grains grown atop Al/LiF, blue grains turn pink, and vice versa, from this rotation. Another  $90^\circ$  rotation restores the original contrast, and so on. This behavior strongly resembles pleochroism, a property of crystals of many minerals whereby the wavelength-dependent transmission through the crystals, and therefore their color, depends on the orientation of the plane of the transmitted light relative to the crystallographic axes. The crystal system for FeP<sub>2</sub> is orthorhombic, a biaxial system.<sup>74</sup> Such a system is capable, in principle, of exhibiting trichroic coloring, wherein up to three colors of transmitted light may be seen through the crystal depending on which crystal face is presented. Additionally, a single face of a pleochroic crystal may appear one of two colors if the incident light is polarized, i.e. one color is observed when the plane of the light is oriented parallel to some crystal axis and another is observed when the plane of the light is oriented perpendicular. Thus, rotation of a pleochroic crystal  $90^\circ$  under polarized illumination will alternate the appearance

between the two possible colors. At intermediate rotation angles, the observed color will be a blend of the two extremes.

No reports exist of pleochroism in FeP<sub>2</sub> crystals or films. This is not surprising, given the difficulty in growing large FeP<sub>2</sub> crystals. It is troubling, however, that there is no known source of polarization in the Raman microscope. However, the same effect was seen within the microscope of the AFM. The resemblance to pleochroism is strong, but without identifying a polarizer in the setup, the phenomenon cannot be confirmed absolutely. Whether pleochroism or some other phenomenon, only an ordered film is expected to exhibit orientation-dependent coloring.

The existence of order within the FeP<sub>2</sub> films is also evidenced by the powder XRD pattern, as seen in Figure 4.13. Three sharp peaks are observed in the region from 5 to 35° 2 $\theta$ . These reflections occur as well in the pattern measured of the FeP<sub>2</sub> powder which itself was found to be in absolute agreement with a pattern calculated from the single crystal structure of Gallois et al.<sup>74</sup> The calculated pattern allows the FeP<sub>2</sub> powder pattern to be indexed unambiguously. The three reflections from the FeP<sub>2</sub> film are found to lie in the same positions as the (002), (004), and (006) reflections of the FeP<sub>2</sub> powder.

Because of the Bragg-Brentano geometry of the diffractometer, only Miller planes parallel to the substrate surface will reflect the incident x-ray to the detector. In a powder sample, crystalline grains are randomly oriented, every set of Miller planes is equally likely to be in the necessary orientation, and all predicted reflections are observed. If a single crystal were to be analyzed in the diffractometer, only a single family of Miller planes would be parallel to the surface of the sample holder and produce peaks in the pattern.

These are the two limiting cases for crystalline samples and the FeP<sub>2</sub> film behaves as would

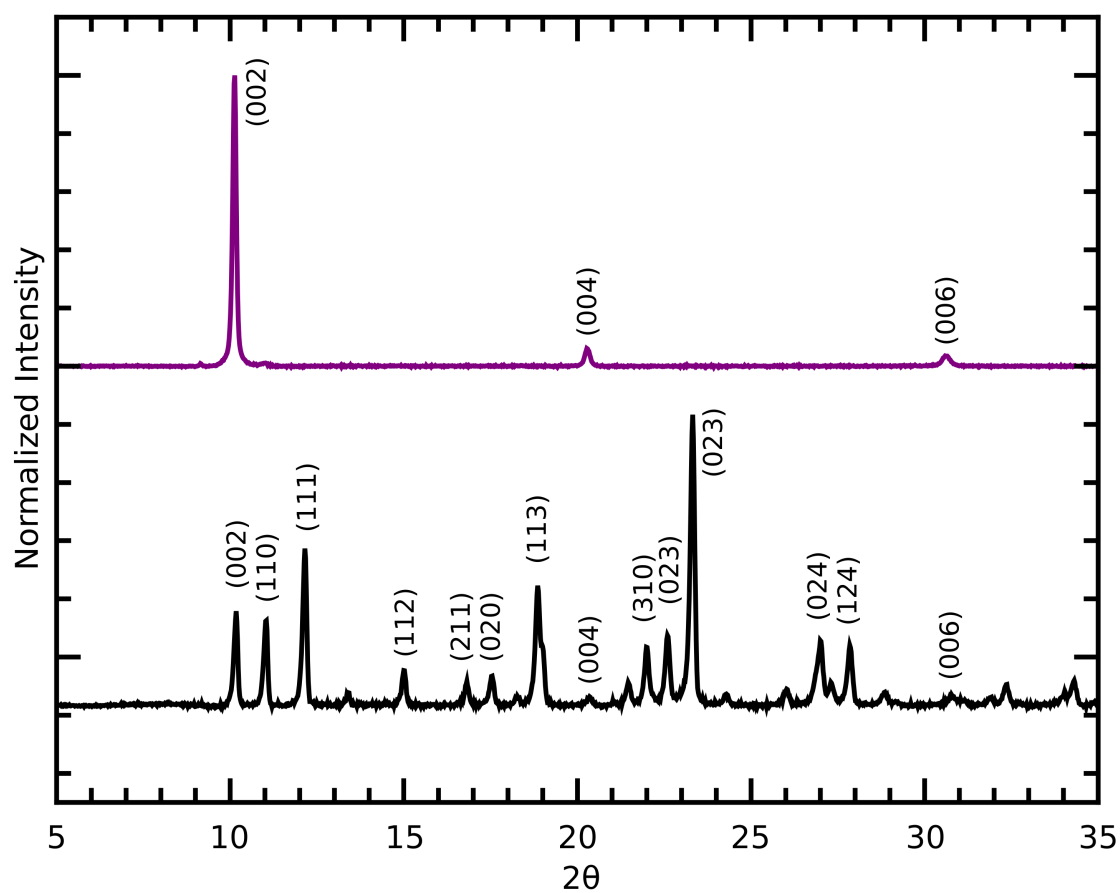


**Figure 4.13.** X-ray diffraction (Cu K $\alpha$ ) spectrum of a ~100 nm FeP<sub>2</sub> film on glass made by annealing an FeP<sub>3</sub> film (top) compared to that of FeP<sub>2</sub> powder (bottom). The spectra were indexed by comparison to the calculated pattern from the single crystal structure in Ref. 74.

a single crystal. However, there is an intermediate case: the crystalline grains of the sample may indeed have only one family of planes parallel to the surface but also have random rotations about the surface normal, such that other planes vary in orientation with respect to the incident x-ray. This phenomenon is called texturing and shown diagrammatically in Figure 4.14. Because the dynamically oriented planes that are not parallel to the surface will go undetected, the spectrum of a textured sample will be the same as that of a single crystalline sample.

The (002), (004), and (006) planes of FeP2 are all orthogonal to the  $c$ -axis of the crystal and parallel with the plane defined by the  $a$ - and  $b$ -axes (Figure 4.15). As a member of the orthorhombic crystal system, where the angles between the  $a$ ,  $b$ , and  $c$ -axes are  $90^\circ$ , it must be the case that the crystalline regions within the FeP2 film are oriented with their  $c$ -axes normal to the surface.

Powder x-ray diffraction is a bulk measurement and care must be exercised in making any further conclusions. It cannot be proved from this simple measurement whether the grains observed under the microscope and within the AFM images are entirely crystalline. For example, the possibility remains that the grains are only crystalline at their surface. Nor can it be said for certain whether the FeP2 films are single crystalline or textured. The latter seems most likely however and the random orientation of the crystallites around the  $c$ -axis is probably related to the orientation dependent coloring of the film grains as observed through the optical microscope.

#### **4.5 Magnetometry and Spin-Crossover of Fe(phen)<sub>2</sub>(SCN)<sub>2</sub> Films**

The physical property most directly altered by the change from the  $^1A_1$  electronic state to the  $^5T_2$  state in mononuclear  $d^6$  metal complexes is the change in magnetic properties, i.e. spin

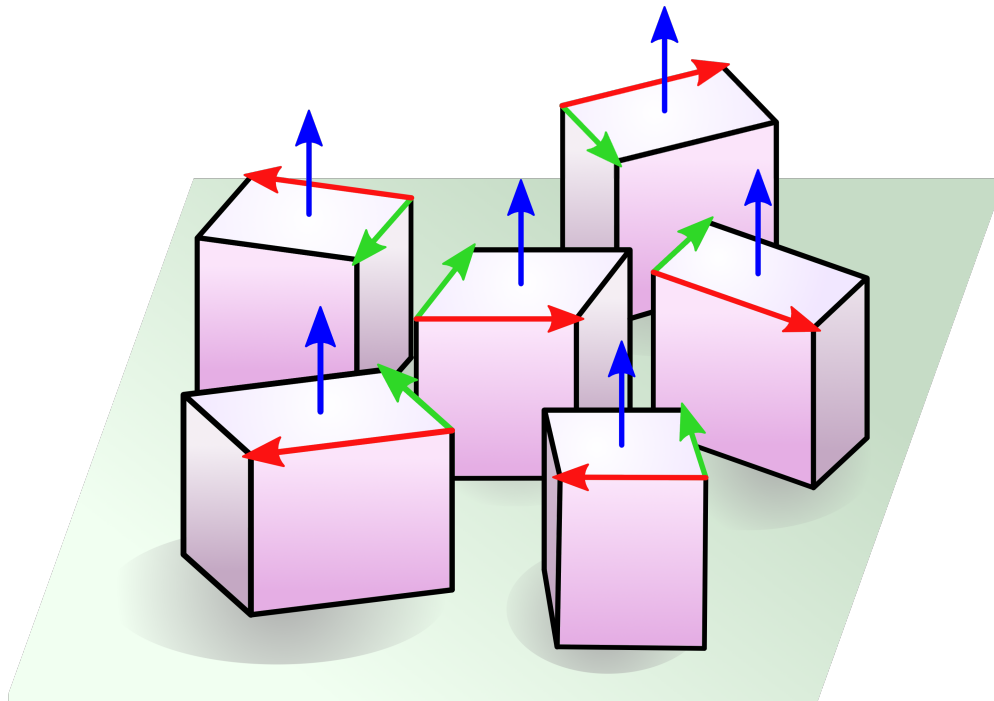


**Figure 4.14.** Diagram of crystalline domains in a textured film. Crystallites may have any orientation made by rotation about the surface normal but one family of planes, here those parallel to the plane made by the red and green axes, is always parallel to the surface.

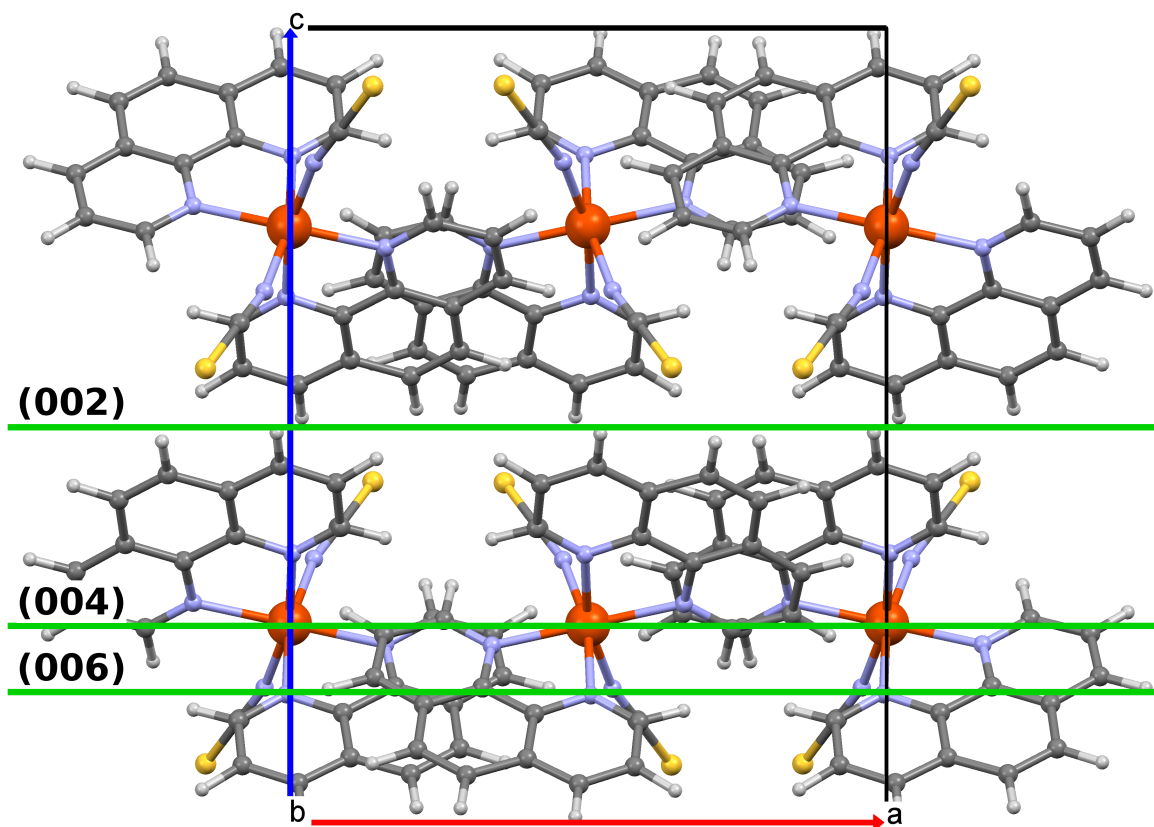


**Figure 4.15.** The view down the  $b$ -axis of the crystal structure of FeP2. The green lines are the (002), (004), and (006) planes, that lie parallel to the  $a$ - $b$ -plane and orthogonal to the  $c$ -axis, seen from the edge. The structure comes from Ref. 74.

state, of the molecule. When in the LS  $^1A_1$  ground state, all six d-electrons are paired, the total magnetic moment is nearly zero, and the material is largely diamagnetic. The magnitude of the spin-only magnetic moment for the molecule is given (in Bohr magnetons) by

$$\mu_S = g \mu_B (S(S+1))^{1/2} \quad (4.1)$$

where  $g$  is the electron  $g$ -factor ( $\sim 2$ ),  $\mu_B$  is a Bohr magneton, and  $S$  is the total spin of the system. Upon switching to the HS  $^5T_2$  ground state, two d-electrons are promoted to the  $e_{2g}$  orbitals giving rise to four unpaired spins and paramagnetism. For a total spin of  $S = 2$ , the spin-only magnetic moment is expected to be about  $5 \mu_B$ . In reality, the measured magnetic moment of an octahedral Fe(II) ion will be slightly higher because of spin-orbit coupling.

For FeP2 in which little to no mixing of high and low spin states occurs at temperatures far from the spin transition temperature, the effective magnetic moment has been reported as  $\mu_{\text{eff}} = \sim 5.2$  and  $\sim 0.2 \mu_B$  for the high and low spin states, respectively.<sup>80</sup> Such highly homogeneous spin compositions occur in strongly cooperative SCO materials and are highly dependent on crystal lattice effects. As the quantity of defect sites increases, the spin transition becomes broader with respect to the temperature range over which mixed compositions are found to the limit that at very low/high temperatures some portion of the molecules remain trapped in the high/low spin state.<sup>80</sup> This effect has important implications for spin crossover materials that would be milled and for devices produced at the nanoscale where the fraction of surface sites becomes significant or even dominant. In these cases, hysteresis widths shrink or disappear, effects associated with the SCO are less severe and more gradual, and the mixed spin states can give rise to ambiguity in the otherwise binary state of the material.<sup>34,124</sup>

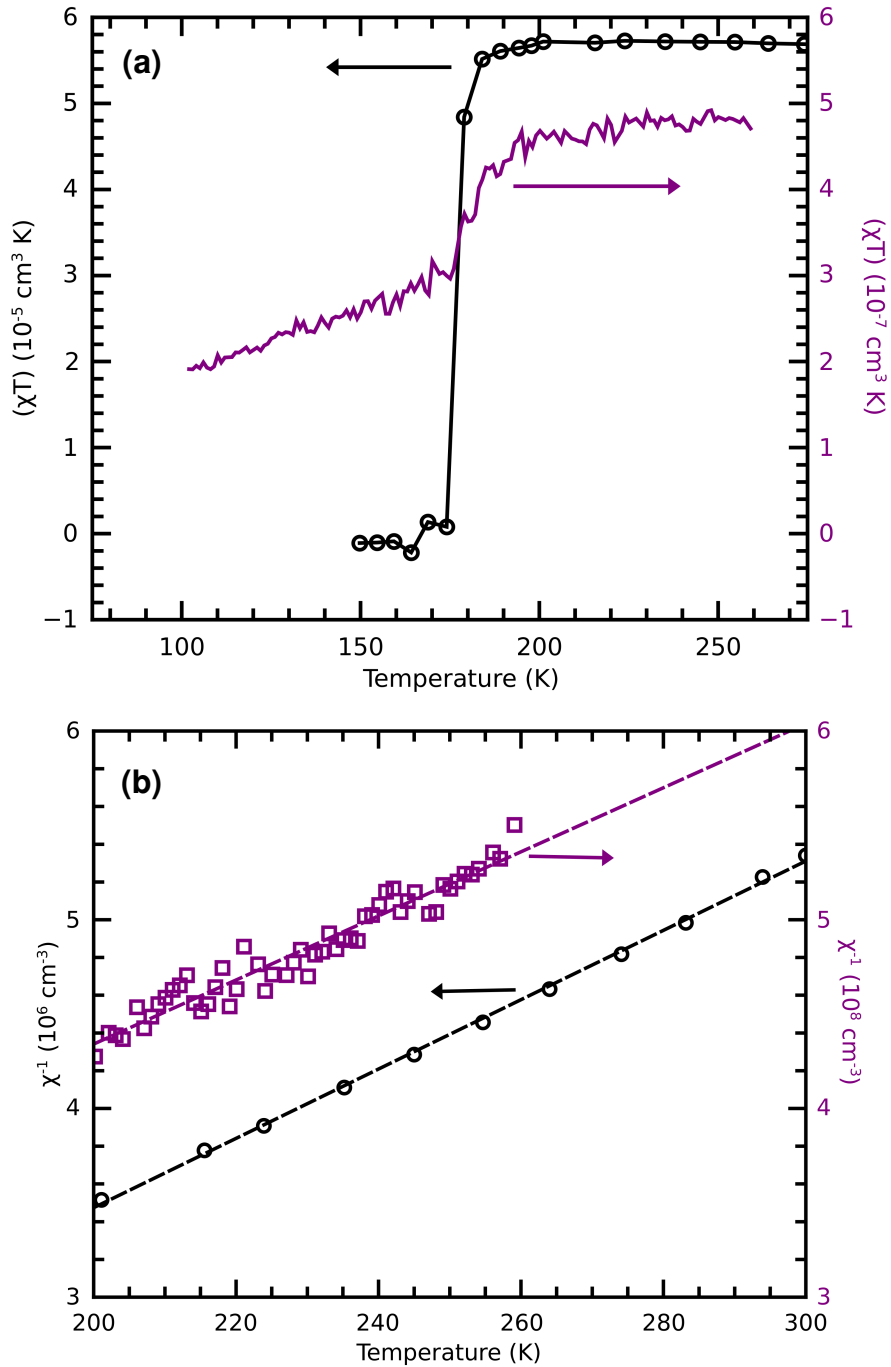


**Fig 4.16.** The magnetic susceptibility product ( $\chi T$ ) measured by SQUID magnetometry (a) of an FeP2 film on Si collected at 0.5 T (solid, purple line) compared to that of roughly 10 mg of FeP2 powder collected at 0.1 T (black line with circles). The inverse of the magnetic susceptibility (b) is linear (dashed lines) with respect to temperature above 200 K for both the film (purple squares) and the powder (black circles).

In the case of FeP2 specifically, the simplest synthetic routes give rise to low quality crystalline powders that were historically thought to represent a polymorph different from that of the higher quality material produced by solvent extraction (see Chapter 2) based on differences in the magnetic behaviors of the materials.<sup>74</sup> It was eventually proven that the crystal structures of the two suspected polymorphs are in fact isostructural and the differences in magnetic behavior coincided with crystalline quality and defects.<sup>80,108</sup>

Figure 4.16 shows the temperature dependence of the magnetic susceptibility product ( $\chi T$ ) and effective magnetic moment for a  $10 \pm 2$  mg powder sample of FeP2 synthesized by thermal decomposition from FeP3 and of an FeP2 film, as measured by SQUID magnetometer. The SQUID magnetometer measures the magnetization of a sample directly and the magnetic susceptibility product is found by the relationship

$$(\chi T) = (M / H) T \quad (4.2)$$

where  $\chi$  is the magnetic susceptibility ( $\text{cm}^3$ ),  $T$  is the temperature (K),  $M$  is the measured magnetization (emu), and  $H$  is the applied field (Oe). Whereas the magnetization and magnetic susceptibility depend on temperature, the magnetic susceptibility product has no inherent temperature dependence, is related simply to the number of moles in the material measured,  $n_{\text{moles}}$ , and the effective magnetic moment in Bohr magnetons, and is a more useful metric.

$$(\chi T) = 0.125 \mu_{\text{eff}}^2 n_{\text{moles}} \quad (4.3)$$

It is more common to report the molar magnetic susceptibility product, ( $\chi_{\text{M}} T$ ), which can be derived by taking the magnetic susceptibility product over  $n_{\text{moles}}$ .

$$(\chi_{\text{M}} T) = (\chi T) / n_{\text{moles}} \quad (4.4)$$

$(\chi_M T)$  is not reported here because the amount of material in the film is known only crudely, i.e. the film thickness was not measured. The molar magnetic susceptibility product will be an intrinsic property of a given material but  $(\chi T)$  is proportional to the mass of the material. In this case,  $(\chi T)_{\text{FILM}}$  approaches  $5 \times 10^{-7} \text{ cm}^3 \cdot \text{K}$  at high temperature. Combining Equations 4.3 and 4.4, and assuming the effective magnetic moment of FeP2 is  $5.2 \mu_B$  at temperatures far above the spin transition, it is possible to estimate  $n_{\text{moles}}$  for the film. Then using the molar mass of FeP2 (532 g/mol), its density<sup>74</sup> (1.512 g/mol), and the dimensions of the sample substrate ( $6 \times 6 \text{ mm}^2$ ) one can derive an approximate thickness for the film which is found to be *ca.*  $1.4 \mu\text{m}$ . The derived thickness is a bit more than the expected thickness based on the QCM readout but is not unreasonable, especially given the approximations made.

The powder shows behavior typical for good quality FeP2, i.e. highly crystalline or polycrystalline material with few defects. At high temperatures the susceptibility product is constant. When the temperature is lowered through the spin transition,  $(\chi T)_{\text{POWDER}}$  is seen to drop suddenly to a near zero value over a very narrow span of temperature. The transition temperature determined by taking the first derivative of the  $(\chi T)_{\text{POWDER}}$  plot is determined to be 178 K. Typically, the transition temperature for FeP2 is reported closer to 175 K but varies somewhat in the literature where myriad syntheses, sample treatments, and measurement techniques are employed. The sampling in this region was done only every 5 K, so the determined value should be considered approximate.

The general behavior of the FeP2 film is similar in that  $(\chi T)_{\text{FILM}}$  starts high at high temperature and shows a sudden decline when the sample is cooled. Unlike the powder, the main transition in the film appears to occur over a temperature range of at least 20 K. Taking the

derivative once again, the inflection point occurs near 180 K. The drop-off this time is not as severe relative to the magnitude of  $(\chi T)_{\text{FILM}}$ . Further cooling shows  $(\chi T)_{\text{FILM}}$  steadily declining instead of leveling near zero. This continued slow decline indicates material that did not transition to the  $^5T_2$  ground state in the main transition but that requires lower temperatures to switch. The decline is gradual, indicating poor communication and cooperativity between this second class of material in the film.

The observed value of  $(\chi T)$  will depend on the fraction of the material that is in a HS state,  $\gamma_{\text{HS}}$ , and the amount in a LS state,  $1 - \gamma_{\text{HS}}$ .

$$(\chi T) = (1 - \gamma_{\text{HS}}) (\chi T)_{\text{LS}} + \gamma_{\text{HS}} (\chi T)_{\text{HS}} \quad (4.5)$$

The contribution from the LS material is small enough to be safely ignored and Equation 4.5 can be simplified.

$$\gamma_{\text{HS}} = (\chi T) / (\chi T)_{\text{HS}} \quad -4.6$$

As before, the magnetic susceptibility product will be assumed to reach a maximum value of roughly  $5 \times 10^{-7} \text{ cm}^3 \cdot \text{K}$ . Near 100 K, the observed  $(\chi T)$  is about  $1.9 \times 10^{-7} \text{ cm}^3 \cdot \text{K}$ . The calculated fraction of molecules still in a HS state at 100 K is then about 38 %. A significant portion of the film remains un-switched even at 100 K. As discussed above, a residual HS fraction at low temperature is to be expected for material which suffers from poor communication between molecules and clusters of molecules or in which molecular environments hinder switching. Given the topography of the films revealed by AFM and optical microscopy, it should come as no surprise that communication across the film is ineffectual. The film grains are at best considered as small, independent nanoparticles laid in a single layer across the substrate surface. Residual, un-switched

material above and below the spin transition and the broadened transition temperature range are common occurrences for SCO materials prepared on the nanoscale, where the nature of surface domains becomes increasingly important.<sup>32,33,41,125-127</sup> When considering thin films specifically, the SCO behavior of films deviates from the behavior of bulk powder materials and may disappear altogether in the extreme thickness limit of only a few molecular layers.<sup>50,51</sup>

Other explanations have been offered for the higher than expected magnetic moment below the spin transition temperature. Often ignored is the kinetic behavior of the SCO phenomenon and it has been suggested that samples which show incomplete transitions were measured out of equilibrium.<sup>128</sup> Some regions of material that are kinetically slow to transition, may remain HS below the spin transition temperature if sufficient time is not allowed between measured data points.<sup>129</sup> It has been shown that the rate of transition depends strongly on the crystallite size such that ground powders and powders produced by rapid precipitation transition more slowly than single crystalline samples.<sup>130</sup> In addition, the perception of residual HS or LS material that relies on the comparison of  $(\chi_M T)$  at high and low temperature may suffer from deviation from ideal Curie-Weiss behavior.<sup>128</sup> And in most cases, the high temperature maximum of  $(\chi_M T)$  is not established definitively.

Panel (b) of Figure 4.16 shows the inverse magnetic susceptibility,  $\chi^{-1}$ , plotted as a function of temperature for both samples. Above 200 K, the plotted data are found to be linear. This behavior represents a Curie-Weiss temperature dependence of the magnetic susceptibility and is a hallmark of paramagnetic materials. The slope in each case is nearly the same only being smaller by a factor of  $10^2$  in the case of the film. The change of magnitude can be accounted for by the difference in mass between the two samples.

#### 4.6 Films Deposited onto Hot Substrates

It stands to reason that if FeP3 molecules can be decomposed by heat to yield FeP2 molecules, as is the case during synthesis of FeP2 by thermal decomposition of FeP3 and in the conversion of FeP3 films to FeP2, then free FeP3 molecules impacting a hot surface might pyrolyze immediately on contact. In the suggested scenario, free FeP3 molecules are produced during vapor deposition from FeP2 and thermally decompose to yield FeP2 as they physisorb to and migrate across the hot substrate surface. Since the FeP2 molecules are formed while still mobile, they would have the chance to settle into crevice-free, smooth, amorphous films. No subsequent post-deposition heating for conversion from FeP3 would be necessary.

By mounting Si substrates to a copper block heated internally from a cartridge heater, the temperature of the substrates can be controlled and monitored from a thermocouple pinned to the surface of a sample. Figure 4.17 shows the transmission FT-IR spectra from films deposited from FeP2 onto  $1 \times 1 \text{ cm}^2$  Si substrates ( $\sim 600 \text{ nm}$  artificial surface oxide). The spectra shown are limited to the area near  $2100 \text{ cm}^{-1}$  where the N-CS stretching modes are found. The lower energy regions are omitted because they are of little diagnostic value and because of strong artificial effects from SiO<sub>2</sub> background subtraction. At the lowest substrate temperature,  $105 \text{ }^\circ\text{C}$ , there is a broad peak whose maximum is found at  $2056 \text{ cm}^{-1}$ . The peak position lies between that expected for FeP3,  $2050 \text{ cm}^{-1}$  and that for FeP2,  $2072/2060 \text{ cm}^{-1}$ . A mixture of these two species in the film might give rise to a broad peak at this position.

A few weak shoulders appear on the high energy side of this peak whose intensities increase as the substrate temperature increases. The shoulders occur at energies higher than those expected

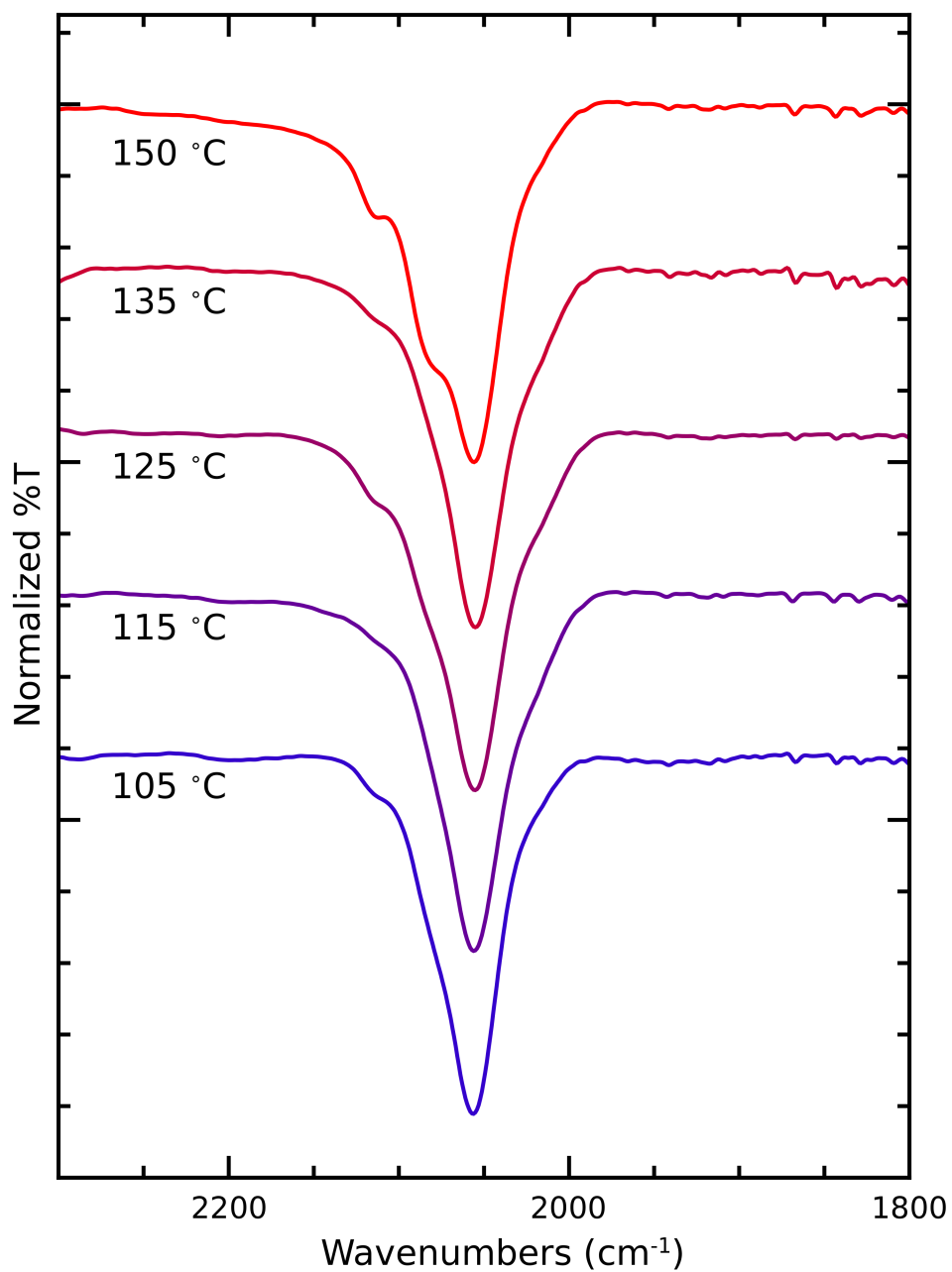


**Figure 4.17.** Transmission FT-IR in the region of the N-CS stretching modes of films deposited from FeP2 onto Si substrates held at different temperatures.

for the FeP2 doublet. Therefore, a third species is implied. Deconvolution of the components of this peak would be speculative. However the shoulder most removed from the main body of the peak appears to lie near  $2114\text{ cm}^{-1}$ . In a previous section of this chapter, a doublet at  $2114/2094\text{ cm}^{-1}$  was found to occur in FeP3 films that were annealed post-deposition at high temperatures (Figure 4.2) and was tentatively assigned to the asymmetric and symmetric N-CS modes of FeP1. Thus, it appears likely that the films deposited onto hot substrates here also contain this species.

That this third species increases in concentration with temperature correlates well to the species detected in Figure 4.2 and assigned as FeP1. Interestingly, when films are deposited onto room temperature substrates and annealed post-deposition, the presence of this species isn't detected until a temperature of  $135\text{ }^{\circ}\text{C}$ . But when substrates are heated during the deposition, this species seems to be present at substrate temperatures as low as  $105\text{ }^{\circ}\text{C}$ . Additionally, post-deposition annealed films can be converted from FeP3, to FeP2, to the third species in succession. With careful temperature control, it is possible to isolate pure films of any of the three species. That is not the case here, where a mixture of species always occurs.

The Raman spectra of films deposited onto hot substrates shown in Figure 4.18 gives a somewhat different picture. For all substrate temperatures, the spectra resemble that of FeP3. However, each also contains weak signals near  $282, 420, 1422, \text{ and } 2072\text{ cm}^{-1}$ , each of which is associated with FeP2 but not FeP3. A third species is not detected. Nonetheless, the FT-IR and Raman spectra can be reconciled by considering that the cross-sections for FT-IR absorption and Raman scattering may be different for each material. Recall that both FeP3 and FeP2 absorb near the wavelength of the Raman laser,  $632.8\text{ nm}$ . If FeP1 absorbs near  $440\text{ nm}$  as suggested by Lee et

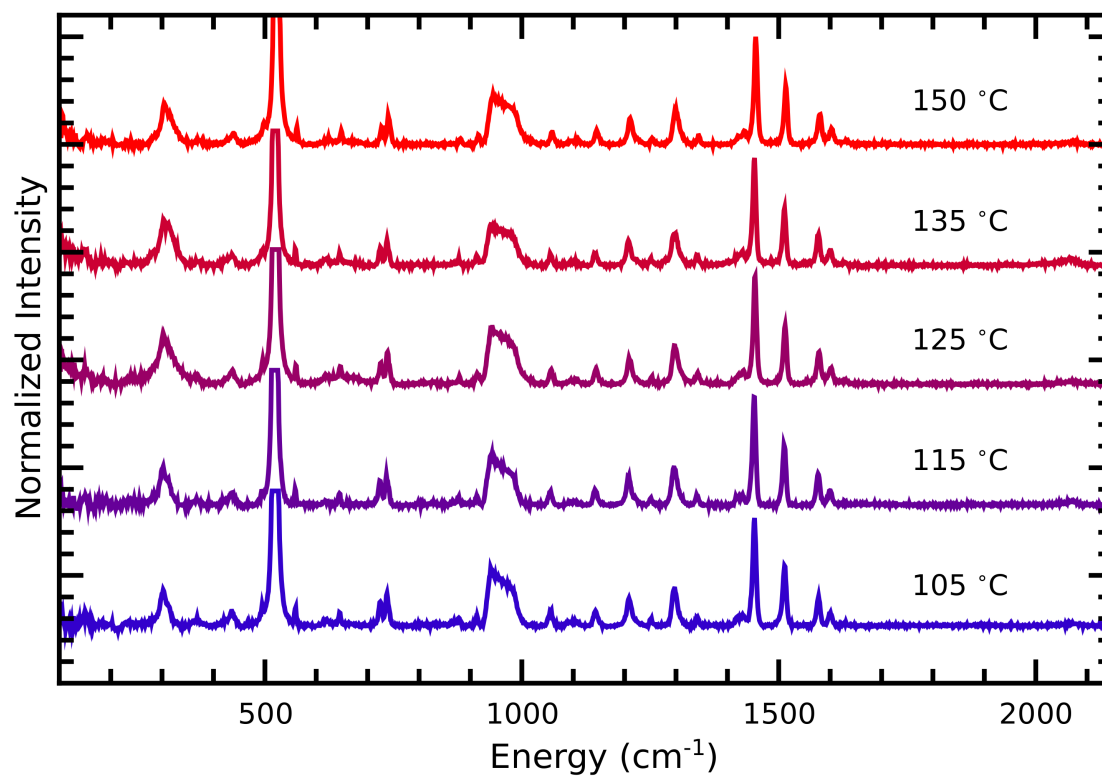


**Figure 4.18.** Raman spectra of films deposited from FeP2 onto Si substrates held at different temperatures. The tall features near 520 and 950 cm<sup>-1</sup> are due to the substrate.

al. the Raman scattering cross-section would be reduced.<sup>106</sup> The Raman intensity should also be less in FeP2 and FeP1 because of the reduction in chromophores (phen ligands).

Whatever the the reason, it is clear from the vibrational spectra presented that films grown on hot substrates are a mixture of at least two species, probably three. No final substrate temperature was identified that would result in a purely FeP2 film. The surfaces of these films were found to be very smooth, which was one of the objectives of this experiment, but this may be a feature of FeP3 on the film surface. This approach was not investigated further. Instead, all FeP2 films subsequently prepared were made by post-deposition annealing of FeP3 films, as described in the previous section.

#### **4.7 Summary**

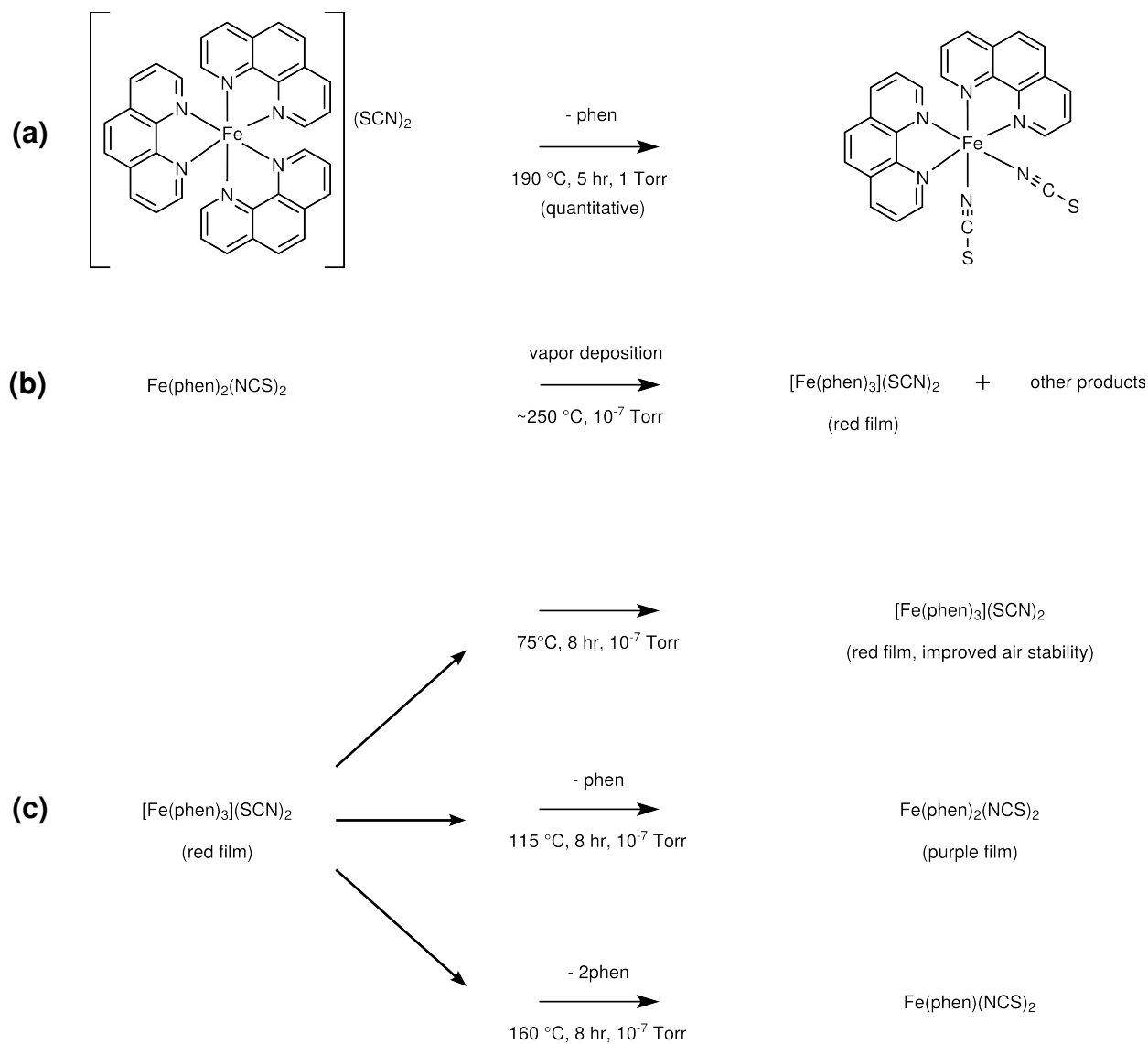
As described in Chapter 3, the preparation of films of FeP2 by vapor deposition of the bulk material has been reported previously but attempts to reproduce this result yielded films identified as FeP3.<sup>26</sup> Therefore, a modified procedure was developed based on observations of films deposited onto beakers covering the deposition boats. In the early stages of the first deposition from each batch of FeP2 powder produced from thermal decomposition of FeP3, a white film is deposited before the red FeP3 film deposits. If an initial sacrificial deposition is performed first to remove the source of the white film, subsequent depositions from the same material will deposit only smooth red FeP3 films. Alternately, the starting material can be produced via the direct aqueous synthesis technique described in Chapter 2. No further "cleaning" of FeP2 produced in this way is required.

Films of FeP2 can be obtained by heating the FeP3 films to moderate temperatures (*ca.* 115 °C) for extended periods of time (*ca.* 8 hrs). It is believed that conversion from FeP3 to FeP2

occurs by thermal decomposition of the FeP3 films in which a phen molecule is liberated from each FeP3 molecule. Coordination of the thiocyanate anions to the Fe<sup>2+</sup> center maintains the geometry as octahedral. The process is shown diagrammatically in Scheme 4.1. If lower annealing temperatures are used, films remain FeP3 but are less sensitive to air than films made with no post-deposition heat treatment. When heated to temperatures of 135 °C and greater, films of a third species are obtained. While not investigated in detail, vibrational spectroscopies suggest that the third material is FeP1 which is likely to form from FeP2 by another thermal decomposition step and release of another phen ligand. If confirmed, this would constitute the first report of FeP1 thin films.

FeP2 films made by the modified procedure show the same spectroscopic qualities as the bulk FeP2 powder. The maximum of visible absorption is shifted to lower energies relative to FeP3, a consequence of the change in ligand field. The paramagnetic state of the complex and reduced N(phen) : N(thiocyanate) ratio relative to FeP3 are evidenced by the x-ray photoelectron spectra. Typical films are comprised of grains 5 to 50 μm in size which is somewhat dependent on the choice of substrate. Deep fissures exist at the boundaries between the grains. Crystalline regions of the films are preferentially oriented with the *c*-axis aligned perpendicular to the substrate surface. The colors of the grains in the optical micrographs varied between two colors and changed with the rotation of the sample on the microscope stage. This suggests that the film is textured rather than single crystalline. These granular FeP2 films still exhibit SCO near the transition temperature of the bulk FeP2 powder but with reduced abruptness and completeness.

Attempts to produce FeP2 films directly during the vapor deposition step by depositing onto heated substrates produced films comprised of a mixture of species, probably FeP3, FeP2,



**Scheme 4.1.** Overview of preparation of FeP3, FeP2, and FeP1 films. Bulk FeP2 can be produced by pyrolysis of FeP3 (a) or precipitated directly from solution (see Chapter 2). Vapor deposition of the FeP2 yields films of FeP3 as discussed in Chapter 3 (b). The temperature during film deposition was not accurately controlled and may not represent the true temperature of the vaporized material (see Chapter 3). Post-deposition heat treatment of the FeP3 films yields films of one of three different materials, depending on the temperature employed (c). FeP3 films heated to mild temperatures remain FeP3 but have improved air stability. FeP3 films heated to moderate temperatures pyrolyze to FeP2 by loss of one phen ligand. FeP3 films heated to higher temperatures pyrolyze to FeP1 by loss of two phen ligands.

and FeP1. Only the post-deposition heating process described above was found to be successful in producing films of the target material. The technique developed is simple, reproducible, and requires unspecialized equipment. However, sufficient temperature control and time is required. Obtaining adequate temperature while heating substrates in vacuum is difficult because heat transfer is by conduction only; convection is not possible. Sample temperature is extremely dependent on the contact and pressure between the sample and heating surface. Within a single batch, some samples will typically show incomplete conversion to FeP2 because of poor heat transfer. Initial trials suggest that heating FeP3 films immediately after the deposition but outside of the vacuum chamber either in a controlled atmosphere or ambient air still effects conversion to FeP2 but with the benefits that heat transfer is more efficient and homogeneous, temperature control is more accurate, and annealing times are significantly reduced. Further refinement of the annealing process at normal pressures is suggested and may also effect the morphology of the FeP2 films which is important to device fabrication. Exploration of alternate heating treatments is outside the scope of this work and device fabrication and electrical characterization were performed on films prepared in vacuum, as described in the next chapter.

## CHAPTER 5

### ELECTRICAL MEASUREMENTS OF $[\text{Fe}(\text{phen})_3](\text{SCN})_2$ AND $\text{Fe}(\text{phen})_2(\text{NCS})_2$ FILMS

#### 5.1 Device Fabrication

Electrical characterization of thin films in a two terminal, diode-like configuration requires that electrodes be attached to opposite ends of a specimen of the material to be measured, charge injected from one or both of the electrodes by means of applying a bias, and transport of the charge through the material to generate a measurable current. The current-voltage, or I-V, characteristics generated are analyzed to understand the conduction properties of the material. Conversion of I to current density, J, and V to electric field, F, allows results to be expressed as J-F characteristics and to be compared between films of different thicknesses, d, and areas, A.

$$J = I / A \quad (5.1)$$

$$F = V / d \quad (5.2)$$

For measurement of thin films, by far the most common device geometry is one of vertical, or "sandwich", junctions (Figure 5.1 (a) and (b)). The bottom electrode, relevant films, and top electrodes are placed onto a flat substrate, one after another, to build the junction from the bottom up. Electrodes are usually placed by physical vapor deposition. Often, deposition of the top electrode may damage or penetrate the junction materials atop which it must lie. In these cases, the top electrode may be placed by a "softer" technique, such as contact with a hanging mercury drop

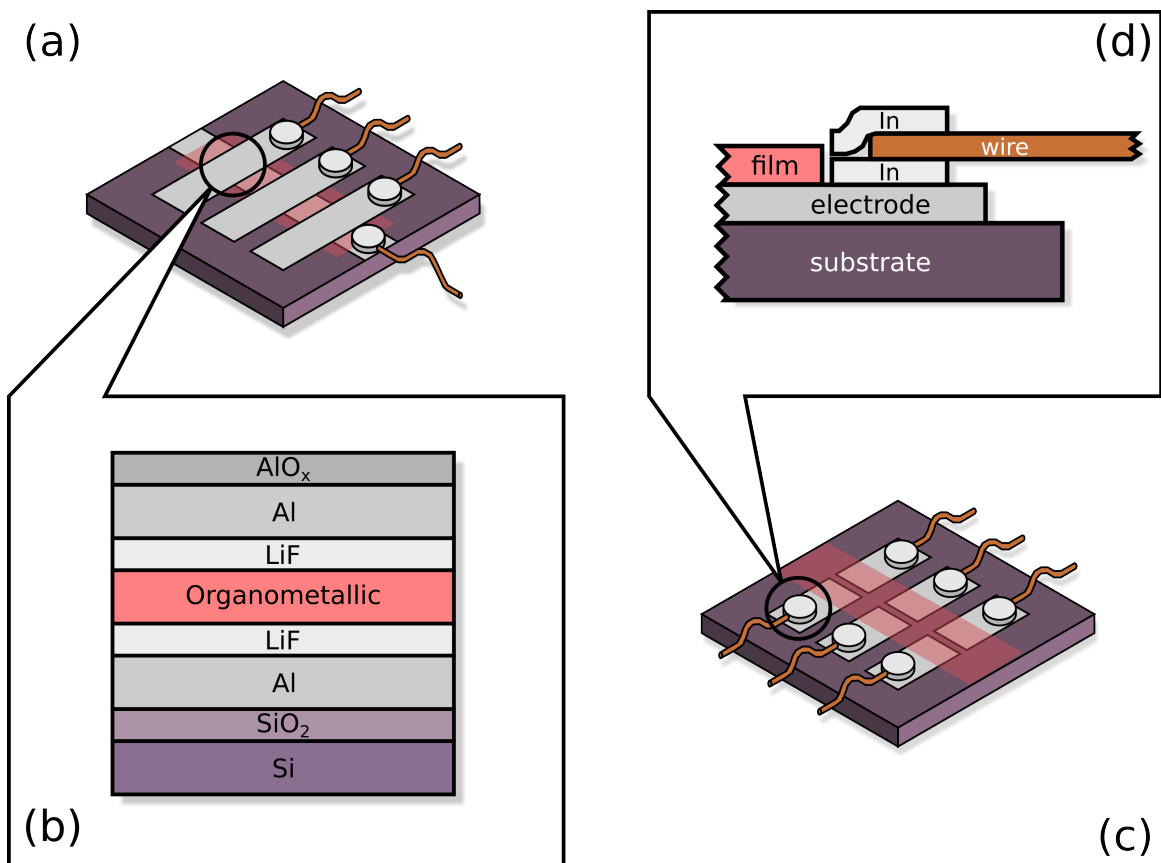


**Figure 5.1.** Structure of two device geometries, vertical/sandwich (*a*) and horizontal/bridge (*c*), used for electrical characterization. Inset (*b*) shows the layers of the sandwich structure for vertical devices. The ~600 nm SiO<sub>2</sub> layer is artificial. The AlO<sub>x</sub> layer is native and grows when deposited electrodes are exposed to air. Inset (*d*) shows how Cu wires were attached to metal electrodes by pressing the wires into soft In pads and capping them with another In pad.

or InGa eutectic.<sup>133,134</sup> The material under investigation is often deposited via physical vapor deposition as well, but where impossible or inappropriate for a material, it may also be placed by spin-coating, drop-casting, etc. Simple devices require only these components. More layers may be added to the "sandwich" in order to improve or modify the operation of the device. Commonly, these materials are electron/hole transport and blocking layers and thin films deposited at the interface of the electrodes and inner layers to improve charge injection/extraction.

An alternative geometry is the horizontal, or "bridge", junction (Figure 5.1 (d)). To make devices with these junctions closely spaced electrodes are first placed on substrate. The material in question is then placed across two electrodes, bridging them. Once again, physical vapor deposition is typically employed to place both the electrodes and the material under investigation. The advantage to this type of device geometry is that no top electrode need be deposited. The risk of shorting or damaging the specimen material is removed. Unfortunately, for organic semiconductors, whose mobilities are quite low, the separation distance between electrodes must be kept quite small (< 500 nm or so) which cannot be accomplished without some form of lithography. Otherwise, current through the device will be too low to measure without the use of sophisticated equipment and/or high electric fields.

In this work, the results presented all come from vertical-junction devices. Square  $1 \times 1 \text{ cm}^2$  Si wafers were used as substrates. These small wafers are cut from an ordinary 4-inch round wafer using a dicing saw. They are treated by the manufacturer to produce a ~600 nm oxide on their surfaces. The oxide layer provides necessary insulation from the p-doped silicon which is rather conductive compared to the materials under test. After the substrates were cleaned by ultrasonication and solvent rinsing, they were placed in the deposition chamber where three, 1 mm

wide bottom electrodes were deposited through a shadow mask to a thickness of ~40 nm. In some devices, a thin LiF layer was also deposited at this stage atop the Al bottom electrodes. Vacuum was then broken in order to load the sample material into the deposition boat. Once vacuum was restored, thin films of the sample material were deposited. Where FeP2 devices were desired, the FeP3 films grown at this step were then annealed, in situ, to convert them to FeP2. Finally, a third round of deposition was required to place a single top electrode, and optionally another interfacial LiF layer, perpendicular to the bottom electrodes. Three junctions were thus formed on each device. An example of a completed vertical junction is shown in Figure 5.1 (a). In order to connect the device electrodes with the terminals of the source meter, thin copper wires were pressed into small indium discs and onto the ends of the electrodes (Figure 5.1 (d)).

Care must be taken that the electrodes are not placed all the way to the edge of the Si wafer and that the indium contacts are not placed in this location either. The diced wafers have microscopic chips along their edges, likely caused by the dicing saw itself or handling of the wafers afterward (Figure 5.2). The chips are formed by loss of flakes from the surface where the oxide layer insulates the device from the conductive Si substrate. If electrodes come into electrical contact with these chips at the wafer's edge, shorts through the Si wafer will occur.

From bottom to top, devices made in this way are symmetric which means that charge conduction across the junctions should be the same regardless of the polarity of the bias applied. Conceivably, a small oxide layer develops atop the bottom Al electrode that would not be present on the underside of the top Al electrode. Yet, no significant polarity dependence is observed for any of the junctions shown here; J-F characteristics are symmetric about zero bias.

When device operation is begun, the potential difference across the devices forces charge

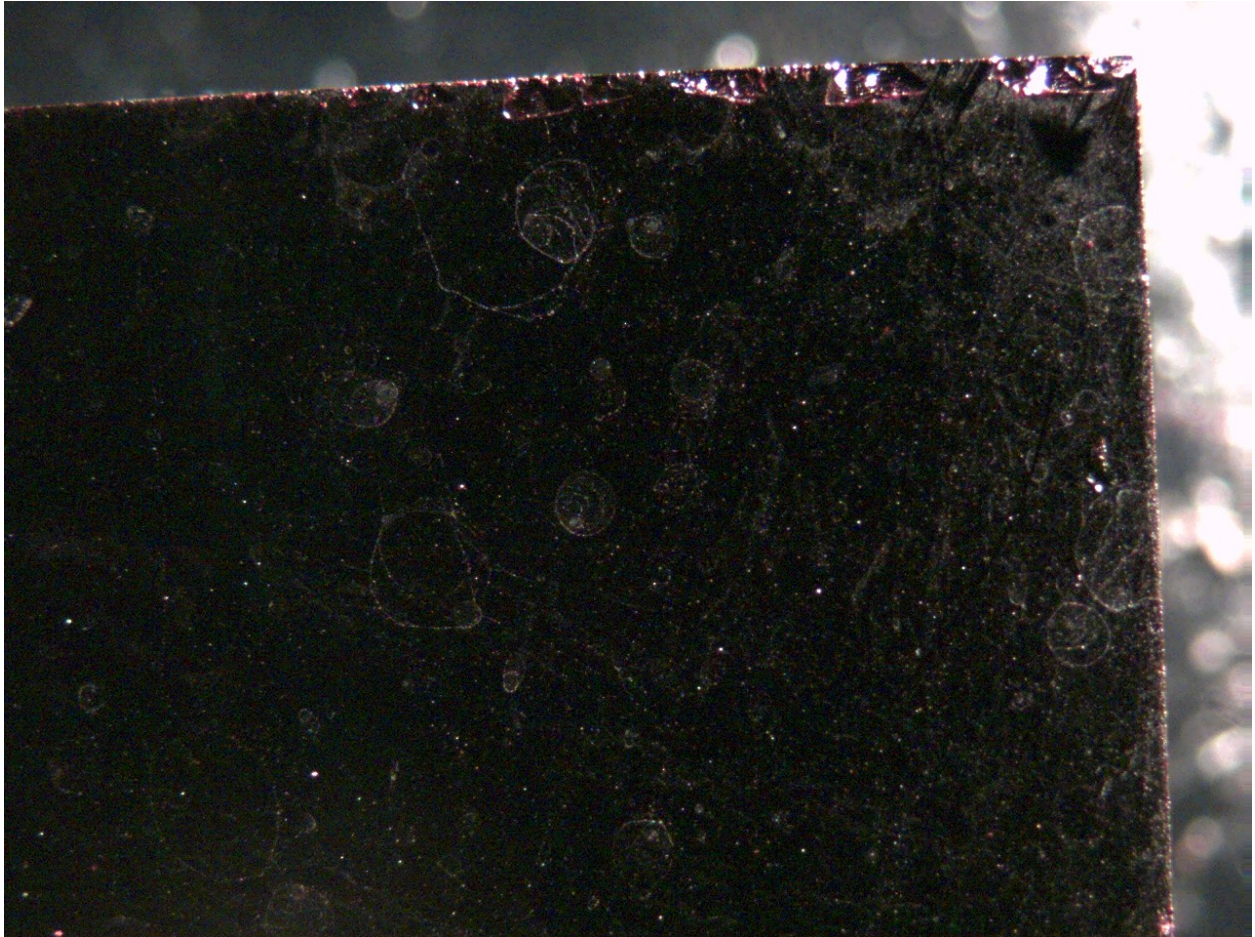


**Figure 5.2.** A photograph of the edges of a (used) Si wafer showing chips in the substrate that are probably a result of dicing or handling.

carriers to be injected into the junction from the electrodes. Within the metal electrodes, electrons exist at the Fermi level of the metal, determined by its work function. For organic materials, electrons are injected from the cathode into the LUMO's of the molecules at the interface. Similarly, holes are injected from the anode into the HOMO's. The energy differences between these frontier orbitals and the Fermi level of the electrode metal provide a barrier to charge carrier injection. In order for electron/hole injection to be efficient, the barrier must be small and the Fermi level of the metal close in energy to the LUMO/HOMO of the material. Junctions with small injection barriers are said to have Ohmic contacts. If the metal is the same for either electrode, its Fermi level cannot be close to both the LUMO and HOMO of the material simultaneously. Thus, symmetric devices will prefer only one type of charge carrier to be injected. Once carriers are injected into the material, they are transported across the material to the opposite electrode. A given material may efficiently transport only electrons, only holes, or both. The choice of metal for the electrodes of symmetric devices allows one to selectively measure the transport of the electrons and holes through the material in the junction, provided contacts are Ohmic.

In order to test the efficacy of device fabrication, trial devices were first made using Alq<sub>3</sub> as the organic semiconductor in the junctions. Three-junction devices were fabricated as in Figure 5.1 (a). Al was used for top and bottom electrodes and thin (0.5 - 1 nm) LiF layers were placed at the electrode interfaces. The Fermi level of Al, determined by its work function, lies near -4.2 eV from vacuum.<sup>135</sup> This is closer to the LUMO of Alq<sub>3</sub> than to the HOMO, as seen in Figure 5.3 (a), but the nominal electron injection barrier is still around 1 eV. Thin layers of LiF have been shown to improve injection efficiency from Al electrodes into organic semiconductors by modifying the energy levels at the interface and decreasing the effective injection barrier.<sup>136,137</sup> By matching the

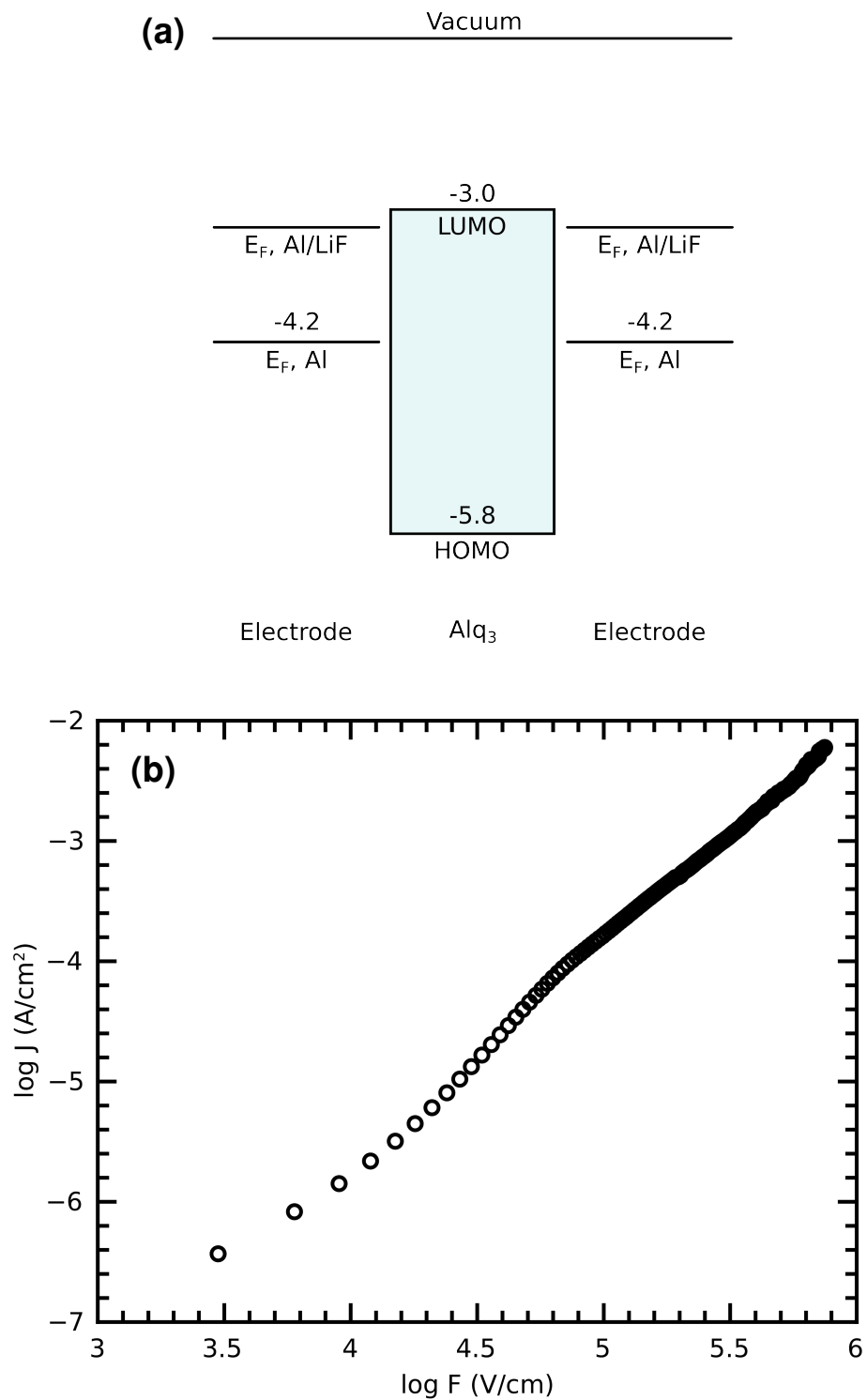


**Figure 5.3.** Energy level diagram for Alq<sub>3</sub> devices (a) and the J-F characteristic measured from one such device with a 134 nm Alq<sub>3</sub> film and Al/LiF electrodes (b).

Fermi level of the metal electrodes to the LUMO of Alq<sub>3</sub>, a so-called "electron-only" device is created. That is, the transport measured in these devices is that of electrons.

Figure 5.3 (b) shows the J-F characteristic from a trial Alq<sub>3</sub> device. Near the end of the plot, at high fields, the slope of the log-log plot approaches 2. This behavior is commonly seen in junctions made with organic semiconductors and with Ohmic contacts. The dependence of J on F<sup>2</sup> suggests that transport through the junction is limited by the accumulation of space charge at the interface of the injecting electrode and the sample material. That is, the device is operating with space-charge-limited current, SCLC. In an ideal device, with Ohmic contacts and no traps or defects, the SCLC represents the upper limit of conduction. In this regime, the rate of injection of charge carriers exceeds the rate at which they can be transported and extracted at the opposite end of the junction. The current in the device is therefore bulk-transport-limited, rather than injection limited. SCLC is described by the Mott-Gurney equation

$$I = 9/8 A \epsilon \epsilon_0 \mu V^2/d^3 \quad (5.3)$$

where A is the junction area,  $\epsilon$  is the dielectric constant of the material (typically  $\sim 3$  for organic semiconductors),  $\epsilon_0$  is the permittivity of vacuum, and  $\mu$  is the mobility of the charge carriers being transported.<sup>138</sup> The intrinsic property of the material obtained by application of this model is the mobility. For the electron-only device represented by Figure 5.3 (b), it is the electron mobility,  $\mu_e$ . By fitting the high field region of the curve on a double-log plot to a linear fit with a slope of 2,  $\mu_e$  is found to be  $\sim 5 \times 10^{-7} \text{ cm}^2/\text{V}\cdot\text{s}$ . Values for  $\mu_e$  reported in the literature range from  $1 \times 10^{-7}$  to  $1 \times 10^{-5} \text{ cm}^2/\text{V}\cdot\text{s}$  (the hole mobility,  $\mu_h$ , is two orders of magnitude lower).<sup>35,139,140</sup> In this discipline, reproducibility of device fabrication is difficult to obtain. Even analysis and interpretation of the

same I-V characteristics can vary between different persons or laboratories yielding a range of mobilities.<sup>141</sup> The electron mobility measured here for Alq<sub>3</sub> can be considered acceptable given the limitations of reproducibility of this technique. Attention can now be turned to devices incorporating films of FeP3 and the SCO material FeP2.

FeP3 and FeP2 devices were made in the same way as the Alq<sub>3</sub> devices, sometimes with and sometimes without LiF. To understand injection from Al and Al/LiF electrodes, it is helpful to know the positions of the frontier orbitals for these materials. The position of the HOMO of a material can be determined by UPS. Attempts to acquire an ultraviolet photoelectron spectrum of either material were not successful. Instead, XPS was used to measure the photoelectron spectrum in the valence band region near 0 BE (Figure 5.4). The XPS experiment requires considerably more effort (sampling time) and suffers from poorer resolution, but the spectra obtained are sufficient for identifying the HOMO energy. Accurate HOMO binding energies are obtained by measuring the onset of the first peak in the photoelectron spectrum.<sup>142</sup> The energy ascertained is relative to the Fermi level, i.e. the work function of the spectrometer.

Inverse photoemission spectroscopy (IPES) is best suited for determination of the LUMO energy because in this measurement an electron is injected into a molecule, just as would occur upon charge injection from a device electrode. If this technique is not available, the optical gap measured by UV-Vis spectroscopy can provide an approximation of the transport gap, i.e. the HOMO-LUMO energy difference for a molecule ionized during transport. The optical gap is usually 0 → 1 eV less than the measured transport gap because of exciton effects.<sup>142</sup> For example, the energy diagram for Alq<sub>3</sub> given in Figure 5.3 (a) is typical of diagrams presented in the literature.<sup>137,139,143-147</sup> The HOMO-LUMO gap is given as 2.8 eV, the same as the optical gap, but

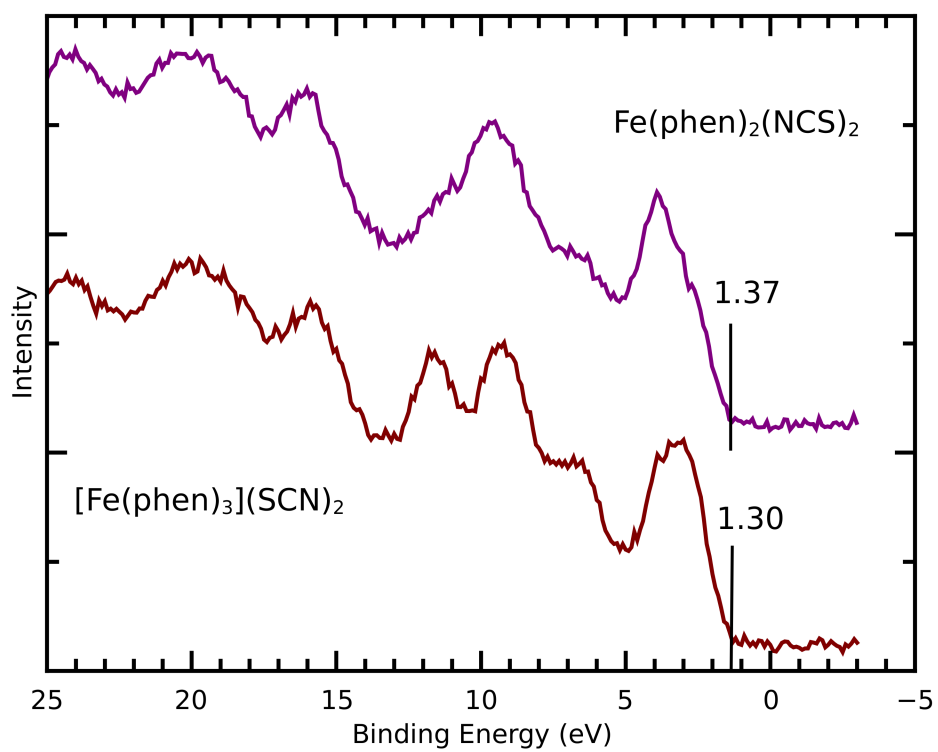


**Figure 5.4.** Valence band spectra measured by XPS for FeP2 (top trace) and FeP3 films (bottom trace). The onset of the HOMO is marked for each.

the transport gap has been measured by UPS and IPES to be 3.6 eV.<sup>142</sup> Because of instrument limitations, the optical gap is considered here.

Through the analysis described above, it is determined that the HOMO of FeP3 lies 1.3 eV below the Fermi level of the x-ray photoelectron spectrometer (as determined by its work function). Using the optical gap determined from the UV-Vis spectrum (Chapter 3), the LUMO lies 2.1 eV higher in energy. For FeP2, the HOMO about 1.4 eV below the work function of the x-ray photoelectron spectrometer and the LUMO is 2 eV higher in energy (UV-Vis spectrum in Chapter 4). Within the uncertainty of the approximations made and those of the measurements, the electronic levels of FeP2 and FeP3 are the same. It would be unusual for the HOMO's of these materials to lie high in energy and closer than the LUMO's to the Fermi level of the Al or Al/LiF electrodes. It is assumed that for the device configuration used in this study, transport through the FeP3 and FeP2 devices will be electron-only. Alq<sub>3</sub> provides a good reference material against which to compare the electron transport characteristics, since it has a relatively high electron mobility.

## 5.2 [Fe(phen)<sub>3</sub>](SCN)<sub>2</sub> Devices

The FeP3 films grown from vapor deposition of FeP2 are amorphous and smooth (see Chapter 3) and highly suited to device fabrication, so long as exposure to air during fabrication is minimized. In Figure 5.5 (a) J-F characteristics are presented for four different junctions, each on a different device of the same batch. The FeP3 film thickness in each case is ~220 nm and all devices were measured at 300 K. Reproducibility within the batch is excellent. On a log-log plot, the curves show two distinct regions. At lower fields, the slope of the curve is ~1 and conduction is Ohmic.

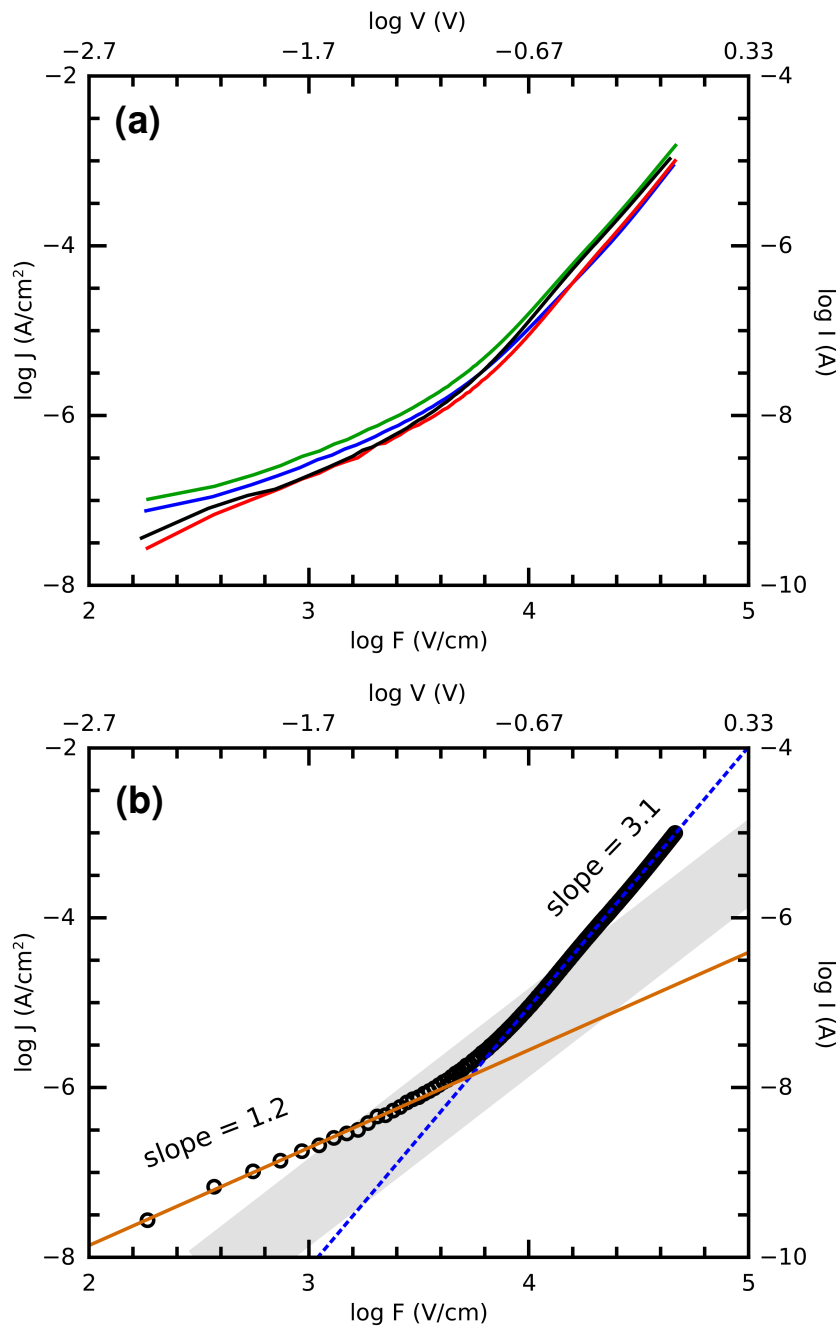


**Figure 5.5.** J-F characteristics for four Si/Al/LiF/FeP3/LiF/Al junctions each on a different sample (a). All samples were made simultaneously and the FeP3 thickness for each was  $\sim 220$  nm. Each  $\log J$  vs.  $\log F$  curve shows two distinct linear regions (b). At low fields, conduction is Ohmic (solid line). At higher fields, the slope of the curve is  $\sim 3$  (dashed line). The shaded region represents the current density expected for a material of the same thickness with a mobility between  $1 \times 10^{-5}$  and  $1 \times 10^{-6}$  cm<sup>2</sup>/V·s and operating by ideal SCLC.

Ohmic conduction occurs when the number of injected charge carriers is fewer than the number of intrinsic carriers of the material. As the bias is increased and more charge carriers are injected, they eventually outnumber the intrinsic carriers and the conduction behavior changes.<sup>148</sup>

At fields higher than  $1 \times 10^4$  V/cm, the slope of the curves changes to a value close to 3. Power law dependence of  $J$  on  $F$  in the form of  $J \propto F^k$  with  $k > 2$  entails a device operating below the SCLC maximum. This might arise from the presence of traps within the film or from injection limited current, for example. In the former case, application of higher fields can often achieve SCLC by increasing the number of injected charge carriers until the traps are filled.<sup>148</sup> The performance of the device can be compared to that of an ideal device of the same thickness operating with SCLC with a mobility typical of organic semiconductors. In panel (b) of Figure 5.5 the 300 K J-F characteristic for one of the junctions in panel (a) is overlaid atop a shaded region which represents the behavior expected for a material with a mobility of  $1 \times 10^{-6}$  to  $1 \times 10^{-5}$   $\text{cm}^2/\text{V}\cdot\text{s}$  operating with SCLC. It seems safe to conclude that the electron-only FeP3 devices outperform the idealized device; their mobility is predicted to exceed that of Alq<sub>3</sub>. FeP3 might prove useful in real-world applications, especially as an electron transport material. Its role might be complimentary to that of Alq<sub>3</sub> since the latter is often selected for use in photovoltaics because of its optical properties and the same properties of FeP3 are very different.

The J-F characteristics measured at varying temperature are shown in Figure 5.6 (a). The sample was mounted to the cold head of a cryogenic chiller and enclosed in a small evacuated chamber ( $\sim 1 \times 10^{-2}$  Torr). Temperature was controlled by activating a resistive heating element near the device and was measured from a thermocouple directly below the sample on the opposite side of the cold head. For these measurements, temperatures were changed and monitored manually by

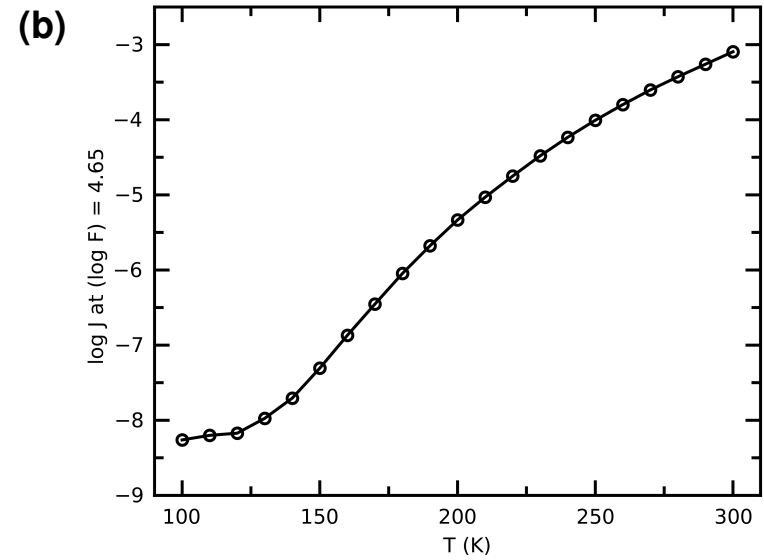
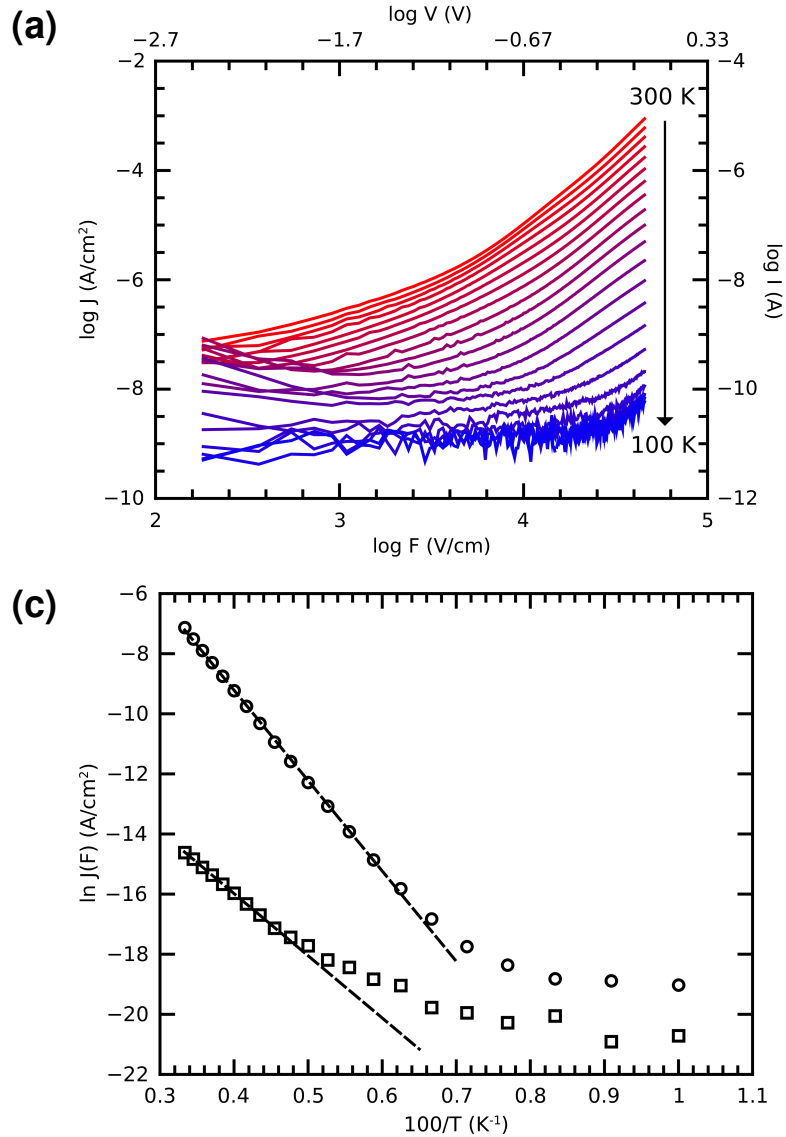


**Figure 5.6.** Temperature dependence of the J-F characteristic of one junction of a Si/Al/LiF/FeP3/LiF/Al device with a 220 nm FeP3 layer. Full J-F scans measured every 10 K upon warming are shown in (a). The current density is plotted as a function of  $T$  at the highest applied field ( $\sim 1 \times 10^{4.65}$  V/cm) in (b). The Arrhenius behavior of the current density at maximum field and at a lower field ( $\sim 1 \times 10^{3.20}$  V/cm) is plotted in (c).

observing the readout from the thermocouple. To keep the length of the experiment practical, scans were taken every 10 K. Once the desired temperature was obtained and appeared stable, collection of the J-F (really I-V) characteristic was initiated via a custom built software package.

The temperature dependence of the electron mobility in FeP3 is immediately obvious. Between 300 and 100 K, the current density at the highest measured field changes by at least five orders of magnitude. The temperature dependence of the current density at this field appears to follow Arrhenius behavior and  $\ln J \propto T^{-1}$  at least at high temperatures (Figure 5.6 (c)). Conduction is thermally activated at low bias where  $J \propto F$  and at high bias where  $J \propto F^3$ . The activation energies in these two regions are 180 meV and 260 meV, respectively. In the Ohmic region of the J-F characteristic, the current density is proportional to the total number of charge carriers,  $n$ , in the film

$$J = nq\mu F \quad (5.4)$$

where  $q$  is the elementary charge. The thermal activation energy in this region represents the barrier to charge injection. The barrier is sufficiently low that the contact of the Al/LiF electrodes with the FeP3 film can be considered Ohmic. Conduction above the Ohmic region of the J-F characteristic will be bulk-transport limited.

In amorphous organometallics like FeP3, where only weak van der Waals interactions exist between molecules and electron orbitals are highly localized on individual molecules, conduction is expected to occur via a hopping mechanism.<sup>149</sup> In this construct, charge carriers must overcome energetic barriers in order to transport between frontier orbitals on adjacent or nearby molecules. The efficiency of hopping increases with temperature because the extra thermal energy increases

the likelihood of overcoming the energy barriers and for hopping to occur. This is contrasted with inorganic semiconductors and highly crystalline organic materials in which orbitals extend across many molecules or atoms. Such materials suffer a loss in performance as temperature increases because ballistic transport is interrupted when charge carriers scatter from interaction with lattice phonons. It is tempting to assign the activation energy derived from the Arrhenius plot (Figure 5.6 (c)) to some kind of average energetic barrier between molecules or to an average trap depth. However, as mentioned by Coropceanu et al., the Arrhenius dependence of J on T is only an empirical observation and may have no real physical justification.<sup>150</sup>

Before moving on to discuss the electrical characterization of FeP2 films, a comment must be made about the behavior of the J-F characteristics at the lowest applied fields. For some J-F curves measured at intermediate temperatures, the current density at the lowest field is seen to be higher than for curves measured at higher temperatures. This seems to be in contradiction to the expected temperature-dependence of hopping transport and in contrast to the behavior seen at higher fields. The effect was observed for all junctions measured in the batch and is believed to be an artifact of measuring at extremely low power levels (low voltage and low amperage). Similarly, the magnitude of the current density appears to plateau at very low temperatures and fields, but this is only because the limit of detection of the experimental configuration is being exceeded.

### **5.3 Fe(phen)<sub>2</sub>(NCS)<sub>2</sub> Devices**

Initial attempts to fabricate and measure vertical junction devices incorporating FeP2 as the active material were unsuccessful: junctions were found to be shorted, always. Penetration of the top electrode through the film to the bottom electrode was identified as the likely cause and other

metals were tested as top electrodes. Figure 5.7 is an optical micrograph taken through the objective of the Raman microscope of a Pb electrode deposited onto a granular FeP2 film. The underlying substrate is the bare Si wafer. Even with a thickness of 100 nm, the surface topography of the FeP2 is apparent through the Pb electrode, including the deep crevices between grains. The AFM imaging presented in Chapter 4 shows that the fissures between grains may be as deep as the FeP2 film thickness and 100 nm wide or more. It is not surprising that shorts of the top and bottom electrodes occur for these films. Other metals for rougher films that may mask the underlying topography of the FeP2 films but are nonetheless shorted.

A new approach is required. One approach tested was to build devices with horizontal junctions as described at the beginning of this chapter and shown in Figure 5.1 (c). When the triple bottom electrodes were deposited, a second mask was added to form a break at their centers. For this purpose, a 46 awg (40  $\mu\text{m}$  diam.) strand of Kanthal D wire was stretched across the electrode mask. The three electrodes are split into six by this process. When the FeP3 film is deposited across the electrodes, and later converted to FeP2, three horizontal junctions are formed per device. The spacing between the two electrodes of a single junction is the diameter of the Kanthal D wire, 40  $\mu\text{m}$ . The spacing is small enough that a single FeP2 grain might extend the entire distance. The width of a junction is the width of the electrodes, 1 mm. Unfortunately, this device geometry yielded no measurable junctions. Rather than shorts, the resistances of all junctions were found to be higher than that measurable using the maximum applied field of the source meter, 210 V.

A quick examination of a hypothetical device of typical mobility operating under ideal SCLC (Equation 5.3) demonstrates why this approach does not succeed with the given device dimensions. Using a mobility of  $\mu = 1 \times 10^{-6} \text{ cm}^2/\text{V}\cdot\text{s}$ , a transport distance of  $d = 40 \mu\text{m}$ , and taking

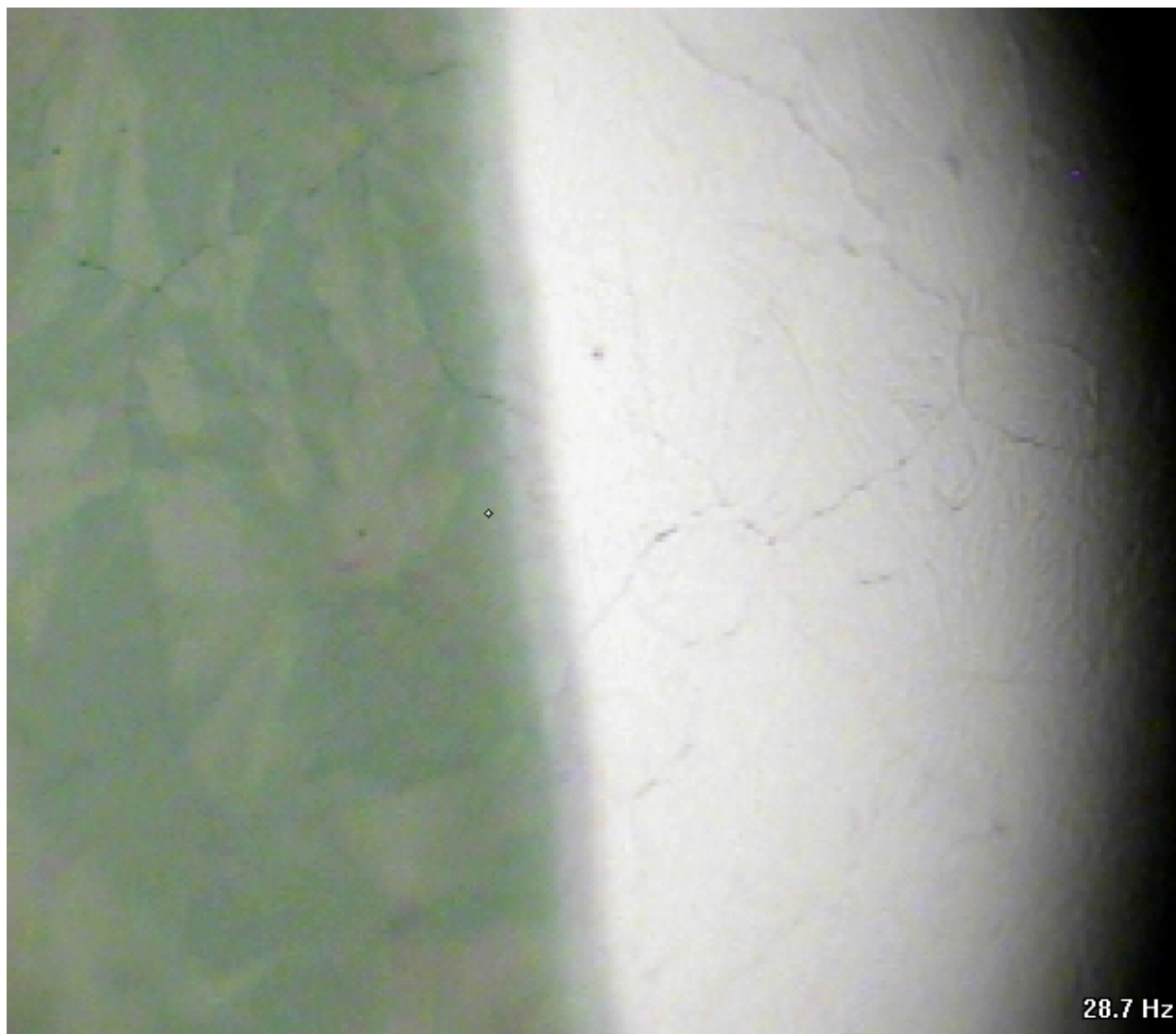


**Figure 5.7.** Optical micrograph of a granular FeP<sub>2</sub> film (100 nm nominal thickness) on Si (left) and covered by a 100 nm Pb film (right).

the junction area as the thickness of the film (e.g. 100 nm) times the width of the junction (1 mm), the current expected from the hypothetical junction is on the order of  $10^{-13}$  A, below the detection limit of the source meter. The limiting factors are the size of the gap between electrodes and the cross-sectional area of the junction. A reduction of the gap size to 50 nm would allow measurement with biases down to  $\sim 10$  V. Hence, for vertical junction devices, film thicknesses of 10's to 100's of nm are typically seen. Areas of vertical junctions are also much larger, on the order of  $1 \times 1 \text{ mm}^2$ . For horizontal junctions, the horizontal cross-sectional area is limited by the thickness of the film and cannot realistically approach the same dimensions. It is surprising then that in the original report of FeP2 thin films, currents as high as  $10^{-8}$  A were recorded and a mobility of only  $6.53 \times 10^{-6} \text{ cm}^2/\text{V}\cdot\text{s}$  was derived for a 240nm thick film in a horizontal junction with a spacing of  $2 \mu\text{m}$  between electrodes.<sup>26</sup>

When an FeP3 film is deposited across a rough substrate, the surface of the deposited film remains remarkably smooth. This observation led to the development of a multilayer deposition technique for the fabrication of FeP2 vertical junction devices. In the first stage of film growth, an FeP3 film is deposited atop the bottom electrodes and heated to effect conversion to FeP2. The films at this stage have are granular with large, deep crevices between film grains and are the subject of Chapter 4. In a second stage, another FeP3 film is deposited over the previous film in order to fill up the cracks and crevices of the FeP2 film. Another annealing step converts the second FeP3 layer to a second FeP2 layer. The process can be repeated to grow an arbitrarily thick FeP2 film with an arbitrary number of layers. Ideally, no cracks will remain in the final FeP2 film, or if they do, they will not extend through the entire thickness of the FeP2. Deposition of the top metal electrode can then be done without fear of shorting the device.

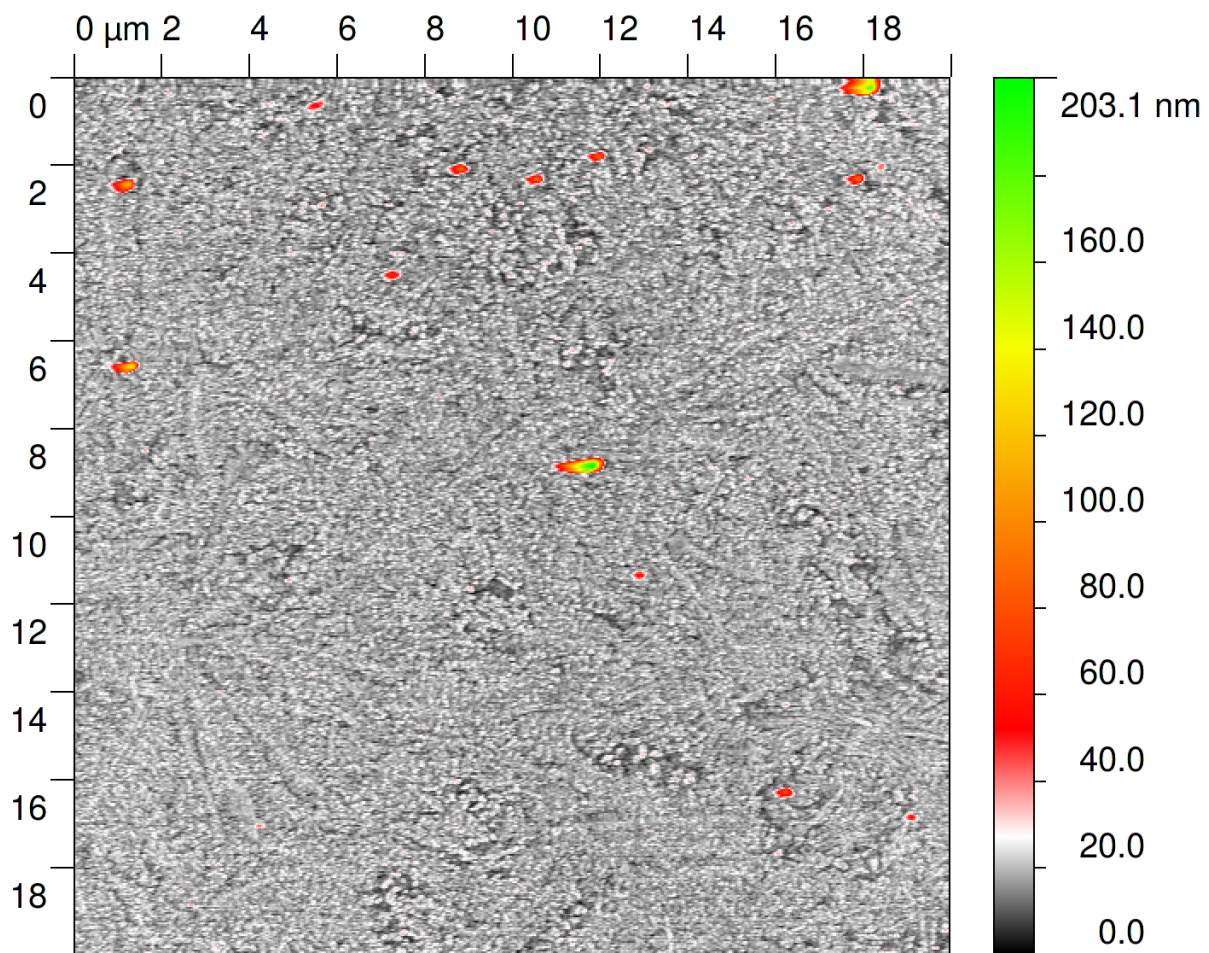


**Figure 5.8.** A 20 x 20  $\mu\text{m}^2$  AFM image of a 61 nm FeP2 film grown by sequential deposition and annealing of four layers. Directly under the film is an Al/LiF electrode. After capturing this image a top electrode was deposited and electrical characterization of the completed device is shown in Figures 5.10, 5.11, and 5.12.



**Figure 5.9.** Optical micrographs taken through the Raman microscope of FeP2 films grown in four layers by sequential deposition/annealing steps. The 61 nm film (on Al/LiF) shown in (a) is the same for which AFM images can be seen in Figure 5.8. Electrical characterization of the finished device made with this film is available in Figures 5.10, 5.11, and 5.12. A high contrast version of the image in (a) is shown in (b). Another multilayer FeP2 film (on Si) made simultaneously but with a different total thickness (37 nm) is shown in (c).

Figure 5.8 shows an AFM image of the surface of a multilayer FeP2 film atop an Al/LiF electrode grown by sequential deposition and annealing of four layers. While the film thickness is 61 nm, small pits in the film do not extend more than  $\sim 20$  nm below the surface. Over the  $20 \times 20 \mu\text{m}^2$  area no grain boundaries can be seen. In optical micrographs of these films (Figure 5.9) grains are still identifiable by their difference in contrast, but obvious grain boundaries are no longer observed. Electrical shorts were rarely found for vertical junction devices formed from these films.

The electrical characterization of the three junctions formed from the multilayer FeP2 film that is the subject of Figures 5.8 and 5.9 is presented in Figures 5.10, 5.11, and 5.12. The anomaly that occurs at 21 V in the  $J$ - $F$  characteristics of the first junction (Figure 5.10a) is an artifact of an automatic ranging feature of the source meter that was not used in subsequent experiments. Each junction was able to sustain fields higher than  $10^7$  V/cm because the current response was so weak. For comparison, the current density in these junctions at a field of  $10^5$  V/cm is  $\sim 10^{-8}$  A/cm<sup>2</sup> while for the FeP3 junctions examined in the last section, current densities approach  $10^{-2}$  A/cm<sup>2</sup> for the same field. At the highest fields measured, the slopes of the  $J$ - $F$  curves on the log-log plot approach 2. If the SCLC model is applied, mobilities near  $10^{-11}$  cm<sup>2</sup>/V·s are extracted. Whether the devices are operating at the SCLC limit or exhibit a  $J \propto F^2$  relationship at high bias only by coincidence, it is clear that the charge conduction in these devices is inferior to conduction in the FeP3 devices.

At first, this result seems surprising. Mobilities in crystalline organic semiconductors are in general higher than mobilities in amorphous materials.<sup>149</sup> This can be attributed to extended electronic interactions between molecules. In amorphous materials, molecular interactions are weak and there is positional and energetic disorder due to the randomness of local molecular environments. In Chapter's 3 and 4, it is shown that FeP3 and FeP2 films are amorphous and (poly)

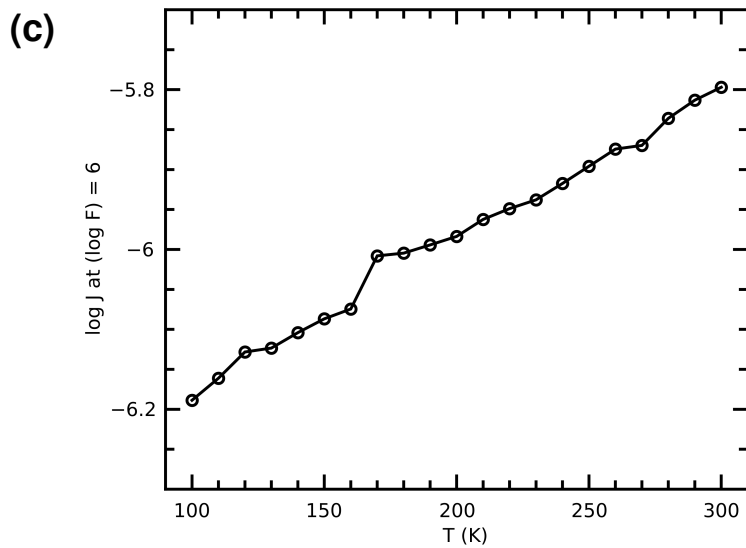
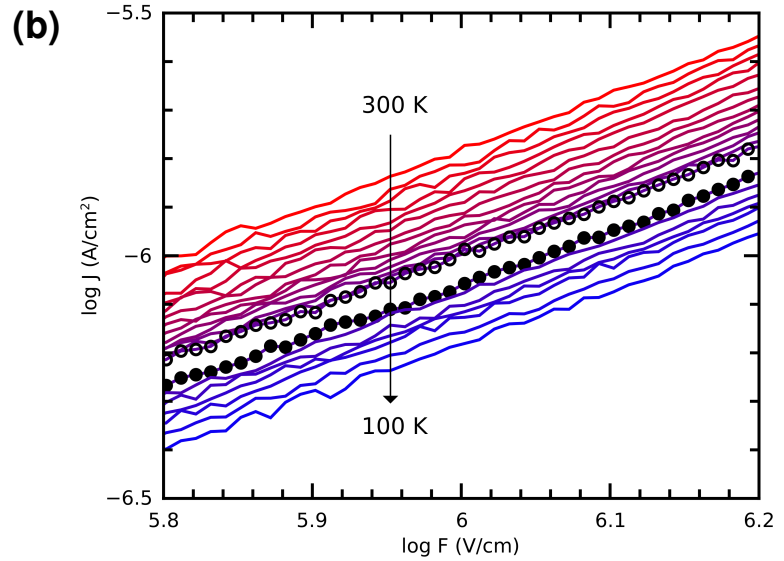
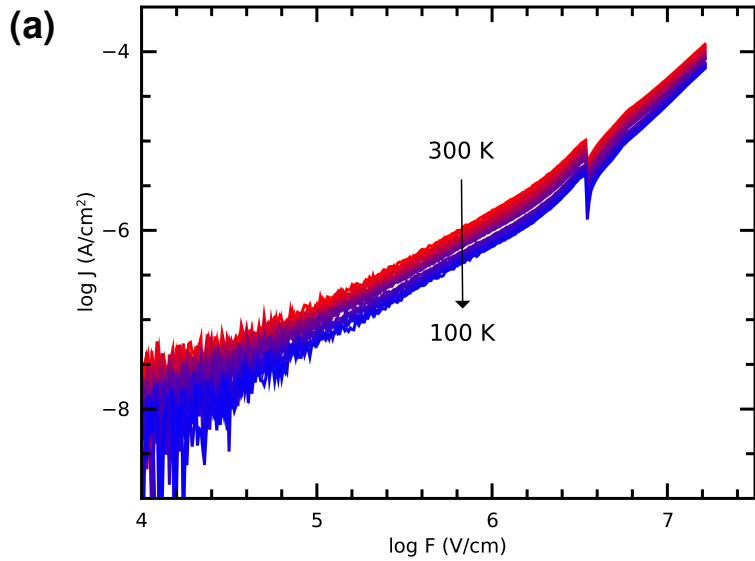


**Figure 5.10.** Temperature dependence of the J-F characteristic of Junction 1 of a Si/Al/FeP2/Al device with a 61 nm FeP2 layer grown in multiple successive depositions. Full J-F scans measured every 10 K upon cooling are shown in (a). The anomaly near  $\log(F) = 6.5$  is caused by the automatic measurement ranging of the sourcemeter switching modes at 21 V. A gap (b) is visible between scans measured at 170 (open circles) and 160 K (closed circles) which divides the J-T curve into two regions (c).

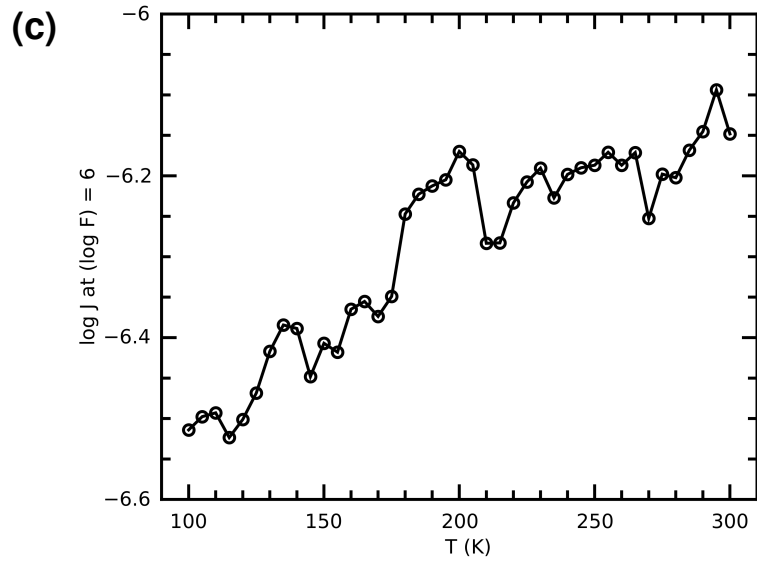
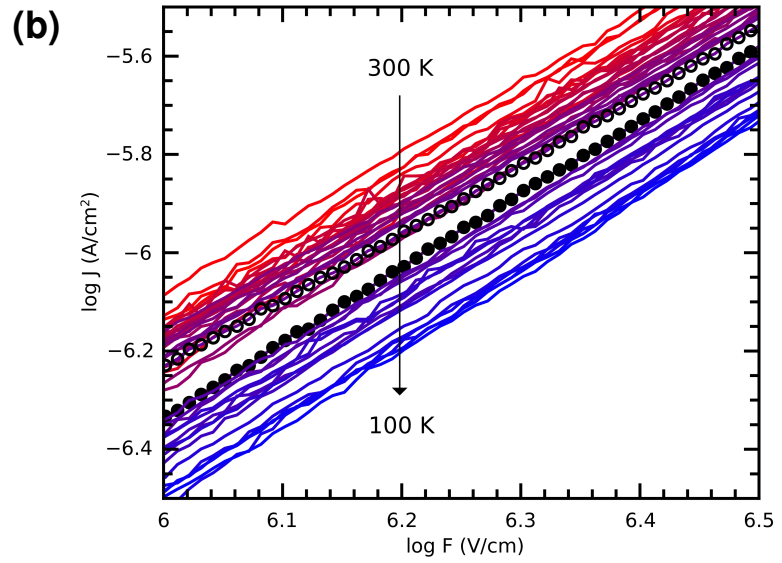
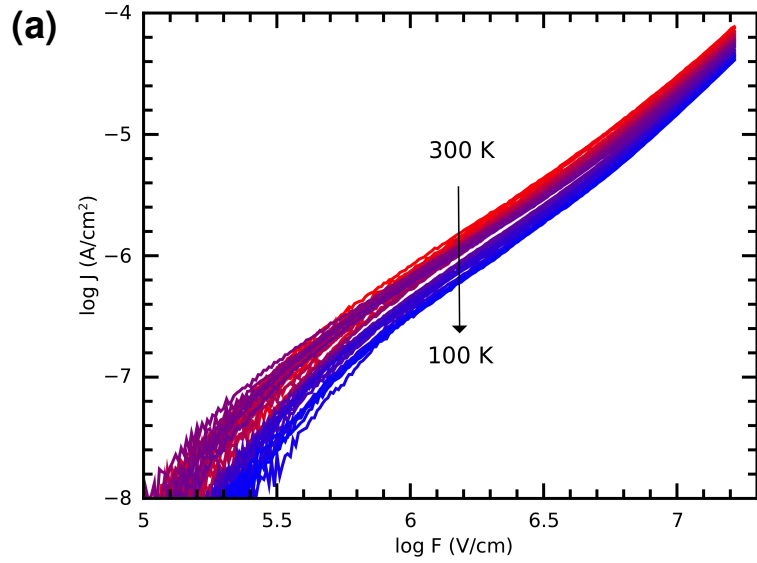


**Figure 5.11.** Temperature dependence of the J-F characteristic of Junction 2 of a Si/Al/FeP2/Al device with a 61 nm FeP2 layer grown in multiple successive depositions. Full J-F scans measured every 5 K upon warming are shown in (a). A gap (b) is visible between scans measured at 180 (open circles) and 175 K (closed circles) which divides the J-T curve into two regions (c).

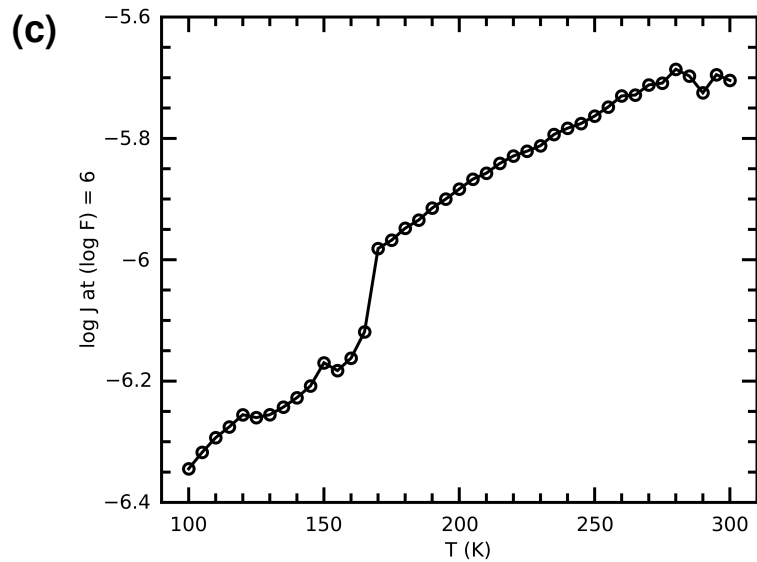
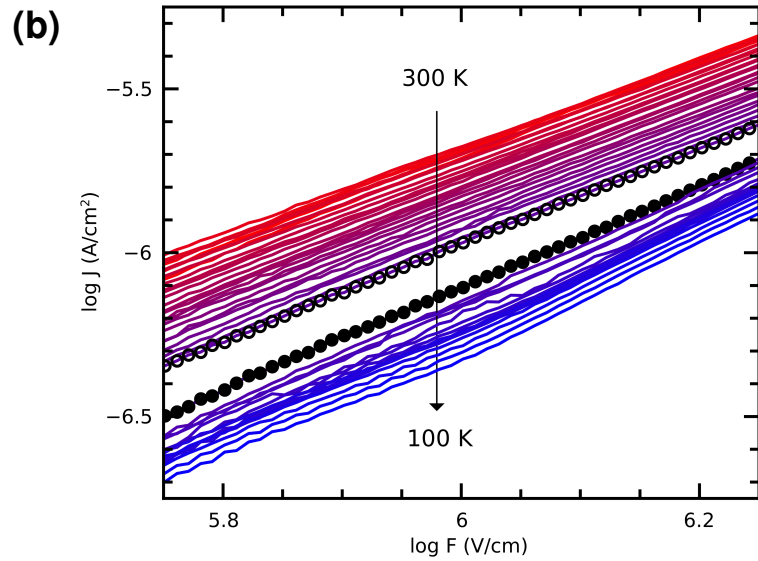
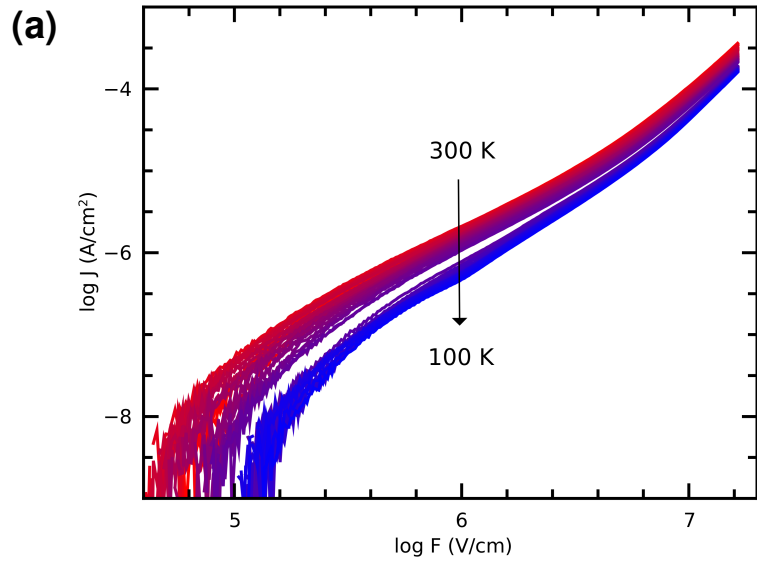


**Figure 5.12.** Temperature dependence of the J-F characteristic of Junction 3 of a Si/Al/FeP2/Al device with a 61 nm FeP2 layer grown in multiple successive depositions. Full J-F scans measured every 5 K upon cooling are shown in (a). A gap (b) is visible between scans measured at 170 (open circles) and 165 K (closed circles) which divides the J-T curve into two regions (c).

crystalline, respectively. However, even if transport across crystalline domains is efficient, another process can hinder conduction in the FeP2 films.

A clue to the conduction-limiting mechanism is found in the temperature dependence of the J-F characteristics. A change in temperature of 200 K is seen to effect a change of less than a factor of 10 in the current density measured at any field. This behavior is in stark contrast to that exhibited by the FeP3 devices which are strongly temperature-dependent. The conduction mechanism in these FeP2 films is unlikely to be a hopping mechanism which is thermally activated. Band transport, as well, is temperature-dependent, though with an inverse relationship, and can be ruled out. Only conduction limited by tunneling is expected to occur independent of temperature. Most often, tunneling in vertical devices occurs at the interface of the electrode and the molecular layer when the barrier to injection is sufficiently high. Injection barriers may exist because of a mismatch between the Fermi energy of the electrons in the metal electrodes and the molecular orbitals of the semiconductor layer, traps at the interface, or interfacial dipoles. Conduction in such devices is injection-limited. Tunneling within the film itself cannot be ruled out, either. The boundaries between grains, like the interfaces at the electrodes, might pose barriers that require tunneling in order for carriers to traverse. In this case, the conduction through the films would be bulk-transport-limited.

The junctions measured for Figures 5.10, 5.11, and 5.12 contained no interfacial LiF between the Al electrodes and the FeP2 films. In order to investigate the injection efficiency at the electrode-film interface and to provide a better comparison the the FeP3 devices measured and presented in the previous section, which contained such interfacial layers, a second FeP2 device was fabricated this time placing LiF atop the bottom Al electrode and beneath the top Al electrode.

The electrical characterization of one junction from this device is shown in Figure 5.13. At a field of  $10^5$  V/cm, the current density in the FeP2-LiF junction is similar to that of the other FeP2 junctions and far below that approached by the FeP3-LiF junctions. But, as the field is increased, current density in the FeP2-LiF junction quickly outpaces conduction in the FeP2 junctions already presented. At  $10^6$  V/cm, current density is improved by four orders of magnitude. The conduction in the improved junctions is still inferior to FeP3 junctions, but it is enough that scanning to higher fields could not be undertaken for fear of breakdown. The improved FeP2-LiF junctions still exhibit only weak temperature dependence suggesting tunneling as the dominant conduction limiting mechanism again. Since the introduction of LiF at the electrode interfaces positively affects current in the devices, inefficient charge injection from the electrodes is probably the major the current-limiting mechanism for these FeP2 junctions.

Upon close examination of the J-F curves for each junction, a small gap is noticed that appears to divide the sets of curves into two groups. The plots in panel (b) of each of Figures 5.10, 5.11, and 5.12 show the J-F curves in detail near a field of  $10^6$  V/cm where the gaps can be seen more clearly. When the current densities at this field are plotted as a function of temperature (panel (c) of each figure), the gaps are manifested as discontinuities in the resulting J-T curves. The break in the J-T curves is small for the first two junctions (Figures 5.10 and 5.11) and might otherwise be overlooked if it were not for the obvious discontinuity in the J-T curve for the third junction (Figure 5.12). On opposite sides of the discontinuity, the temperature-dependence of the current density is slightly different. Most intriguing is the abruptness of and temperature range over which the change in temperature-dependence occurs. In each case, the discontinuity occurs between two sequential scans measured 5 (junctions 2 and 3) or 10 K (junction 1) apart. For junctions 1, 2, and

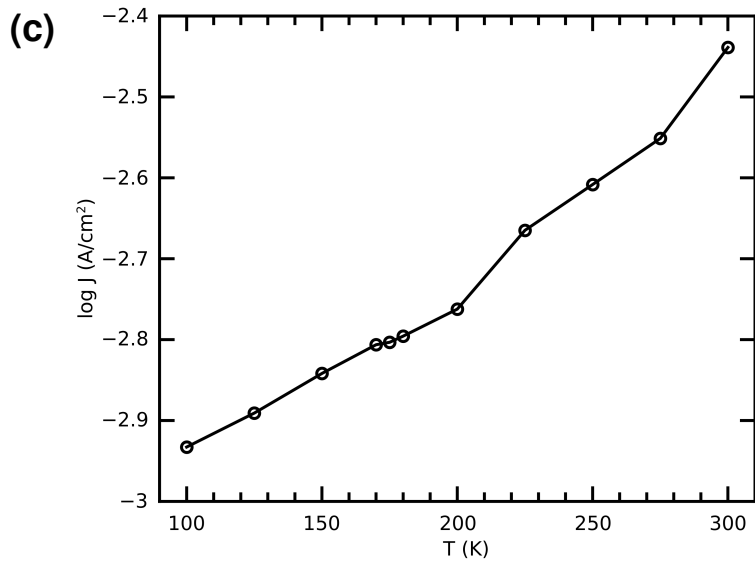
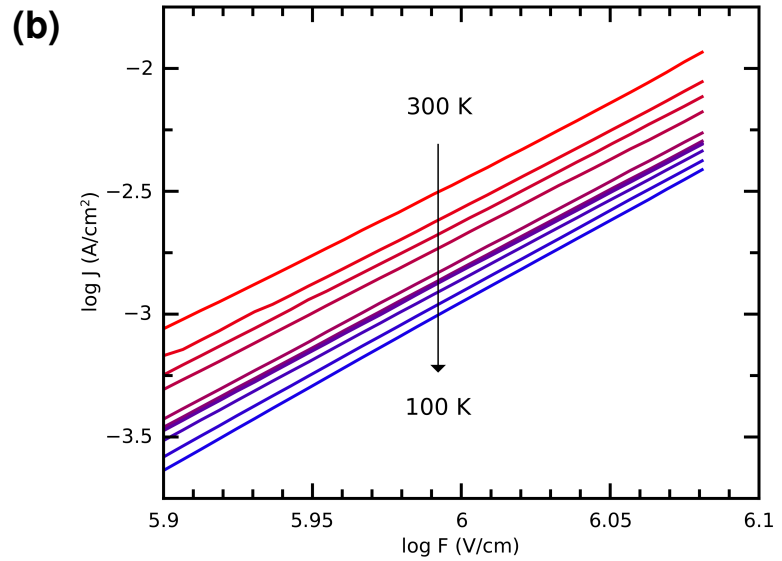
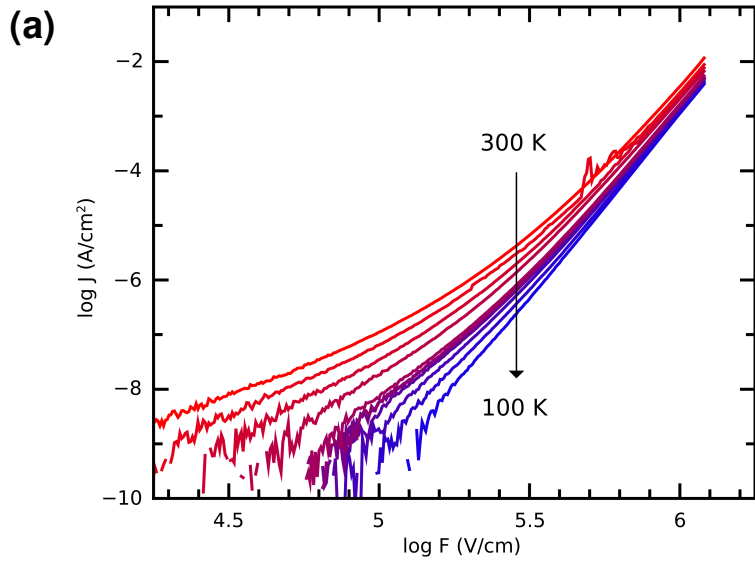


**Figure 5.13.** Temperature dependence of the J-F characteristic of one junction of a Si/Al/LiF/FeP2/LiF/Al device with an 83 nm FeP2 layer grown in multiple successive depositions. Full J-F scans measured upon cooling are shown in (a). The high-field region is examined in detail in (b). The current density at  $F = 1 \times 10^6$  V/cm is shown as a function of temperature in (c).

3, the break occurs between the temperatures of 170/160, 180/175, and 170/165 K, respectively.

That is, the effect is seen near the SCO temperature of FeP2.

During the SCO from HS to LS, the six Fe-N coordinate bonds contract in length by around 10% because the antibonding  $e_g$  orbitals are depopulated. This change at the molecular level affects the crystal packing and the unit cell of FeP2 is reduced in volume some 5%.<sup>74</sup> The FeP2 films, being comprised of crystalline domains, are expected to experience a change in volume or at least a development of strain from this contraction. Recent computational experiments suggest that the strain experienced by SCO films undergoing transition may be so great as to cause the films to buckle out of plane.<sup>151</sup> No evidence of a bucking effect was observed in these films, but a reversible change in volume could explain the anomaly of the temperature dependence of the current density that occurs near the SCO temperature of FeP2.

In some conduction models, the current is strongly dependent on the film thickness. For example, for the SCLC model (Equation 5.3) the current varies as a function of the inverse cube of the film thickness. A small change in film thickness might induce a noticeable change in the current density at the spin transition. It is shown in Chapter 4 that the crystalline domains of an FeP2 film are oriented with the  $c$ -axis perpendicular to the plane of the film while the  $a$  and  $b$ -axes lie parallel to the same plane. A change in the length of the  $c$ -axis might produce a change in the thickness of the film and a change in the measured current density. Upon transitioning from the HS to LS state, the  $c$ -axis of the FeP2 crystal reduces in length by about 1.5%.<sup>74</sup> For an extreme dependence of  $J \propto d^{-3}$ , the current density could be expected to increase by no more than 5%. For the junction in Figure 5.12 the current density changes by nearly 20%. More importantly, any shrinkage of the  $c$ -axis, and therefore the film thickness, should *increase* the current density but the observed

anomaly involves a *decrease* in  $J$ . A change in film thickness that might result from SCO cannot explain the observed effect.

The current through a thin film is also proportional to the area of the films. A decrease in area of the films should cause a decrease in the measured current, and if a static area is assumed when calculating  $J$ , as has been done here, then the calculated current density (but not the real current density) will show a proportionate decrease. Once again, the reduction of the crystallographic axes, this time the  $a$  and  $b$ -axes, can be used to predict the magnitude of any hypothetical change in area that might occur. In this case, the film area can only be expected to shrink a maximum of  $\sim 4\%$ . The dependence on area is too weak to explain a 20% decrease in current. And, adhesion to the substrate likely prevents any major reduction in film area.

It can be concluded that any SCO-induced changes in the film geometry are not the cause of the anomaly observed in the  $J$ - $T$  curves near 160 to 180 K. Instead, it may be the case that the intrinsic mobility of the FeP2 films changes upon SCO. Few experiments to date have measured the electrical properties of SCO materials and the results of these experiments are not entirely consistent with some authors reporting a higher conductivity for the LS state<sup>39,41,43,44,50</sup> and others for the HS state.<sup>45,152</sup> Differences in sample form and conduction mechanisms (e.g. tunneling vs. hopping) complicates comparison. Computational experiments, however, are in agreement and predict that the HS forms of SCO molecules should show a higher conductivity.<sup>36,37</sup> This conclusion is reached on the basis of the predicted densities of states for the two spin states. In the HS case, there is a higher density of states, both occupied and unoccupied, near the Fermi level. That is to say, the HOMO-LUMO gap is smaller for the HS state. The results here are in agreement with the computational studies in that conductivity is larger for the HS state. In this work the low

temperature (LS) valence-band x-ray photoelectron spectrum was not obtained. Nor was the UV-Visible absorption spectrum of the LS FeP2 complex measured. Though, other authors have measured the absorption spectrum and have found that the optical gap for the LS complex is smaller in energy than that for the HS complex, the optical gap may not accurately represent the transport gap. Admittedly, the compatibility of the electrical properties of the FeP2 films here with the prior computational studies may only be fortuitous.

A third possible mechanism might be interaction of transported electrons with the unpaired spins in the HS complex. An effect such as this is expected to cause scattering of transported electrons and holes. If this were the case, while in a high magnetic spin state, the film would conduct less efficiently and the current density would be higher in the LS state. Once again, this explanation cannot explain the results obtained here where the current density is lower below the spin transition temperature.

In closing, it must be said that the anomaly in the J-T curves of the FeP2 junctions in Figures 5.10, 5.11, and 5.12 is not consistently reproduced. Even for the same junctions for which the data is presented, other scans made before or after, on warming or cooling, did not show any such anomalies. For example, in the temperature-dependent current density measurements of the 83 nm multilayer FeP2 film junction with Al/LiF electrodes shown in Figure 5.13, there is no obvious change in the dependence that occurs near the SCO temperature. There does appear to be a break between the scan measured at 225 and that at 200 K, but this artifact occurred because a lengthy pause in time was taken between the two scans.

## 5.4 Summary

The amorphous FeP3 films deposited directly from FeP2 lend themselves to vertical junction device fabrication. Reproducibility of the electrical characteristics was good for the few junctions created. These initial results suggest that the intrinsic mobility of electrons in FeP3 films is at least on par with common organic semiconductors and may be higher than the prototypical organic semiconductor Alq<sub>3</sub>. The material might find use as an electron transport layer for applications such as light harvesting and organic light-emitting diodes. Further investigation is needed to confirm these initial results and to establish the hole mobility of the material. In addition, UPS and IPES experiments should be undertaken to determine the absolute energies of the HOMO and LUMO for the material so that appropriate electrode metals can be selected for electron-only and hole-only transport.

When the amorphous FeP3 films are converted to FeP2 and built into vertical junction devices, the junctions are found to be shorted in every case. The cause of the shorts is probably penetration of the vapor-deposited top electrode through cracks and grain boundaries down to the bottom electrode. A horizontal device geometry could overcome the need for a top electrode but would require inconveniently narrow gaps between electrodes. Instead, films of FeP2 can be built up in layers by repeating deposition and annealing stages. The multilayer FeP2 films produced in this way possess a smoother topography overall without crevices or cracks between grains. Vapor deposition of top electrodes on these films yields measurable junctions reliably. Conduction through the films is poor. The weak temperature dependence implies that at least part of the conduction-limiting mechanism is tunneling. Introduction of LiF at the interfaces of the films and the electrodes improves conduction which suggests contact with the Al electrodes is otherwise poor

and there is a large barrier to carrier (electron) injection. The temperature dependence of the current density occasionally shows a split behavior, being higher above the spin transition temperature of FeP2. The origin of this effect cannot easily be ascribed to changes in the geometry of the films. Nor can it be assigned to spin-state dependent scattering of charge carriers. It may well be correlated with the difference in the HOMO-LUMO gaps of the two magnetic spin states. The difficulty in providing an explanation for the behavior of the FeP2 films highlights the need for further characterization of the electrical properties of SCO materials. Experiments should span a large range of materials, scales, and transport mechanisms, but be designed in a more systematic way, so that the results are more easily compared between studies.

If proved to exist, any effect from the SCO on the current through the FeP2 junctions is small, but not necessarily insignificant. On the other hand, the poor conduction characteristics of these films will limit their potential uses. Conductivity is probably limited by injection at the electrode interface. Device performance may be improved by selection of different electrode materials or introduction of materials at the interfaces in order to mediate conduction between the electrodes and films. There is a strong chance that ultimate device performance will be constrained by the quality of the FeP2 films at the interfaces and throughout the bulk. A new process for the fabrication of films is therefore desired. Other SCO materials which lend themselves more easily to thin film preparation are more appropriate for the development of devices based on novel SCO-dependent electrical properties. That said, the small effects observed near the SCO temperature in these films should encourage activity in the field.

## CHAPTER 6

### CONCLUSIONS

With recent attention given to nanoscale applications, the field of SCO research is as active and energetic as it was at its beginnings in the 1960's and 70's. That early period of exploration was ignited by the discovery of SCO for the first time in a synthetic complex, i.e. in the title compound FeP2. Fittingly, the nanoscale SCO renaissance currently underway was largely motivated by the vapor deposition of FeP2 thin films, another first for SCO materials.<sup>25,26</sup> At the moment, the next target is to realize fully the potentials of SCO materials. There is no doubt that FeP2 will play an important role in achieving this goal, as it has done throughout the history of SCO research. This work has hopefully taken a few steps long that path.

First, the synthesis by direct precipitation was refined to exclude impurities and consequent ambiguities and to maximize yields. This refinement will no doubt increase the attractiveness of the material to a new generation of scientists and help to maximize the experimental return on investment of raw materials. Second, a thorough spectroscopic and structural characterization has been completed on the thin films that are deposited directly from FeP2. As it turns out, these films were found to be FeP3 instead of the target complex. While unexpected, and as of yet mechanistically unexplained, the deposition of FeP3 films from FeP2 could prove to be a blessing in disguise. The optical properties of FeP3 are quite interesting especially the change in color that occurs on oxidation. Already the effect has been incorporated into an electrochromic display.<sup>54</sup>

Vapor deposition opens an entirely new avenue for the inclusion of this material into active devices. Additionally, the results of the preliminary electrical characterization given here suggest that FeP3 has a mobility at least as great as common inorganic semiconductors. Films from this material may have an impact on devices in related fields, such as photovoltaics. The possibility exists that through appropriate ligand modification, SCO-active forms of FeP3 may be deposited into thin films in the same way. Thus, FeP3 may become a vehicle in which SCO properties are introduced into current and future technologies.

Through much toil and steadfast determination, the primary goals of this work were eventually achieved. Films of the SCO-active material FeP2 were fashioned, although not by the means originally imagined at the outset of this work. Instead of direct vapor deposition of FeP2 films, a modified process was developed in which FeP3 films are annealed and converted to the target material. The conversion process is completely analogous to the conversion of FeP3 powder into FeP2 by pyrolysis. Unfortunately, the ultra-smooth, uniform surfaces of the FeP3 films are not preserved upon conversion and the FeP2 films suffer from deep grain boundaries. When vertical electrical devices are made from these films, penetration of the top electrodes through the films shorts all devices. Yet, by sheer persistence in the face of repeated failures, and perhaps imprudence, this obstacle, too, was overcome. By depositing and annealing multiple layers of films from FeP2 on top of one another, it is possible to grow a granular, polycrystalline FeP2 film whose surface is continuous. From these films, vertical devices can be assembled and the first results of their electrical characterization has been presented. Conduction through these devices is rather low which is perhaps best ascribed to the poor contact between electrodes and the FeP2 films. Unfortunately, the nature of the contact seems likely to be an inherent consequence of the

fabrication process, i.e. the multilayer film technique. It is doubtful that this technique can produce devices of sufficient quality for commercial application. Yet, all is not lost. The multilayer films may simply be better suited to other device geometries, such as the field effect transistor geometry. Importantly, a small change in the conductivity of the films was observed near the spin transition temperature. The HS state of this material appears to be more conductive. Considering that current in these devices is probably limited by poor injection efficiency where contacted by the electrodes, it is quite remarkable and fortunate that any effect was not masked by the more dominant current limiting mechanism. It may well be the case that once efficient injection is achieved, current through the FeP2 films is bulk transport limited and shows severe effects at the spin transition temperature. As this project comes to a close, the hope is that the reader may find this result irresistibly tantalizing and forge ahead toward the ultimate aim of SCO modulation of electrical current and vice versa.

Finally, the possible manufacture of films of the theoretical complex  $\text{Fe}(\text{phen})(\text{SCN})_2$ , called FeP1 here, should not be overlooked. As a one dimensional coordination polymer, the bulk properties of this material, including its electrical conductivity, are likely to be different than both of the other  $\text{Fe}(\text{phen})_x(\text{SCN})_2$  complexes studied here already. A new molecule means new potential and new opportunities. And yet, exploration on this new experimental front should progress quickly because of the extensive body of work that already exists for FeP2 and FeP3. The optimist might envision in the near future a kind of chemical hat trick in which all three related molecules, FeP1, FeP2, and FeP3, leave their mark on the discipline.

## REFERENCES

- 1 Gütlich, P. Spin Crossover – Quo Vadis? *Eur. J. Inorg. Chem.* **2013**, 581-591.
- 2 Hauser, A. Ligand Field Theoretical Considerations. *Adv. Polym. Sci.* **2004**, 233, 49-58.
- 3 Halcrow, M. A. Structure: Function Relationships in Molecular Spin-Crossover Materials. In *Spin-Crossover Materials: Properties and Applications*; Halcrow, M., Ed.; Wiley & Sons: West Sussex, U.K., 2013; Chapter 5, pp 147-169.
- 4 Sorai, M.; Seki, S. Magnetic Heat Capacity Due to Cooperative Low-Spin  $^1A_1$  High-Spin  $^5T_2$  Transition in  $Fe(phen)_2(NCS)_2$  Crystal. *J. Phys. Soc. Japan* **1972**, 33, 575.
- 5 Gütlich, P.; Goodwin, H. A. Spin Crossover – An Overall Perspective. *Top. Curr. Chem.* **2004**, 233, 1-47.
- 6 Shores, M. P.; Klug, C. M.; Fiedler, S. R. Spin-State Switching in Solution. In *Spin-Crossover Materials: Properties and Applications*; Halcrow, M., Ed.; Wiley & Sons: West Sussex, U.K., 2013; Chapter 10, pp 281-301.
- 7 Gütlich, P.; Link, R.; Steinhäuser, H. G. Mössbauer-Effect Study of the Thermally Induced Spin Transition in Tris(2-picolyamine)iron(II) Chloride. Dilution Effect in Mixed Crystals of  $[Fe_xZn_{1-x}(2-pic)_3]Cl_2 \cdot C_2H_5OH$  ( $x = 0.15, 0.029, 0.0009$ ). *Inorg. Chem.* **1978**, 17, 2509-2514.
- 8 Halcrow, M. A. Spin-Crossover Compounds with Wide Thermal Hysteresis. *Chem. Lett.* **2014**, 43, 1178-1188.
- 9 Decurtins, S.; Gütlich, P.; Köhler, C. P.; Spiering, H. Light-Induced Excited Spin State Trapping in a Transition-Metal Complex: The Hexa-1-Propyltetrazole-Iron (II) Tetrafluoroborate Spin-Crossover System. *Chem. Phys. Lett.* **1984**, 105 (1), 1-4.

- 10 Chong, C.; Slimani, A.; Varret, F.; Boukheddaden, K.; Collet, E.; Ameline, J.; Bronisz, R.; Hauser, A. The Kinetics Features of a Thermal Spin Transition Characterized by Optical Microscopy on the Example of  $[\text{Fe}(\text{btr})_3](\text{ClO}_4)_2$  Single Crystals: Size Effect and Mechanical Instability. *Chem. Phys. Lett.* **2011**, *504*, 29-33.
- 11 Slimani, A.; Varret, F.; Boukheddaden, K.; Chong, C.; Mishra, H.; Haasnoot, J.; Pillet, S. Visualization and Quantitative Analysis of Spatiotemporal Behavior in a First-Order Thermal Spin Transition: A Stress-Driven Multiscale Process. *Phys. Rev. B: Condens. Matter Mater. Phys.* **2011**, *84*, 094442.
- 12 Varret, F.; Slimani, A.; Boukheddaden, K.; Chong, C.; Mishra, H.; Collet, E.; Haasnoot, J.; Pillet, S. The Propagation of the Thermal Spin Transition of  $[\text{Fe}(\text{btr})_2(\text{NCS})_2]\cdot\text{H}_2\text{O}$  Single Crystals, Observed by Optical Microscopy. *New J. Chem.* **2011**, *35*, 2333-2340.
- 13 Slimani, A.; Varret, F.; Boukheddaden, K.; Garrot, D.; Oubouchou, H.; Kaizaki, S. Velocity of the High-Spin Low-Spin Interface Inside the Thermal Hysteresis Loop of a Spin-Crossover Crystal, via Photothermal Control of the Interface Motion. *Phys. Rev. Lett.* **2013**, *110*, 087208.
- 14 Ruauadel-Teixier, A.; Barraud, A.; Coronel, P. Spin Transition in a Magnetic Langmuir-Blodgett Film. *Laboratoire de Spectrochimie des Elements de Transition* **1988**, 107-115.
- 15 Coronel, P.; Ruauadel-Teixier, A.; Barraud, A. LB. Films Exhibiting Cooperative Spin Transition, for 2D Molecular Memory Devices. *Laboratoire Chimie Organique* **1990**, 537-541.
- 16 Soyer, H.; Mingotaud, C.; Boillot, M.-L.; Delhaes, P. Spin Crossover of a Langmuir-Blodgett Film Based on an Amphiphilic Iron(II) Complex. *Langmuir* **1998**, *14*, 5890-5895.
- 17 Létard, J.-F.; Nguyen, O.; Soyer, H.; Mingotaud, C.; Delhaès, P.; Kahn, O. First Evidence of the LIESST Effect in a Langmuir-Blodgett Film. *Inorg. Chem.* **1999**, *38*, 3020-3021.
- 18 Cobo, S.; Molnár, G.; Real, J. A.; Bousseksou, A. Multilayer Sequential Assembly of Thin Films That Display Room-Temperature Spin Crossover with Hysteresis. *Angew. Chem., Int. Ed.* **2006**, *45*, 5786-5789.

- 19 Molnár, G.; Cobo, S.; Real, J. A.; Carcenac, F.; Daran, E.; Vieu, C.; Bousseksou, A. Combined Top-Down/Bottom-Up Approach for the Nanoscale Patterning of Spin-Crossover Coordination Polymers. *Adv. Mater.* **2007**, *19*, 2163-2167.
- 20 Agustí, G.; Cobo, S.; Gaspar, A. B.; Molnár, G.; Moussa, N. O.; Szilágyi, P. Á.; Pálfi, V.; Vieu, C.; Muñz, M. C.; Real, J. A.; Bousseksou, A. Thermal and Light-Induced Spin Crossover Phenomena in New 3D Hofmann-Like Microporous Metalorganic Frameworks Produced As Bulk Materials and Nanopatterned Thin Films. *Chem. Mater.* **2008**, *20*, 6721-6732.
- 21 Cavallini, M.; Bergenti, I.; Milita, S.; Ruani, G.; Salitros, I.; Qu, Z.-R.; Chandrasekar, R.; Ruben, M. Micro- and Nanopatterning of Spin-Transition Compounds into Logical Structures. *Angew. Chem., Int. Ed.* **2008**, *47*, 8596-8600.
- 22 Thibault, C.; Molnár, G.; Salmon, L.; Bousseksou, A.; Vieu, C. Soft Lithographic Patterning of Spin Crossover Nanoparticles. *Langmuir* **2010**, *26*, 1557-1560.
- 23 Rackwitz, S.; Faus, I.; Lägél, B.; Linden, J.; Marx, J.; Oesterschulze, E.; Schlage, K.; Willie, H.-C.; Wolff, S.; Wolny, J. A.; Schünemann, V. Installation of a Combined Raman and AFM Microscope as a Sample Environment for Nuclear Resonance Scattering at P01, PETRA III. *Hyperfine Interact.* **2014**, *226*, 667-671.
- 24 Naik, A. D.; Stappers, L.; Snauwaert, J.; Fransaeer, J.; Garcia, Y. A Biomembrane Stencil for Crystal Growth and Soft Lithography of a Thermochromic Molecular Sensor. *Small* **2010**, *6*, 2842-2846.
- 25 Bernien, M. X-ray Absorption Spectroscopy of Fe Complexes on Surfaces: Electronic Interactions and Tailoring of the Magnetic Coupling. Ph. D. Thesis, Freie Universität, Berlin, May 2009.
- 26 Shi, S.; Schmerber, G.; Arabski, J.; Beaufrand, J.-B.; Kim, D. J.; Boukari, S.; Bowen, M.; Kemp, N. T.; Viart, N.; Rogez, G.; Beaurepaire, E.; Aubriet, H.; Petersen, J.; Becker, C.; Ruch, D. Study of Molecular Spin-Crossover Complex Fe(phen)<sub>2</sub>(NCS)<sub>2</sub> Thin Films. *Appl. Phys. Lett.* **2009**, *95*, 043303.
- 27 Miyamachi, T.; Gruber, M.; Davesne, V.; Bowen, M.; Boukari, S.; Joly, L.; Scheurer, F.; Rogez, G.; Yamada, T. K.; Ohresser, P.; Beaurepaire, E.; Wulfhekel, W. Robust Spin Crossover and Memristance Across a Single Molecule. *Nat. Commun.* **2012**, *3*, 938.

- 28 Alam, M. S.; Stocker, M.; Gieb, K.; Müller, P.; Haryono, M.; Student, K.; Grohmann, A. Spin-State Patterns in Surface-Grafted Beads of Iron(II) Complexes. *Angew. Chem., Int. Ed.* **2010**, *49*, 1159-1163.
- 29 Bernien, M. Spin Crossover in a Vacuum-Deposited Submonolayer of a Molecular Iron(II) Complex. *J. Phys. Chem. Lett.* **2012**, *3*, 3431-3434.
- 30 Bousseksou, A.; Molnár, G.; Salmon L.; Nicolazzi, W. Molecular Spin Crossover Phenomenon: Recent Achievements and Prospects. *Chem. Soc. Rev.* **2011**, *40*, 3313-3335.
- 31 Cavallini, M. Status and Perspectives in Thin Films and Patterning of Spin Crossover Compounds. *Phys. Chem. Chem. Phys.* **2012**, *14*, 11855-11876.
- 32 Martinho, P. N.; Rajnak, C.; Ruben, M. Nanoparticles, Thin Films and Surface Patterns from Spin-Crossover Materials and Electrical Spin State Control. In *Spin-Crossover Materials: Properties and Applications*; Halcrow, M., Ed.; Wiley & Sons: West Sussex, U.K., 2013; Chapter 14, pp 375-404.
- 33 Larionova, J.; Salmon, L.; Guari, Y.; Tokarev, A.; Molvinger, K.; Molnár, G.; Bousseksou, A. Towards the Ultimate Size Limit of the Memory Effect in Spin-Crossover Solids. *Angew. Chem.* **2008**, *120*, 8360-8364.
- 34 Félix, G.; Nicolazzi, W.; Mikolasek, M.; Molnár, G.; Bousseksou, A. Non-Extensivity of Thermodynamics at the Nanoscale in Molecular Spin Crossover Materials: A Balance Between Surface and Volume. *Phys. Chem. Chem. Phys.* **2014**, *16*, 7358-7367.
- 35 Fong, H. H.; So, S. K. Hole Transporting Properties of Tris(8-hydroxyquinoline) Aluminum (Alq3). *J. Appl. Phys.* **2006**, *100*, 094502.
- 36 Aravena, D.; Ruiz, E. Coherent Transport through Spin-Crossover Single Molecules. *J. Am. Chem. Soc.* **2012**, *134*, 777-779.
- 37 Baadji, N.; Sanvito, S. Giant Resistance Across the Phase Transition in Spin-Crossover Molecules. *Phys. Rev. Lett.* **2012**, *108*, 217201.
- 38 Ruiz, E. Charge Transport Properties of Spin Crossover Systems. *Phys. Chem. Chem. Phys.* **2014**, *16*, 14-22.

- 39 Takahashi, K.; Cui, H.-B.; Okano, Y.; Kobayashi, H.; Einaga, Y.; Sato, O. Electrical Conductivity Modulation Coupled to a High-Spin—Low-Spin Conversion in the Molecular System  $[\text{Fe}^{\text{III}}(\text{qsal})_2][\text{Ni}(\text{dmit})_2]_3 \cdot \text{CH}_3\text{CN} \cdot \text{H}_2\text{O}$ . *Inorg. Chem.* **2006**, *45*, 5739-5741.
- 40 Djukic, B; Lemaire, M. T. Hybrid Spin-Crossover Conductor Exhibiting Unusual Variable-Temperature Electrical Conductivity. *Inorg. Chem.* **2009**, *48*, 10489–10491.
- 41 Matsuda, M.; Tajima, H. Thin Film of a Spin Crossover Complex  $[\text{Fe}(\text{dpp})_2](\text{BF}_4)_2$ . *Chem. Lett.* **2007**, *36*, 700-701.
- 42 Matsuda, M.; Isozaki, H.; Tajima, H. Electroluminescence Quenching by a Spin-Crossover Transition. *Chem. Lett.* **2008**, *37*, 374-375.
- 43 Rotaru, A.; Gural'skiy, I. A.; Molnár, G.; Salmon, L.; Demont, P.; Bousseksou, A. Spin State Dependence of Electrical Conductivity of Spin Crossover Materials. *Chem. Commun.* **2012**, *48*, 4163-4165.
- 44 Rotaru, A.; Dugay, J.; Tan, R. P.; Gural'skiy, I. A.; Salmon, L.; Demont, P.; Carrey, J.; Molnár, G.; Respaud, M.; Bousseksou, A. Nano-Electromanipulation of Spin Crossover Nanorods: Towards Switchable Nanoelectronic Devices. *Adv. Mater.* **2013**, *25*, 1745-1749.
- 45 Prins, F.; Monrabal-Capilla, M.; Osorio, E. A.; Coronado, E.; van der Zant, H. S. J. Room-Temperature Electrical Addressing of a Bistable Spin-Crossover Molecular System. *Adv. Mater.* **2011**, *23*, 1545-1549.
- 46 Etrillard, C.; Faramarzi, V.; Dayen, J.-F.; Létard, J.-F.; Doudin, B. Photoconduction in  $[\text{Fe}(\text{Htrz})_2(\text{trz})](\text{BF}_4) \cdot \text{H}_2\text{O}$  Nanocrystals. *Chem. Commun.* **2011**, *47*, 9663-9665.
- 47 Zhang, X.; Palamarciuc, T.; Rosa, P.; Létard, J.-F.; Doudin, B.; Zhang, Z.; Wang, J.; Dowben, P. A. Electronic Structure of a Spin Crossover Molecular Adsorbate. *J. Phys. Chem. C* **2012**, *116*, 23291-23296.
- 48 Ludwig, E.; Naggert, H.; Kalläne, M.; Rohlf, S.; Kröger, E.; Bannwarth, A.; Quer, A.; Rossnagel, K.; Kipp, L.; Tuczek, F. Iron(II) Spin-Crossover Complexes in Ultrathin Films: Electronic Structure and Spin-State Switching by Visible and Vacuum-UV Light. *Angew. Chem. Int. Ed.* **2014**, *53*, 3019-3023.
- 49 Gopakumar, T. G.; Matino, F.; Naggert, H.; Bannwarth, A.; Tuczek, F.; Berndt, R. Electron-Induced Spin Crossover of Single Molecules in a Bilayer on Gold. *Angew. Chem. Int. Ed.* **2012**, *51*, 6262-6266.

- 50 Pronschinske, A.; Chen, Y.; Lewis, G.; Shultz, D. A.; Calzolari, A.; Buongiorno-Nardelli, M.; Dougherty, D. B. Modification of Molecular Spin Crossover in Ultrathin Films. *Nano Lett.* **2013**, *13*, 1429-1434.
- 51 Pronschinske, A.; Bruce, R. C.; Lewis, G.; Chen, Y.; Calzolari, A.; Buongiorno-Nardelli, M.; Shultz, D. A.; You, W.; Dougherty, D. B. Iron(II) Spin Crossover Films on Au(111): Scanning Probe Microscopy and Photoelectron Spectroscopy. *Chem. Commun.* **2013**, *49*, 10446-10452.
- 52 Meded, V.; Bagrets, A.; Fink, K.; Chandrasekar, R.; Ruben, M.; Evers, F.; Bernand-Mantel, A.; Seldenthuis, J. S.; Beukman, A.; van der Zant, H. S. J. Electrical Control Over the Fe(II) Spin Crossover in a Single Molecule: Theory and Experiment. *Phys. Rev. B* **2011**, *83*, 245415.
- 53 Ellingsworth, E. C.; Turner, B.; Szulczewski, G. Thermal conversion of [Fe(phen)<sub>3</sub>](SCN)<sub>2</sub> thin films into the spin crossover complex Fe(phen)<sub>2</sub>(NCS)<sub>2</sub>. *RSC Adv.* **2013**, *3*, 3745.
- 54 Gao, G.; Xu, L.; Wang, W.; An, W.; Qiu, Y.; Wang, Z.; Wang, E. Electrochromic Multilayer Films of Tunable Color by Combination of Copper or Iron Complex and Monolacunary Dawson-Type Polyoxometalate. *J. Phys. Chem. B* **2005**, *109*, 8948-8953.
- 55 Day, P.; Sanders, N. The Spectra of Complexes of Conjugated Ligands. Part II. Charge-transfers in Substituted Phenanthroline Complexes: Intensities. *J. Chem. Soc. A* **1967**, 1536-1541.
- 56 Bergkamp, M. A.; Brunschwig, B. S.; Gütllich, P.; Netzel, T. L.; Sutin, N. Temperature Dependence on the Lifetimes of the Ligand-Field States of Tris(1,10-Phenanthroline)Iron(II). *Chem. Phys. Lett.* **1981**, *81*, 147-150.
- 57 Hoshina, G.; Ohba, S.; Tsuchiya, N.; Isobe, T.; Sennab, M. Tris(1,10-phenanthroline-*N,N'*)iron(II) dithiocyanate trihydrate. *Acta Cryst.* **2000**, *C56*, e191-e192.
- 58 Hauser, A. Light-Induced Spin Crossover and the High-Spin→Low-Spin Relaxation. *Top. Curr. Chem.* **2004**, *234*, 155-198.
- 59 Goodwin, H. A.; Sylva, R. N. The Magnetic Properties of Tris(2-methyl-1,10-phenanthroline)iron(II) ion. *Aust. J. Chem.* **1968**, *21*, 83-90.

- 60 Gallé, G.; Jonusauskas, G.; Tondusson, M.; Mauriac, C.; Letard, J. F.; Freysz, E. Transient Absorption Spectroscopy of the  $[\text{Fe}(\text{2 CH}_3\text{-phen})_3]^{2+}$  Complex: Study of the High Spin  $\leftrightarrow$  Low Spin Relaxation of an Isolated Iron(II) Complex. *Chem. Phys. Lett.* **2013**, 556, 82–88.
- 61 Sharma, G. D.; Sangodkar, S. G.; Gupta, S. K.; Roy, M. S. Charge Transport Mechanism and Photovoltaic Behaviour of Undoped and I<sub>2</sub> Doped tris(1,10-phenanthroline) iron (II) Complex (TPFe) Thin Film Devices. *J. Mater. Sci.: Mater. Electron.* **1998**, 9, 9-15.
- 62 Baker, W. A., Jr.; Bobonich, H. M. Magnetic Properties of Some High Spin Complexes of Iron(II). *Inorg. Chem.*, **1964**, 3, 1184-1188.
- 63 König, E. Some Aspects of the Chemistry of the Bis(2,2'-Dipyridyl) and Bis(1,10-Phenanthroline) Complexes of Iron(II). *Coord. Chem. Rev.* **1968**, 3, 471-495.
- 64 Baker, W. A., Jr.; Bobonich, H. M. Magnetic Studies of Mixed Ligand Complexes of Iron(II). *Inorg. Chem.*, **1963**, 2(5), 1071-1072.
- 65 Madeja, K.; König, E. Zur Frage der Bindungsverhältnisse in Komplexverbindungen des Eisen(II) Mit 1,10-Phenanthroline. *J. Inorg. Nucl. Chem.* **1963**, 25, 377-385.
- 66 Baker, W. A., Jr.; Long, G. J. Infrared Spectra of Some Magnetically Anomalous Iron(II) Complexes. *Chem. Commun.* **1965**, 426, 368-369.
- 67 König, E.; Madeja, K. Unusual Magnetic Behaviour of Some Iron(II)-Bis-(1,10-phenanthroline) Complexes. *Chem. Commun.* **1966**, 810, 61-62.
- 68 Dészi, I.; Molnár, B.; Tarnóczy, T.; Tompa, K. On the Magnetic Behaviour of iron(II)-bis-(1,10 phenanthroline)-thiocyanate Between -- 190° and 30°C. *J. Inorg. Nucl. Chem.* **1967**, 29, 2486-2490.
- 69 Collins, R. L.; Pettit, R. Mössbauer Studies of Iron Organometallic Complexes-III, Octahedral Complexes. *J. Inorg. Nucl. Chem.* **1966**, Vol. 28, 1001-1010.
- 70 König, E.; Madeja, K.  $^5\text{T}_2$ — $^1\text{A}_1$  Equilibria in Some Iron(II)-Bis(1,10-phenanthroline) Complexes. *Inorg. Chem.* **1967**, 6, 48-55.
- 71 Sorai, M.; Seki, S. Phonon Coupled Cooperative Low-Spin  $^1\text{A}_1 \rightleftharpoons$  High-Spin  $^5\text{T}_2$  Transition in  $[\text{Fe}(\text{phen})_2(\text{NCS})_2]$  and  $[\text{Fe}(\text{phen})_2(\text{NCSe})_2]$  Crystals. *J. Phys. Chem. Solids*, **1974**, 35, 555-570.

- 72 Bousseksou, A.; McGarvey, J. J.; Varret, F.; Real, J. A.; Tuchagues, J.-P.; Dennis, A. C.; Boillot, M. L. Raman Spectroscopy of the High- and Low-Spin States of the Spin Crossover Complex  $\text{Fe}(\text{phen})_2(\text{NCS})_2$  : an Initial Approach to Estimation of Vibrational Contributions to the Associated Entropy Change. *Chem. Phys. Lett.*, **2000**, *318*, 409-416.
- 73 Brehm, G.; Reiher, M.; Schneider, S. J. Estimation of the Vibrational Contribution to the Entropy Change Associated with the Low- to High-Spin Transition in  $\text{Fe}(\text{phen})_2(\text{NCS})_2$  Complexes: Results Obtained by IR and Raman Spectroscopy and DFT Calculations. *Phys. Chem. A*, **2002**, *106*, 12024-12034.
- 74 Gallois, B.; Real, J.-A.; Hauw, C.; Zarembowitch, J. Structural Changes Associated with the Spin Transition in  $\text{Fe}(\text{phen})_2(\text{NCS})_2$ : A Single-Crystal X-ray Investigation. *Inorg. Chem.* **1990**, *29*, 1152-1158.
- 75 MacLean, E. J.; McGrath, C. M.; O'Connor, C. J.; Sangregorio, C.; Seddon, J. M. W.; Sinn, E.; Sowrey, F. E.; Teat, S. J.; Terry, A. E.; Vaughan, G. B. M.; Young, N. A. Structural Study of the Thermal and Photochemical Spin States in the Spin Crossover Complex  $[\text{Fe}(\text{phen})_2(\text{NCSe})_2]$ . *Chem. Eur. J.* **2003**, *921*, 5314-5322.
- 76 Gruber, M.; Davesne, V.; Bowen, M.; Boukari, S.; Beaurepaire, E.; Wulfhekel, W.; Miyamachi, T. Spin State of Spin-Crossover Complexes: From Single Molecules to Ultrathin Films. *Phys. Rev. B* **2014**, *89*, 195415.
- 77 Chiş, V.; Droghetti, A.; Isai, R.; Morari, C.; Rungger, I.; Sanvito, S. DFT Structural Investigation on  $\text{Fe}(1,10\text{-phenanthroline})_2(\text{NCS})_2$  Spin Crossover Molecule. *AIP Conf. Proc.* **2013**, *1565*, 57-62.
- 78 Madeja, V. K.; Wilke, W.; Schmidt, S. Methoden zur Darstellung von Diacido-bis-1,10-phenanthrolin-Eisen(II) Komplexen. *Z. Anorg. Allg. Chem.* **1966**, *346*, 306-315.
- 79 Ganguli, P.; Gütllich, P.; Müller, E. W. Further Studies on the Spin Cross-over Phenomenon in Di-isothio-cyanatobis(1,10-phenanthroline)iron(II). *J. Chem. Soc., Dalton Trans.*, **1981**, 441-446.
- 80 Muller, E. W.; Spiering, H.; Gütllich, P. Spin Transition in  $[\text{Fe}(\text{phen})_2(\text{NCS})_2]$  and  $[\text{Fe}(\text{bipy})_2(\text{NCS})_2]$ . Hysteresis and Effect of Crystal Quality. *Chem. Phys. Lett.* **1982**, *93*, 567-571.

- 81 Akabori, K.; Matsuo, H.; Yamamoto, Y. Thermal Properties of Tris(1,10-Phenanthroline) Complexes of Iron(II) and Nickel(II) Salts. *J. Inorg. Nucl. Chem.*, **1973**, *35*, 2679-2690.
- 82 Schilt, A. A.; Fritsch, K. Some Transition Metal Thiocyanate 1,10-phenanthroline Mixed Ligand Complexes. *J. Inorg. Nucl. Chem.* **1966**, *28*, 2677-2683.
- 83 Driver, R.; Walker, W. R. Some Unusual Complexes of Iron with 1,10-Phenanthroline and 2,2'-Bipyridyl. *Aust. J. Chem.* **1967**, *20*, 1375-1383.
- 84 Cunningham, A. J.; Fergusson, J. E.; Powell, H. K. J.; Sinn E.; Wong, H. Magnetic Properties of Iron(II) Near the  $^5T_2 - ^1A_1$  Crossover. *J. Chem. Soc., Dalton Trans.*, **1972**, 2155-2160.
- 85 Teodorescu, M. The Structure of Dark-Red Compound  $[Fe(II)(phen)_2(NCS)_2] \cdot H_2O$ . *Revue Roumaine de Chimie* **1976**, *21(7)*, 1031-1036.
- 86 Böhmer, Von W.-H.; Madeja, K. Zur Infrarotspektroskopischen Charakterisierung von Eisen(II)-Komplexen mit einem Triplett-Grundzustand. *Z. Anorg. Allg. Chem.* **1982**, *486*, 153-164.
- 87 Savage, S.; Jia-Long, Z.; Maddock, A. G. The Red form of Bis(1,10-phenanthroline)dithiocyanatoiron(ii). *J. Chem. Soc. Dalton Trans.* **1985**, 991-996.
- 88 Lee, T. S.; Kolthoff, I. M.; Leussing, D. L. Reaction of Ferrous and Ferric Iron with 1,10-Phenanthroline. I. Dissociation Constants of Ferrous and Ferric Phenanthroline. *J. Am. Chem. Soc.* **1948**, *70*, 2348-2352.
- 89 Lei, L.; Jing, S.; Walton, R. I.; Xin, X.; O'Hare, D. Investigation of the Solid State Reaction of  $FeSO_4 \cdot 7H_2O$  with 1,10-Phenanthroline. *J. Chem. Soc., Dalton Trans.* **2002**, 3477-3481.
- 90 Ito, T.; Tanaka, N.; Hanazaki, I.; Nagakura, S. Electronic Structure of Tris(1,10-phenanthroline)iron(II) Complex. *Bull. Chem. Soc. Jpn.* **1969**, *42*, 702-709.
- 91 Saywell, L. G.; Cunningham, B. B. Determination of Iron: Colorimetric o-Phenanthroline Method. *Ind. Eng. Chem., Anal. Ed.* **1937**, *9*, 67-69.
- 92 Fortune, W. B.; Mellon, M. G. Determination of Iron with o-Phenanthroline: A Spectrophotometric Study. *Ind. Eng. Chem., Anal. Ed.* **1938**, *10*, 60-64.

- 93 Bandemer, S. L.; Schaible, P. J. Determination of Iron. A Study of the o-Phenanthroline Method. *Ind. Eng. Chem., Anal. Ed.* **1944**, *16*, 317-319.
- 94 Harvey, A. E., Jr.; Smart, J. A.; Amis, E. S. Simultaneous Spectrophotometric Determination of Iron(II) and Total Iron with 1,10-Phenanthroline. *Anal. Chem.* **1955**, *27*, 26-29.
- 95 Clark, R. J. H.; Turtle, P. C.; Strommen, D. P.; Streusand, B.; Kincaid, J.; Nakamoto, K. Resonance Raman Spectra and Excitation Profiles of Tris( $\alpha$ -diimine) Complexes of Iron(II). *Inorg. Chem.* **1977**, *16*, 84-89.
- 96 Bailey, R. A.; Kozak, S. L.; Michelsen, T. W.; Mills, W. N. Infrared Spectra of Complexes of the Thiocyanate and Related Ions. *Coord. Chem. Rev.* **1971**, *6*, 407-445.
- 97 Ganesan, K.; Ratke, L. Facile Preparation of Monolithic  $\kappa$ -Carrageenan Aerogels. *Soft Matter* **2014**, *10*, 3218-3224.
- 98 Sarkar, S.; Pande, S.; Jana, S.; Sinha, A. K.; Pradhan, M.; Basu, M.; Chowdhury, J.; Pal, T. Exploration of Electrostatic Field Force in Surface-Enhanced Raman Scattering: An Experimental Investigation Aided by Density Functional Calculations. *J. Phys. Chem. C* **2008**, *112*, 17862-17876.
- 99 McKenzie, E. D. The Steric Effect in Bis(2,2'-Bipyridyl) and Bis(1,10-Phenanthroline) Metal Compounds. *Coord. Chem. Rev.* **1971**, *6*, 187-216.
- 100 Inskeep, R. G. Infra-Red Spectra of Metal Complex Ions Below  $600\text{ cm}^{-1}$ —I. Spectra of the Tris Complexes 1, 10-Phenanthroline and 2,2'-Bipyridine with the Transition Metals Iron(II) through Zinc(II). *J. Inorg. Nucl. Chem.* **1962**, *24*, 763-776.
- 101 Schilt, A. A.; Taylor, R. C. Infra-red Spectra of 1:10-Phenanthroline Metal Complexes in the Rock Salt Region Below  $2000\text{ cm}^{-1}$ . *J. Inorg. Nucl. Chem.* **1959**, *9*, 211-221.
- 102 Andrade, G. F. S.; Temperini, M. L. A. 1,10-Phenanthroline Adsorption on Iron Electrode Monitored by Surface-Enhanced Raman Scattering (SERS). Comparison to SERS of Phen and Its Transition Metal Complex on Silver Electrode. *J. Phys. Chem. C* **2007**, *111*, 13821-13830.
- 103 Hutchinson, B.; Takemoto, J.; Nakamoto, K. Metal Isotope Effect on Metal-Ligand Vibrations. II. Tris Complexes of 2,2'-Bipyridine and 1,10-Phenanthroline. *J. Am. Chem. Soc.* **1970**, *92*, 3335-3339.

- 104 Hoefler, A. Vibrational Spectroscopy on Thermally and Optically Switchable Spin Crossover Compounds. Ph. D. Dissertation, Die Johannes Gutenberg-Universität, Mainz, Germany, 2000.
- 105 Burger, K.; Ebel, H.; Madeja, K. The Effect of Spin States of Iron(II) on the XPS of its Mixed Complexes. *J. Electron Spectrosc. Relat. Phenom.* **1982**, *28*, 115-121.
- 106 Lee, T. S.; Kolthoff, I. M.; Leussing, D. L. Reaction of Ferrous and Ferric Iron with 1,10-Phenanthroline. II. Kinetics of Formation and Dissociation of Ferrous Phenanthroline. *J. Am. Chem. Soc.* **1948**, *70*, 3596-3600.
- 107 Kolthoff, I. M.; Leussing, D. L.; Lee, T. S. Reaction of Ferrous and Ferric Iron with 1,10-Phenanthroline. III. The Ferrous Monophenanthroline Complex and the Colorimetric Determination of Phenanthroline. **1950**, *72*, 2173-2177.
- 108 Gasgnier, M.; Boillot, M. L.; Kaitasov, O. Electron Microscopy Studies between 80 and 480 K of a Spin Crossover Compound as [Fe(phen)<sub>2</sub>(NCS)<sub>2</sub>]. *J. Mater. Sci. Lett.* **2002**, *21*, 599-601.
- 109 Dockum, B. W.; Reiff, W. M. Thiocyanate-Bridged Transition-Metal Polymers. 1. Structure and Low-Temperature Magnetic Behavior of (Bipyridyl)iron(II) Thiocyanate: Fe(bpy)(NCS)<sub>2</sub>. *Inorg. Chem.* **1982**, *21*, 391-398.
- 110 Dockum, B. W.; Reiff, W. M. On the Existence of Tris 2,2'-biquinoline Complexes of First Transition Series Metal Ions in the Solid State. Spectra and Magnetic Characterization of [Fe(II)(2,2'-biquinoline)<sub>3</sub>](NCS)<sub>2</sub> and some Related Pseudo-tetrahedral Ferrous Compounds. *Inorg. Chim. Acta* **1986**, *120*, 61-76.
- 111 Lapidus, S. H.; Stephens, P. W.; Shurdha, E.; DaSilva, J. G.; Miller, J. S. Dimer Structure of 1,2-Bipyridyldichloroiron(II), [Fe<sup>II</sup>Cl<sub>2</sub>bipy]<sub>2</sub> and Chain Structure of 2,2'-Bipyridyldithiocyanatoiron(II), [Fe<sup>II</sup>(NCS)<sub>2</sub>bipy]<sub>n</sub>. The Use of Powder X-ray Diffraction Data to Determine the Structure of Werner Coordination Complexes. *Polyhedron* **2013**, *52*, 713-718.
- 112 Tuan, D. F.-T.; Reed, J. W.; Hoffman, R. Studies of the Linkage and Bonding of Triatomics in Transition Metal Complexes. Part 2. NCS<sup>-</sup> Complexes. *J. Mol. Struct.: THEOCHEM* **1991**, *232*, 111-121.

- 113 Tsuchiya, N.; Isobe, T.; Senna, M.; Yoshioka, N.; Inoue, H. Mechanochemical Effects on the Structures and Chemical States of  $[\text{Fe}(\text{Phen})_3](\text{NCS})_2 \cdot \text{H}_2\text{O}$ . *Solid State Commun.* **1996**, *99*, 525-529.
- 114 König, E.; Madeja, K. Infra-red Spectra at the  ${}^5\text{T}_2 - {}^1\text{A}_1$  Cross-over in Iron(II) Complexes. *Spectrochim. Acta* **1967**, *23A*, 45-54.
- 115 Duncan, J. F.; Mok, K. F. A Mössbauer Study of Iron(II)-1,10-Phenanthroline Complexes. *J. Chem. Soc. A* **1966**, 1494-1496.
- 116 Fisher, D. C.; Drickamer, H. G. Effect of Pressure on the Spin State of Iron in Ferrous Phenanthroline Compounds. *J. Chem. Phys.* **1971**, *54*, 4825-4837.
- 117 Herber, R.; Casson, L. M. Light-Induced Excited-Spin-State Trapping: Evidence from VTFTIR Measurements. *Inorg. Chem.* **1986**, *25*, 847-852.
- 118 Tsuchiya, N.; Tsukamoto, A.; Ohshita, T.; Isobe, T.; Senna, M.; Yoshioka, N.; Inoue, H. Anomalous Spin Crossover of Mechanically Strained Iron(II) Complexes with 1,10-Phenanthroline with Their Counterions,  $\text{NCS}^-$  and  $\text{PF}_6^-$ . *J. Solid State Chem.* **2000**, *153*, 82-91.
- 119 Bousseksou, A.; Molnár, G.; Demont, P.; Menegotto, J. Observation of a Thermal Hysteresis Loop in the Dielectric Constant of Spin Crossover Complexes: Towards Molecular Memory Devices. *J. Mater. Chem.* **2003**, *13*, 2069-2071.
- 120 Levchenko, G. G.; Bukin, G. V.; Gaspar, A. B.; Real, J. A. The Pressure-Induced Spin Transition in the  $\text{Fe}(\text{phen})_2(\text{NCS})_2$  Model Compound. *Russ. J. Phys. Chem. A* **2009**, *83*, 951-954.
- 121 Matienzo, L. J.; Yin, L. I.; Grim, S. O.; Swartz, W. E., Jr. X-ray Photoelectron Spectroscopy of Nickel Compounds. *Inorg. Chem.* **1973**, *12*, 2762-2769.
- 122 Johansson, L. Y.; Larsson, R.; Blomquist, J.; Cederström, C.; Grapenieser, S.; Helgeson, U.; Moberg, L. C.; Sundbom, M. X-ray Photoelectron and Mössbauer Spectroscopy on a Variety of Iron Compounds. *Chem. Phys. Lett.* **1974**, *24*, 508-513.
- 123 Norbury, A. H.; Thompson, M.; Songstad, J. X-ray Photoelectron Spectroscopy of the Cyanate, Thiocyanate, Selenocyanate and Tellurocyanate Ions. *Inorg. Nucl. Chem. Lett.* **1973**, *9*, 347-350.

- 124 Haddad, M. S.; Federer, W. D.; Lynch, M. W.; Hendrickson, D. N. Spin-Crossover Ferric Complexes: Unusual Effects of Grinding and Doping Solids. *Inorg. Chem.* **1981**, *20*, 131-139.
- 125 Coronado, E.; Galán-Mascarós, J. R.; Monrabal-Capilla, M.; García-Martínez, J.; Pardo-Ibáñez, P. Bistable Spin-Crossover Nanoparticles Showing Magnetic Thermal Hysteresis Near Room Temperature. *Adv. Mater.* **2007**, *19*, 1359-1361.
- 126 Tissot, A.; Bardeau, J.-F.; Rivière, E.; Brisset, F.; Boillot, M.-L. Thermo- and Photoswitchable Spin-Crossover Nanoparticles of an Iron(II) Complex Trapped in Transparent Silica Thin Films. *Dalton Trans.* **2010**, *39*, 7806-7812.
- 127 Chakraborty, P.; Boillet, M.-L.; Tissot, A.; Hauser, A. Photoinduced Relaxation Dynamics in Iron(II) Spin-Crossover Nanoparticles: The Significance of Crystallinity. *Angew. Chem. Int. Ed.* **2013**, *52*, 1-5.
- 128 Sinitskiy, A. V.; Tchougréeff, A. L.; Dronskowski, R. Phenomenological Model of Spin Crossover in Molecular Crystals as Derived from Atom-Atom Potentials. *Phys. Chem. Chem. Phys.* **2011**, *13*, 13238-13246.
- 129 Casey, A. T.; Isaac, F. Comment on the Anomalous Paramagnetism of  $[\text{Fe}(\text{NCS})_2\text{phen}_2]$ . *Aust. J. Chem.* **1967**, *20*, 2765-2766.
- 130 Ozarowski, A.; McGarvey, B. R.; Sarkar, A. B.; Drake, J. E. EPR Study of Manganese(II) in Two Crystalline Forms of  $\text{Fe}(\text{C}_6\text{H}_8\text{N}_2\text{S}_2)_2(\text{NCS})_2$  and the High-Spin—Low-Spin Transition that Occurs in Only One Form. X-ray Structure Determination of Both Forms. *Inorg. Chem.* **1988**, *27*, 628-635.
- 131 Vasudevan, S.; Vasan, H. N.; Rao, C. N. R. PES Study of Spin-State Transitions in  $d^6$  Transition Metal Complexes and Oxides. *Chem. Phys. Lett.* **1979**, *65*, 444-451.
- 132 Burger, K.; Furlani, C.; Mattogno, G. J. XPS Structural Characterization of Spin State Crossover in  $\text{Fe}^{\text{II}}(\text{NCS})_2(o\text{-phen})_2$ . *Electron. Spectrosc. Relat. Phenom.*, **1980**, *21*, 249-256.
- 133 Chiechi, R. C.; Weiss, E. A.; Dickey, M. D.; Whitesides, G. M. Eutectic Gallium-Indium (EGaIn): A Moldable Liquid Metal for Electrical Characterization of Self-Assembled Monolayers. *Angew. Chem. Int. Ed.* **2008**, *47*, 142-144.
- 134 Haicka, H.; Cahen, D. Making Contact: Connecting Molecules Electrically to the Macroscopic World. *Prog. Surf. Sci.* **2008**, *83*, 217-261.

- 135 Eastment, R. M.; Mee, C. H. B. Work Function Measurements on (100), (110) and (111) Surfaces of Aluminum. *J. Phys. F.: Metal Phys.* **1973**, *3*, 1738-1745.
- 136 Stöbel, M.; Staudigel, J.; Steuber, F.; Blässing, J.; Simmerer, J.; Winnacker, A. Space-Charge-Limited Electron Currents in 8-Hydroxyquinoline Aluminum. *Appl. Phys. Lett.* **2000**, *76*, 115-117.
- 137 Uddin, A.; Lee, C. B.; Hu, X.; Wong, T. K. S. Interface Injection-Limited Carrier-Transport Properties of Alq<sub>3</sub>. *Appl. Phys. A* **2004**, *78*, 401-405.
- 138 Mott, N. F.; Gurney, R. W. *Electronic Processes in Ionic Crystals*. Clarendon Press: Oxford, 1940.
- 139 Kumar, A.; Srivastava, R.; Tyagi, P.; Mehta, D. S.; Kamalasanan, M. N. Effect of Doping of 8-Hydroxyquinolinatolithium on Electron Transport in Tris(8-Hydroxyquinolinato)Aluminum. *J. Appl. Phys.* **2011**, *109*, 114511.
- 140 Monzon, L. M. A.; Burke, F.; Coey, J. M. D. Optical, Magnetic, Electrochemical, and Electrical Properties of 8-Hydroxyquinoline-Based Complexes with Al<sup>3+</sup>, Cr<sup>3+</sup>, Mn<sup>2+</sup>, Co<sup>2+</sup>, Ni<sup>2+</sup>, Cu<sup>2+</sup>, and Zn<sup>2+</sup>. *J. Phys. Chem. C* **2011**, *115*, 9182-9192.
- 141 Blakesley, J. C.; Castro, F. A.; Kylberg, W.; Dibb, G. F. A.; Arantes, C.; Valaski, R.; Cremona, M.; Kim, J. S.; Kim, J.-S. Towards Reliable Charge-Mobility Benchmark Measurements for Organic Semiconductors. *Org. Electron.* **2014**, *15*, 1263-1272.
- 142 Krause, S.; Casu, M. B.; Schöll, A.; Umbach, E. Determination of Transport Levels of Organic Semiconductors by UPS and IPS. *New J. Phys.* **2008**, *10*, 085001.
- 143 Barth, S.; Müller, P.; Riel, H.; Seidler, P. F.; Rieß, W.; Vestweber, H.; Bässler, H. Electron Mobility in Tris(8-Hydroxy-quinoline)Aluminum Thin Films Determined via Transient Electroluminescence from Single- and Multilayer Organic Light-Emitting Diodes. *J. Appl. Phys.* **2001**, *89*, 3711-3719.
- 144 Brütting, W.; Berleb, S.; Mückl, A. G. Device Physics of Organic Light-Emitting Diodes Based on Molecular Materials. *Org. Electron.* **2001**, *2*, 1-36.
- 145 Wang, Z.; Lou, Y.; Naka, S.; Okada, H. Bias and Temperature Dependent Charge Transport in Solution-Processed Small Molecular Mixed Single Layer Organic Light Emitting Devices. *Appl. Phys. Lett.* **2011**, *98*, 063302.

- 146 Ishihara, S.; Hase, H.; Okachi, T.; Naito, H. Demonstration of Determination of Electron and Hole Drift-Mobilities in Organic Thin Films by Means of Impedance Spectroscopy Measurements. *Thin Solid Films* **2013**, *554*, 213-217.
- 147 Steil, S.; Großmann, N.; Laux, M.; Ruffing, A.; Steil, D.; Wiesenmayer, M.; Mathias, S.; Monti, O. L. A.; Cinchetti, M.; Aeschlimann, M. Spin-Dependent Trapping of Electrons at Spinterfaces. *Nat. Phys.* **2013**, *9*, 242-247.
- 148 Lampert, M. A. Simplified Theory of Space-Charge-Limited Currents in an Insulator with Traps. *Phys. Rev.* **1956**, *103*, 1648-1656.
- 149 Karl, N. Charge Carrier Transport in Organic Semiconductors. *Synth. Met.* **2003**, *133-134*, 649-657.
- 150 Coropceanu, V.; Cornil, J.; da Silva Filho, D. A.; Olivier, Y.; Sibley, R.; Brédas, J.-L. Charge Transport in Organic Semiconductors. *Chem. Rev.* **2007**, *107*, 926-952.
- 151 Boukheddaden, K.; Bailly-Reyre, A. Towards the Elastic Properties of 3D Spin-Crossover Thin Films: Evidence of Buckling Effects. *EPL* **2013**, *103*, 26005.
- 152 Matsuzawa, S.; Tazoe, K.; Nojiri, H.; Iijima, F.; Oshio, H. Correlation among Charge, Dielectric, and Magnetic Properties in Electron-Transfer-Type Spin-Crossover Systems. *Chem. Lett.* **2014**, *43*, 1173-1175.